HIGH PERFORMANCE HgCdTe PHOTODETECTOR DESINGS

VIA DARK CURRENT SUPPRESSION

A THESIS SUBMITTED TO
THE GRADUATE SCHOOL OF NATURAL AND APPLIED SCIENCES
OF
THE MIDDLE EAST TECHNICAL UNIVERSITY

BY

YİĞİT ÖZER

IN PARTIAL FULFILLMENT OF THE REQUIREMENTS
FOR
THE DEGREE OFMASTER OF SCIENCE
IN
ELECTRICAL AND ELECTRONICS ENGINEERING

JULY 2018

Approval of the thesis:

HIGH PERFORMANCE HgCdTe PHOTODETECTOR DESINGS
VIA DARK CURRENT SUPPRESSION

submitted by **YİĞİT ÖZER** in partial fulfillment of the requirements for the degree of **Master of Science in Electrical and Electronics Engineering Department, Middle East Technical University** by,

Prof. Dr. Halil Kalıpçılar
Director, Graduate School of **Natural and Applied Sciences** _____

Prof. Dr. Tolga Çiloğlu
Head of Department, **Electrical and Electronics Engineering** _____

Asst. Dr. Serdar Kocaman
Supervisor, **Electrical and Electronics Engineering Dept., METU** _____

Examining Committee Members:

Prof. Dr. Cengiz Beşikçi
Electrical and Electronics Engineering Dept., METU _____

Asst. Dr. Serdar Kocaman
Electrical and Electronics Engineering Dept., METU _____

Assoc. Prof. Dr. Barış Bayram
Electrical and Electronics Engineering Dept., METU _____

Prof. Dr. Gönül Turhan Sayan
Electrical and Electronics Engineering Dept., METU _____

Assoc. Prof. Dr. Tuğba Selcen Navruz
Electrical and Electronics Engineering Dept., Gazi University _____

Date: 04.07.2018

I hereby declare that all information in this document has been obtained and presented in accordance with academic rules and ethical conduct. I also declare that, as required by these rules and conduct, I have fully cited and referenced all material and results that are not original to this work.

Name, Last Name: Yiğit Özer

Signature :

ABSTRACT

HIGH PERFORMANCE HgCdTe PHOTODETECTOR DESINGS VIA DARK CURRENT SUPPRESSION

Özer, Yiğit
M.S., Department of Electrical and Electronics Engineering
Supervisor : Asst. Prof. Dr. Serdar Kocaman

July 2018, 114 pages

This thesis work covers the numerical analysis and design of infrared photon detectors with a focus of HgCdTe based devices. An in-house numerical tool is utilized for the design and characterization process, where the Poisson, current and continuity equations are solved numerically with the high precision in electrical and optical properties. A high operating temperature alternative substrate mid-wave HgCdTe detector is designed benefiting from the generation-recombination dark current suppression. The advancement in the operating temperature is nearly 40 K (from ~85 K to ~125 K) for the designed device structure, which leads to diffusion limited dark current even for a very low carrier lifetimes (τ_{SRH} = 200 ns). The performance enhancement is achieved by the utilization of high Cd composition material at the depletion region targeting lower SRH recombination rates. The sensitivity of the designed structure to the fabrication errors is analyzed in terms of doping, composition and layer thickness. Moreover, a design methodology is introduced so that the inserted wide bandgap layer does not create valence band discontinuity that might lead to a noticeable decrease in quantum efficiency. In addition, a similar method is applied to SWIR window and performance of HgCdTe SWIR detectors has been shown to increase as well. The designed SWIR detector reached state-of-art sensors in terms of dark current density while benefiting from the reduced cost of alternative substrate

detectors. With this enhancement, the designed HgCdTe sensors are capable of sensing based on solely nightglow radiation.

Keywords: dark current suppression, alternative substrate, HgCdTe, nightglow detection, high operation temperature.

ÖZ

KARANLIK AKIM BASIRMA İLE YÜKSEK PERFORMANSLI HgCdTe FOTODEDEKTÖR DİZAYNLARI

Özer, Yiğit
Yüksek Lisans, Elektrik Elektronik Mühendisliği Bölümü
Tez Yöneticisi : Dr. Öğr. Üyesi Serdar Kocaman

Temmuz 2018, 114 sayfa

Bu tez çalışması HgCdTe bazlı cihazlar için kızılötesi dedektör tasarımı ve numerik analizini kapsamaktadır. Dizayn ve karakterizasyon aşamaları için, kurum içi geliştirilen numerik araç kullanılmış ve bu araç Poission, akım ve devamlılık denklemlerini çözerken, optik ve elektriksel değerlerin yüksek kesinlik ile hesaplanmasında kullanılmıştır.

Oluşma-rekombinasyon karanlık akım bastırma yönteminden faydalanılarak, yüksek çalışma sıcaklıklı alternatif taban orta dalgaboyu HgCdTe kızılötesi dedektör dizayn edildi. Çalışma sıcaklığında ulaşılan artış ortaya konulan cihaz için yaklaşık 40 K (~85 K den ~125 K e) olup, çok küçük taşıyıcı ömrüne (τ_{SRH} = 200 ns) rağmen difüzyon limitli performansa ulaşıldı. Performans artışı düşük rekombinasyon oranı hedeflenerek, yayılım bölgesine yüksek Cd kompozisyonlu malzeme uygulanması ile sağlanmıştır. Önerilen cihaz yapısının fabrikasyon hatalarına olan hassasiyeti katkılama, kompozisyon ve katman kalınlığına göre analiz edilmiştir. Dahası, eklenilen geniş bantgenişlikli katmanın, düşük kuantum verimliliğe yol açabilecek valans band devamsızlığı oluşturmaması amacıyla bir dizayn yöntemi tanıtılmıştır.

Ek olarak, benzer bir metodoloji SWIR penceresinde uygulandı ve aynı şekilde SWIR dedektörlerin de performansının iyileştirildiği gözlendi. Ortaya konulan SWIR dedektörler, alternatif taban HgCdTe dedektörlerin sunduğu düşük maliyetten yararlanırken aynı zamanda karanlık akım yoğunluğu anlamında günümüzün en gelişmiş sensörlerinin seviyesine ulaşmıştır. Bu gelişme ile beraber, dizayn edilen SWIR sensörler tek başına gece parıltısı ışımasından yararlanarak görüntüleme yapma kapasitesindedir.

Anahtar Kelimeler: karanlık akım bastırma, alternatif taban, HgCdTe, gece parıltısı ışıması, yüksek çalışma sıcaklığı

To my family

ACKNOWLEDGMENTS

First, I would like to express my sincere thanks to my advisor Asst. Prof. Dr. Serdar Kocaman for his enlightening guidance and unflagging support. It would not be possible to overcome difficulties and to achieve my goals without his supervision.

I would like to thank Prof. Dr. Cengiz Beşikçi for the opportunity to work in a well-equipped facility as well as his enlightening discussions and technical comments.

I would like to thank Prof. Dr. Gönül Turhan Sayan, Assoc. Prof. Dr. Barış Bayram and Assoc. Prof. Dr. Tuğba Selcen Navruz for being on my thesis committee.

I want to give my special thanks to Mr. Eray Yurtseven and Mr. Kaan Sel for sharing their clean room experience and valuable suggestions with me as well as their friendship.

I would like to thank Mr. Can Livanelioğlu for his effort and contribution to this thesis.

I would like to thank Mr. Göktuğ Cihan Özmen, Mr. Alperen Gövdeli, Mr. Utku Karaca, Mr. Anıl Aslan, Mr. Muratcan Sarıhan, Mr. Ekin Kızılkan and Mr. Mertcan Erdil for their technical comments as well as their friendship.

During the procession of this study, the author acknowledges the financial support of TUBITAK BIDEB 2210-A 2017-1 Scholarship.

Last but the best, I want to express my sincere appreciation to my family for their endless support.

TABLE OF CONTENTS

LIST OF FIGURES

FIGURES

LIST OF TABLES

TABLES

CHAPTER 1

INTRODUCTION

Infrared detection technology is a leading research topic for both academia and industry over 100 years for its contribution to human life with a wide range of applications. Together with the foundation of invisible rays in the spectrum of light, major technologies have been developed such us spectroscopy, night vision, thermal and hyperspectral imaging.

In 1950s, infrared detectors were designed to be single dimension arrays (first generation) with mechanical scanner [1]. After the development of CMOS readout integrated circuits (ROICs), second-generation focal plane arrays (FPAs) are presented with crucial enhancements over the scanning detectors. For instance, design and fabrication of megapixel detector arrays are accomplished together with smaller size, improved response time, lower power consumption and frequency noise level. Recently, a major part of the research laboratories focusses on third-generation detectors [2], which aim to introduce new capabilities such as dual-color detection, high frame rates, high thermal resolution and large number of pixels.

In order to enhance and diversify the capabilities of infrared technology, research institutions study many different semiconductor materials such as HgCdTe, InGaAs, Ge, InSb as well as QWIPs (AlGaInAs/InP, InGaAs/InAlAs & InGaAs/InP etc.) and superlattice detector systems (GaAs/AlAs & GaAs/$Al_xGa_{1-x}As$) [3-18]. All of these materials have unique characteristics in terms of electrical and optical properties. In this thesis, an in-house numerical tool is developed in order to investigate electrical and optical properties of HgCdTe infrared detectors. Moreover, a dark current suppression method is utilized for alternative substrate short-wave and mid-wave infrared sensing applications.

This chapter introduces fundamentals of electromagnetic light spectrum, infrared sensor types and figures of merit.

The second chapter summarizes the current HgCdTe technology including special layer structures, advantages and recent challenges of this material technology.

The third chapter details the utilization of in-house numerical tool for HgCdTe detectors. In this chapter, the material properties, normalization, discretization models and mathematical solution methods are represented.

The following chapter presents the design of the mid-wave infrared detector for alternative substrates with design approach, valence band reduction technique, sensitivity and performance analysis.

The chapter five introduces novel SWIR detector designs for lattice mismatched InGaAs and alternative substrate HgCdTe in order to sense nightglow radiation.

Finally, in the last chapter, the conclusion of the study and the future work is presented.

1.1.Infrared Imaging Basics

1.1.1. Electromagnetic Radiation

Interaction of light and matter generates physical processes - absorption, transmission and reflection- that determine the characteristics of optical systems [18]. Absorbance (α), reflectance (ρ) and transmittance (T) are the coefficients describing the optical properties of the object and they are described in Kirchhoff Law of Thermal radiation [19] as follows,

$$\rho + \alpha + T = 1 \tag{1.1}$$

Moreover, Kirchhoff Law also describes emittance (ε) as equal to the absorbance which means that good absorbers are also good emitters. An ideal absorber object is defined as a blackbody, which perfectly absorbs incoming light and re-emits ($\alpha = \varepsilon = 1$). Starting from early 1800s, astronomer William Herschel, Balfour Stewart and Gustav Kirchhoff contributed the thermal radiation phenomena revealing that

temperature of an object has a direct influence on emission and absorption processes. A Nobel Prize winner German scientist Max Planck finalized the theory and proposed the formula known as Planck's Law [20]. This physical law states that the emission spectrum of an object having a temperature above absolute zero (0 K) should be determined by,

$$M_\lambda(\lambda,T) = \frac{2\pi hc^2}{\lambda^5(e^{\frac{hc}{\lambda kT}}-1)} \frac{W}{cm^2.\mu m} \tag{1.2}$$

where M_λ is spectral exitance, λ is a wavelength of emittance, h is Planck's constant and c is the speed of light.

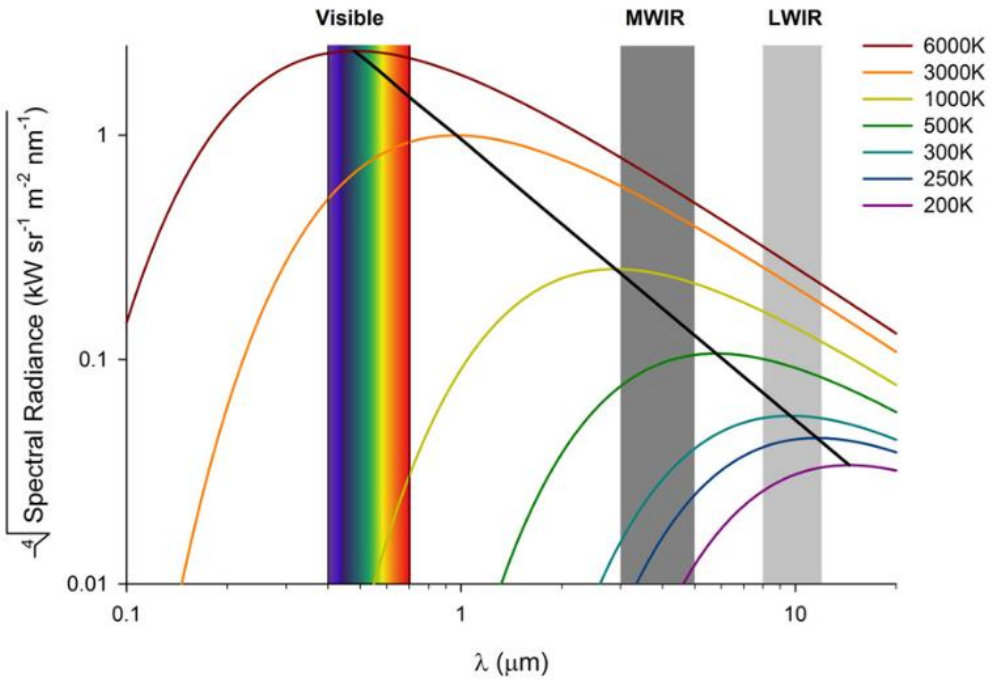

Figure 1.1: Spectral Radiance for various objects at different temperatures [21].

The integral of the spectral exitance for wavelengths from zero to infinity provides the total amount of energy emitted from the target with corresponding temperature. This phenomena is also known as the Stefan-Boltzmann Law [22] and it is given by,

$$M(T) = \int_0^\infty M_\lambda(\lambda,T)d\lambda = \sigma T^4 \frac{W}{cm^2} \tag{1.3}$$

where σ is the Stefan-Boltzmann Constant ($\sigma = 5.67032 \times 10^{-12} W/cm^2K^4$). It is obvious that the emitted energy from an object is determined by the fourth power of the temperature. Another point is that the wavelength where the maximum emission

occurs is a function of temperature and this phenomena is introduced as Wien Displacement Law [23]. Derivative of the spectral exitance with respect to the wavelength point is zero for this wavelength and it is equal to,

$$\lambda_{max} = \frac{2898\ \mu mK}{T(K)} \tag{1.4}$$

Furthermore, emissivity is an important parameter determining the total energy emission ratio between the actual material and blackbody. It is, in general, wavelength dependent parameter. However, in literature, emissivity of a material is specified as follows,

$$\varepsilon = \frac{\int_0^\infty \varepsilon(\lambda) M_\lambda(\lambda,T) d\lambda}{\int_0^\infty M_\lambda(\lambda,T) d\lambda} = \frac{\int_0^\infty \varepsilon(\lambda) M_\lambda(\lambda,T) d\lambda}{\sigma T^4} \tag{1.5}$$

The emissivity of a human body is ~0.98, which is approximated as a blackbody in this thesis.

1.1.2. Atmospheric Transmission

The electromagnetic radiation attenuates due to two different physical process. Firstly, gas molecules in the atmosphere absorb a portion of light and cause low transmission rate at specific wavelengths. Each type of atmospheric elements corresponds to an absorption in different wavelength due to diversified resonant frequencies of the inner bonds. Water vapor (H_2O) and the carbon dioxide (CO_2) are two of the most dominant mechanisms of atmospheric absorption.

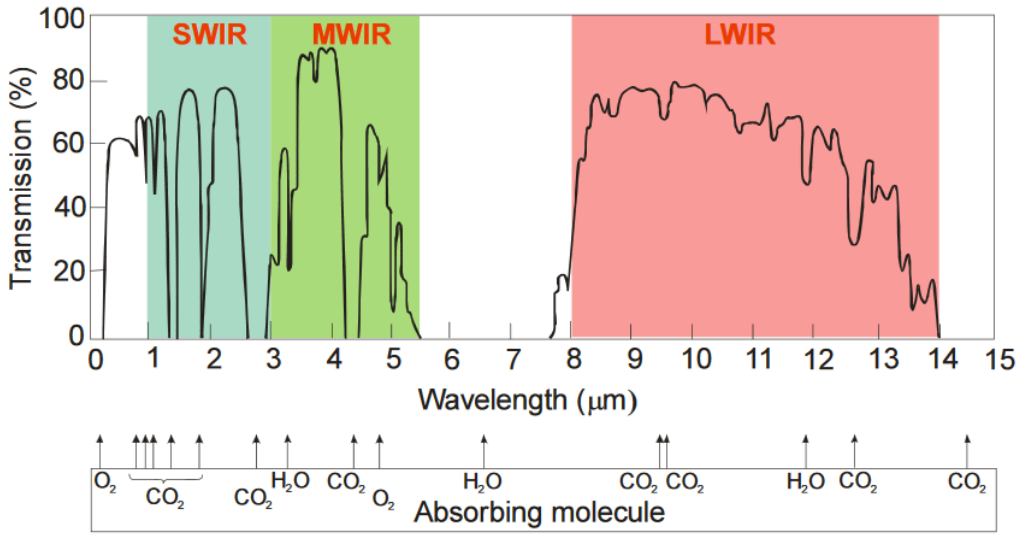

Figure 1.2: Measured atmospheric transmission at sea level. Blue, green and red regions illustrates SWIR, MWIR and LWIR windows respectively. The inset at the bottom represents the absorption wavelengths for corresponding molecules [24].

As seen in the **Figure 1.2**, atmospheric transmission is nearly zero in certain regions. Therefore, wavelengths of detection is divided into windows from visible wavelengths (700 nm) to far infrared region (~100 μm). The commonly accepted infrared regions are summarized below.

- Near infrared region (NIR): 0.7 μm – 1.4 μm
- Short wavelength infrared region (SWIR): 1.4 μm – 1.7 μm
- Mid-wavelength infrared region (MWIR): 3 μm – 5 μm
- Long wavelength infrared region (LWIR): 8 μm – 12 μm
- Very long wavelength infrared region (VLWIR): 12 μm – 20 μm
- Far infrared region (FIR): 20 μm – 1000 μm

One valuable application of the infrared detection is thermal imaging. Capturing the infrared radiation emitted by the objects above absolute zero temperature and identification of the targets in absolute dark environments are among crucial capabilities for the defense industry. The radiation emitted from a near room temperature object or a human is significant above ~4 μm wavelength, which enables thermal detection in MWIR and LWIR bands. However, this radiation is insufficiently low in SWIR band and the sun is the major natural source of radiation in this band. Therefore, usually, reflected sunlight from an object is aimed to be detected in SWIR

band. The characteristics of a SWIR image is similar to the visible imaging but it provides several advantages over conventional cameras. Capability to seeing through fog and haze, longer visibility distance and material identification are some of the useful applications in SWIR band.

Scattering is an atmospheric event, which causes the attenuation in electromagnetic radiation. The interaction of incident light and a particle in atmosphere initiates scattering. For this process, the size of the particle determines the scattering type and hence the behavior of the attenuation. The particles having a larger size than the wavelength of light are subject to Mie Scattering [25]. Rain and fog are examples of this type of atmospheric event. Another type of scattering is Rayleigh scattering [26] and it is effective when the particle in the atmosphere has a comparable size with the wavelength of incident light. Typically, it has wavelength dependent characteristics in which the short wavelength light scatters more than the other wavelengths of light. This physical phenomenon constitutes the color of sky during the mid-day and sunset conditions.

The transmission of radiation can be calculated as seen in Equation 1.6.

$$T = e^{-(K_a+\gamma)x} \tag{1.6}$$

T is transmission, K_a is absorption coefficient, γ is scattering coefficient and x represents the distance between light source and observer. The absorption coefficient strongly depends on the wavelength of light. Moreover, scattering coefficient can be expressed as,

$$\gamma = n\pi r^2 K_0 \tag{1.7}$$

n corresponds to number of particles in a cm^3 volume, r represents the radius of the particle and K_0 corresponds to intrinsic scattering coefficient, which determines the scattering ratio depending on the particle radius and wavelength. This constant can be estimated by using **Figure 1.3**.

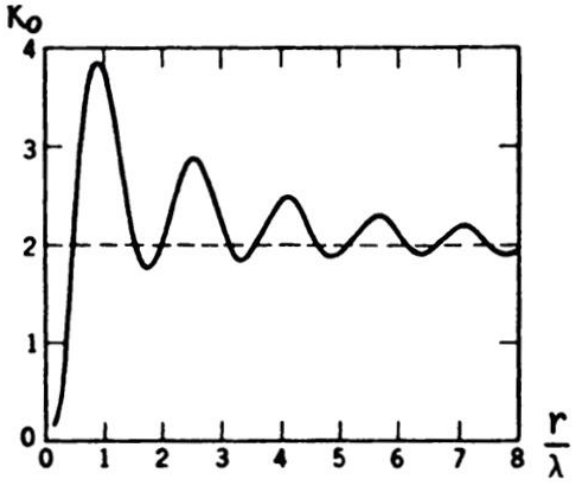

Figure 1.3: K_0 values are illustrated with respect to the ratio of radius of particle to the wavelength of incoming light [27].

As the value of x axis gets larger in **Figure 1.3**, Mia scattering dominates the Rayleigh scattering and K_0 approaches a certain value with insignificant oscillation. However, lower r/λ values (0 - 3) are subject to a significant change in the scattering and represent strongly wavelength dependent characteristics.

1.2. Infrared Detector Types

The infrared detectors can be classified into two categories as thermal and photon detectors. Each detector type benefits from different physical mechanisms and hence, they have different applications.

1.2.1. Thermoelectric Detectors

Firstly, thermal detectors aim to sense the resistivity, conductivity or permittivity change of the material. The temperature of the detector increases when the incoming light is absorbed by the material. This temperature increment influences the electrical properties of the material and changes the output signal. Thermopiles, pyroelectric detectors and micro bolometers are examples of the thermal detectors.

Thermopiles consist of two conductive arms, which are physically connected in one side and open in the other side. The voltage difference is measured from the open

arms. In case of the illumination, the resistivity changes in the exited arm and affects the measured voltage.

Pyroelectric detectors based on materials such as DLaTGS, $LiTaO_3$, and PZT. These semiconductors are pyroelectric materials, which produce charge in the surface depending on their temperature. The temperature fluctuation is usually triggered by optical illumination in order to build a photodetector.

Another thermoelectric detector is microbolometers. Similar to the other thermoelectric detectors, the resistivity of corresponding region changes under illumination. Microbolometers senses this local change and CMOS circuitry reads the data. Thermal isolation for each pixel is essential for this technology so that the response time of the detector can be increased. For this purpose, the light sensitive region is usually suspended and its connection to the substrate is minimized.

1.2.2. Photon Detectors

These detectors based on the creation of electron-hole pairs generated by the incident photons. A photon having an energy, which greater than the bandgap of the semiconductor, initiates the generation of charge carriers. When we measure the current value, it provides information about the intensity of incoming light. This procedure is wavelength sensitive. Therefore, photon detectors should be designed for the desired operation wavelength. Since the operation between electrons and photons is very fast compared to thermal response time of thermoelectric detectors, they are usually utilized for high-speed applications.

Photon detectors can be classified in two categories, which are photoconductive and photovoltaic detectors. The schematic for photoconductive devices is given in **Figure 1.4**.

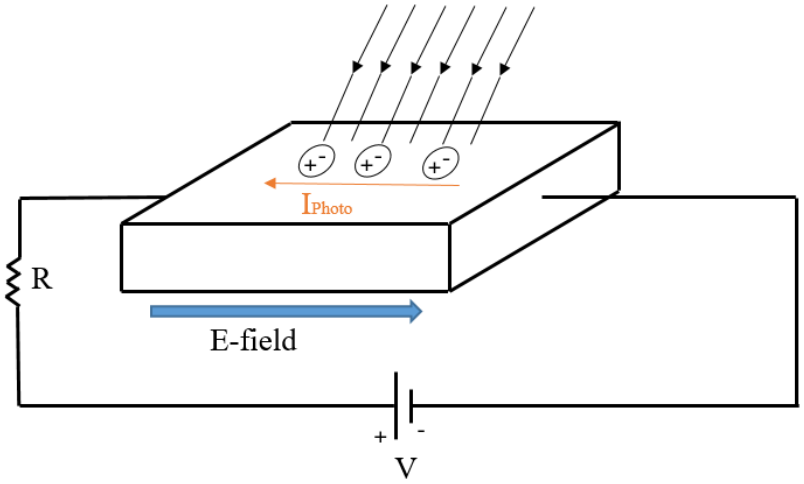

Figure 1.4: The photoconductive detector illustration under illumination.

This topology requires electric field, which is created by the external voltage source in order to collect charged carriers. In the effect of electric field, electrons and holes moves towards opposite directions and reach electrical contacts. The efficiency of this process increases with higher bias voltage but it is not desired due to the elevated power dissipation.

On the other hand, the photovoltaic devices benefit from the internal electric field for the efficient collection of photo-generated carriers, even though the generation of EHPs is similar to the photoconductive case. The properties of this electric field can be adjusted by donor and acceptor doping profiles. The excitation of the carriers with incoming light produces a current value namely photo current, which can be considered as signal level. Moreover, without any light source, there is still an existing current, which is generated by the thermal generation and recombination mechanisms. This current is called dark current and in most cases, it determines the operation conditions (temperature, bias etc.) of the device.

1.3. Electrical Properties of Photovoltaic Detectors

1.3.1. Dark Current

In a photovoltaic device, the current characteristics depend on many parameters such as doping profiles, material type, device length and defects. The dark current level has critical importance for the determination of operating temperature and bias voltage

and it is governed by various mechanisms. Diffusion current is the most fundamental dark current component for infrared detectors and an ideal detector should have only diffusion current as a dark current component. For a long diode, the dark current level can be evaluated as [28],

$$I_{dark} = qA\left(\frac{L_p}{\tau_p}p_n + \frac{L_n}{\tau_n}n_p\right)\left(e^{\frac{qV}{kT}} - 1\right) \tag{1.8}$$

where q is the unit charge, A is device area, L_p and L_n are diffusion lengths, p_n and n_p are electron and hole densities which are given by,

$$p_n = \frac{n_i^2}{N_D} \tag{1.9}$$

$$n_p = \frac{n_i^2}{N_A} \tag{1.10}$$

N_D and N_A are the donor and acceptor doping densities respectively. Moreover, the dark current can be elevated by the recombination mechanisms when one of these processes dominates the diffusion current.

- Generation recombination (Shockley-Read-Hall - SRH) [29]: One of the most apparent recombination mechanisms is SRH recombination. The impurities in the semiconductor create localized energy states within the bandgap, which may trigger hole emission, hole capture, electron emission and electron capture processes. Due to the lack of carriers inside the depletion region, generation mechanism dominates the recombination rate and produces dark current.
- Tunneling dark currents [30]: Tunneling is another physical phenomena leading to the generation of dark current for the low bandgap semiconductor devices. This event can be either direct transition between valence and conduction bands (band-to-band, BTB) or indirect transition with the help of trap energy level inside the bandgap (trap-assisted-tunneling, TAT). The indirect process occurs in two steps. The first one is thermal transition of carriers between trap energy level and one of the bands, where the second step is the tunneling between the other band and the trap level. Trap-Assisted-Tunneling (TAT) process may be triggered with smaller fields than the direct

(band-to-band) transition since the required energy is higher for BTB tunneling.

- Auger recombination [31]: Auger recombination is a process, where the released energy from the recombination of one electron and hole is transmitted to another carrier. This energy transmission can be classified in three different processes.

  Auger-1 process is dominant in n-type semiconductors, where the excess energy is transferred to an electron. C_e is the Auger coefficient for electrons.

  $$r_{Auger\_1} = C_e n^2 p \tag{1.11}$$

  When a hole absorbs the energy, the process is named as Auger-7 and it is dominant in p-type doped regions. C_h is the Auger coefficient for holes.

  $$r_{Auger\_7} = C_h n p^2 \tag{1.12}$$

  For intrinsic materials, Auger-S process should be considered since both transitions are significant. $C_e \; and \; C_h$ are the Auger coefficients for electrons and holes.

  $$r_{Auger\_S} = C_e n^2 p + C_h n p^2 \tag{1.13}$$

- Radiative recombination [32]: An excited electron in a semiconductor can release its energy by emitting photons during the band-to-band recombination. This event is an intrinsic process, which may influence the characteristics of a direct bandgap semiconductor. Indirect bandgap semiconductors require phonon interaction to realize this process so radiative recombination rate is negligible for these materials. However, it may dominate the dark current for photon detectors since direct bandgap materials are used for the infrared detection. The net radiative recombination rate can be evaluated as,

  $$R_{radiative} = B(np - n_i^2) \tag{1.14}$$

  where B is the material dependent radiative recombination coefficient.

1.3.2. Photo Current

A photocurrent of a photovoltaic device can be evaluated in terms of optically generated charge density in diffusion region. For a system, where g_{op} optical generation rate, q is electron charge and A is the area of semiconductor, W is the

depletion region length, L_n and L_p are the diffusion length for p and n sides of the semiconductor.

$$I_{photo} = qAL_n g_{op} + qAW g_{op} + qAL_p g_{op} \tag{1.15}$$

As can be seen in the above equation, the photo current is limited by the diffusion length since the EHPs generated outside of this region cannot be collected.

1.4. Infrared Photodetector Characteristics & Figures of Merit

In order to appraise the performance of IR detector, the fundamental parameters are needed to be considered. IR detection figures of merit are represented below and explained briefly.

1.4.1. Responsivity

Responsivity is a measure of the observed signal level for a unit incoming light power. Responsivity can be calculated either for voltage signal (voltage responsivity) and current signal (current responsivity). It provides information about the collection of photo-generated carriers and an important benchmark for the infrared detection. The spectral responsivity can be evaluated using the following relation.

$$R = \frac{output\ signal}{incoming\ flux} = \frac{i_{photo}\,(A)\ or\ v_{photo}(V)}{\phi\,(W)} \tag{1.16}$$

The photon responsivity can be evaluated regardless of the energy (and wavelength) of the incident light showing the device response with respect to the incoming photon number. The photon responsivity can be found using Equation 1.17.

$$R_p = \frac{i_{photo}\,(A)\ or\ v_{photo}(V)}{\phi\,(photons/sec)} \tag{1.17}$$

Above the cutoff wavelength, the absorption is expected to be zero due to the insufficient amount of energy to generate electron-hole pair for the semiconductor device. This means that responsivity is a function of wavelength and it is entitled as

spectral responsivity. Typically, the peak responsivity and the frequency spectrum are measured separately in order to find spectral responsivity. Ideally, incident light with any wavelength below cutoff should be absorbed and contribute to the photo current level. Therefore, the spectral photon responsivity should be constant below the cutoff wavelength. Moreover, when we consider incoming flux in Watts, the spectral responsivity increases linearly as shown in the **Figure 1.5** since the energy of a single photon inversely proportional with the wavelength (Equation 1.18).

$$E_{photon} = \frac{hc}{\lambda} \tag{1.18}$$

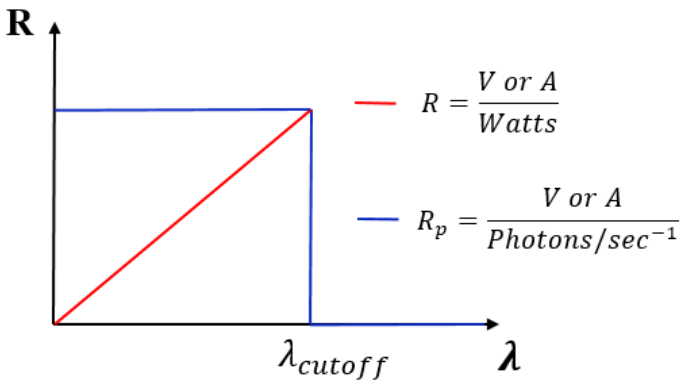

Figure 1.5: Responsivity profile with respect to the wavelength.

1.4.2. Quantum Efficiency

Quantum efficiency (QE) represents the percentage of photo-generated electron-hole pairs to the number of incoming photons. This parameter is an important benchmark for the infrared detection in terms of light-electric conversion efficiency. Due to absorption, reflection and the electrical properties of the semiconductor device may result in a decrease in QE. External quantum efficiency is defined so that the absorption performance of the device is conceived. One major parameter is the reflection from the surface of the detector. However, it is possible to minimize it with the utilization of anti-reflection coating. Reflection of an incident radiation normal to surface is governed by the formula,

$$R = \frac{(n-n_{air})^2+k^2}{(n+n_{air})^2+k^2} \tag{1.19}$$

where R is reflectance, k is the extinction coefficient, n and n_{air} are refractive index of semiconductor and air. The reflectance of well-known semiconductors (GaAs, Ge) may be around 30% so anti-reflection coating has a critical importance for high performance devices. When the anti-reflection coating is applied to the surface, reflected light is aimed to be minimized by the destructive interference for the desired range of wavelengths. When the extinction coefficient is negligibly small and the refractive index for the anti-reflection coating is n_{ar}, the reflectance can be evaluated as,

$$R = \left(\frac{n-n_{ar}}{n+n_{ar}}\right)^2 \tag{1.20}$$

Absorbed photon density exponentially changes inside the semiconductor (as shown in Equation 1.21).

$$I = I_0 e^{-\alpha x} \tag{1.21}$$

where I is the optical intensity inside the absorptive layer, I_0 is the optical intensity at the surface, α is absorption coefficient and x is the position. According to this relation, the absorption rate depends on the material. For instance, due to the high absorption coefficient of HgCdTe, the significant amount of absorption occurs in the first couple of micrometers for this material. Therefore, a certain size of the semiconductor device allows significant percentage of absorption depending on the optical properties of the semiconductor. Unless the absorber layer designed carefully, sensor suffers from the low absorption leading depredated external quantum efficiency.

Internal quantum efficiency is defined as the number of generated electrons per absorbed photon. In some cases, absorbed photons may not contribute to the photocurrent due to undesired electrical events. Specifically, recombination mechanisms, inappropriate band structure and non-ideal electrical contacts may disturb this parameter. The quantum efficiency of the device can be evaluated with the multiplication of external and internal quantum efficiencies as seen in the Equation 1.22.

$$\eta = \eta_{int} . \eta_{ext} = \frac{\eta_{int}(1-r)(1-e^{-\alpha x})}{(1-re^{-\alpha x})} \quad (1.22)$$

η_{ext} , η_{int} and η are external, internal and overall quantum efficiencies, α is the absorption coefficient, r is the reflection from the surface and x is the thickness of the absorptive layer. When a significant ratio of the photons are absorbed ($e^{-\alpha t} \ll 1$), the quantum efficiency can be approximated as follows,

$$\eta \simeq \eta_{int}(1-r) \quad (1.23)$$

1.4.3. Noise

Noise can be defined as the fluctuations in the measured signal, which directly influence the operation of the sensor. These fluctuations can be originated from different mechanisms.

- Thermal (Johnson) Noise [33]: It is originated from the random motion of carriers due to thermal energy. Thermal noise exists above 0 K temperature and increases as the temperature increases. Resistance of the semiconductor determines its significance.

  $$i_{n\_thermal} = \sqrt{\frac{4kT\Delta f}{R}} \quad (1.24)$$

  k is Boltzmann constant, T is temperature, R is the resistance of the device and Δf is the measurement frequency bandwidth.
- Shot Noise [34]: Random arrival of incoming photons generates fluctuations in the photocurrent level. Moreover, for photovoltaic photodetectors, transmission of the charge carriers over potential energy barrier may generate the similar effect.

  $$i_{n\_shot} = \sqrt{2qI\Delta f} \quad (1.25)$$

  q is electron charge, I is the current level and Δf is the measurement frequency bandwidth.
- Capacitor Noise: Capacitor noise based on the thermal noise generation on an RC circuit. The source of this noise is not the capacitor itself but the fluctuations in the charge on the capacitor. When the device resistance is very high, the thermal generation of carriers does not depend on the resistance since

the capacitance term dominates the noise generation. This noise is also known as kTC noise.

$$Q_{n\_cap} = \sqrt{kTC} \tag{1.26}$$

k is Boltzmann constant, T is temperature and C is the capacitance.

- 1/f (Pink) Noise [35]: Even though the source of the pink noise is not still discovered, the behavior of this event occurs in many physical, biological and economic systems. This stochastic process generates noise such that the energy for each octave in the frequency spectrum is equal. 1/f noise limits the low frequency detection since its noise spectrum is more significant in lower frequencies as shown in **Figure 1.6**.

$$S(f) = \frac{C}{f^{\alpha}} \tag{1.27}$$

$S(f)$ is noise spectrum density, C is constant, f is frequency and α is a real number ($0 < \alpha < 3$) typically close to 1.

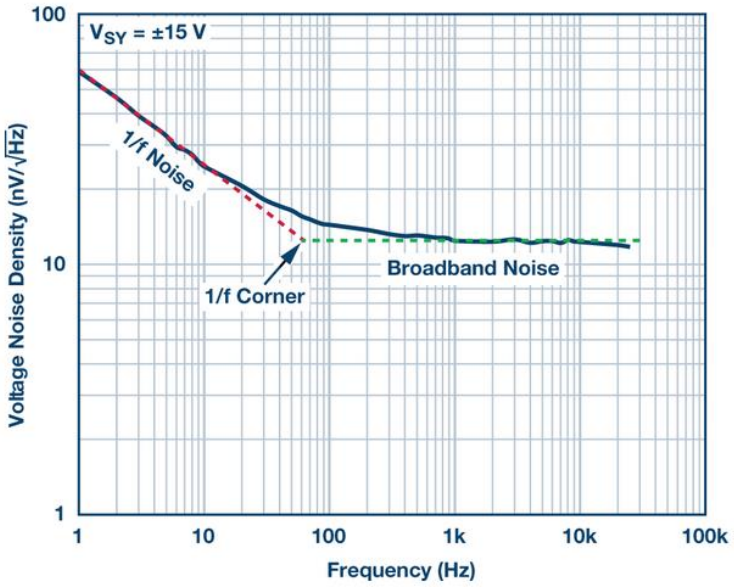

Figure 1.6: A representative 1/f noise spectrum [36].

1.4.4. Noise Equivalent Power (NEP)

NEP is a measure of flux in order to generate a signal that is equal to the noise level. In other words, it is the flux value, which produces the minimum detectable output signal. This parameter can be calculated as in the Equation 1.28.

$$NEP = \frac{\phi}{S/N}\ (W) \tag{1.28}$$

ϕ is flux and S/N is signal to noise ratio.

1.4.5. Detectivity

Detectivity is an important and comprehensive performance parameter for the infrared detectors. It is defined as follows,

$$D = \frac{1}{NEP}\left(\frac{1}{W}\right) \tag{1.29}$$

The detectivity depends on the detector area and noise measurement frequency bandwidth. For this reason, specific detectivity (D^*) is defined as a benchmark for comparison of different detectors in terms of performance. This parameter is independent of detector area and the noise bandwidth. Therefore, it is reliable measure for the performance assessment of infrared detectors.

$$D^* = \frac{\sqrt{A_d \Delta f}}{NEP} = \frac{\sqrt{A_d \Delta f}}{\frac{\phi}{S/N}} = \frac{R_i \sqrt{A_d \Delta f}}{i_{noise}}\left(\frac{cm\sqrt{Hz}}{W}\right) \tag{1.30}$$

1.4.6. Noise Equivalent Temperature Difference (NETD)

Noise Equivalent Temperature Difference (NETD) [37] is an important figure of merit, which can be considered in order to estimate thermal detection performance. The minimum temperature difference producing a signal level equal to the noise of the detector is defined as NETD. In other words, this parameter reveals the minimum detectable temperature difference. A good NETD is in the order of milikelvins for photon detectors providing a high contrast image. One should note that NETD is defined only for thermal imaging so it is useful for detection in MWIR and LWIR atmospheric windows. NETD can be evaluated using the following relation.

$$NETD = \frac{4(F/\#)^2 \sqrt{\Delta f}}{\sqrt{A_d} \int T(\lambda) D^*(\lambda) \frac{dM_\lambda}{dT} d\lambda}\ (K) \tag{1.31}$$

1.4.7. Background Limited Performance (BLIP)

In case the dominant noise mechanism is originated from the background flux, the detector performance is determined by the photon noise. In such a condition, the thermally generated noise mechanisms are insignificant for the sensor operation. The most prominent method to achieve BLIP operation is to decrease detector temperature and reduce the dominancy of the thermally generated noise mechanisms [37]. The temperature, which the photon noise starts to dominate noise of the detector, is defined as the BLIP temperature. This temperature is used as a benchmark for the comparison of high performance detectors. A detector that satisfies BLIP operation at a higher temperature benefits from reduced cooling cost and power dissipation.

In general, the overall detector noise contains a small amount of noise that is generated thermally, although they are much lower than the photon noise. In order to quantify this, the percentage of BLIP operation is introduced as in the Equation 1.32 [1].

$$\eta_{BLIP} = \left(\frac{N_{photon}^2}{N_{photon}^2 + N_{FPA}^2}\right)^{1/2} \tag{1.32}$$

where η_{BLIP} is BLIP ratio, N_{photon} and N_{FPA} are the number of carriers generated due to the incoming photons and the other noise mechanisms respectively. As can be observed, for a higher BLIP percentage, dominancy of the photon noise should be more significant; hence the signal to noise ratio is higher.

CHAPTER 2

HgCdTe PHOTODETECTORS

Mercury-Cadmium-Telluride (MCT - HgCdTe) is a special II-VI material alloy, which has unique electrical and optical properties. Therefore, it has drawn interest of a large number of universities and research institutes over decades for the state-of-the-art infrared detection [38]. HgCdTe can be epitaxially growth as a combination of CdTe and HgTe. These alloys have almost the same lattice constant, which allows growth of $Hg_{1-x}Cd_xTe$ in any composition without defects introduced by lattice mismatch. CdTe is a semiconductor and has a bandgap energy around 1.6 eV, where HgTe is semi-metal chemical compound with high conductivity. Therefore, a combination of these alloys forms a perfect material for the infrared detection due to the capability to select operation wavelength between 700 nm – 25 μm. For this reason, HgCdTe is extensively used material in third generation infrared detection and it has various types of applications. Moreover, high performance parameters of HgCdTe draw attention of defense industry and ability to design novel device structures further improves potential research activities.

2.1.Challenges for HgCdTe

2.1.1. P-type doping

For the design and development of state-of-art detectors, the control over the layer structures is essential where the precise adjustment of Cd composition and the doping concentrations push forward the detector performances even under challenging conditions. Stable and well-controlled composition profile and the n-type doping can be achieved using MBE growth method and in-situ indium doping. However, control

over p-type doing is still a fabrication challenge for HgCdTe. A specific type of defect (Hg vacancies) represents p-type behavior but the utilization of mercury vacancies as a dopant is not a convenient method due to several reasons. Firstly, these vacancies significantly decrease carrier mobility values and result in poor electrical characteristics. Secondly, it is not possible to control vacancy density precisely. Moreover, these Hg vacancies may create non-uniform diffusion barrier and hinder carrier to diffuse stably.

Utilization of p-type doping as an in-situ process is more preferable approach since the ex-situ diffusion and ion implementation methods do not have a wide range of flexibility on the doping density. Moreover, ion implementation process damages the atomic bonds and lowers the carrier lifetimes, which negatively influence the detector performance. P-type doping can be achieved by the replacement of Te with V group elements or replacement of (Cd/Hg) atoms with group I elements and the most commonly used dopant is Arsenic as a group V element to replace Tellurium [39]. After in-situ implementation of Arsenic, these atoms are located to Hg/Cd lattice sites and behave as n-type impurities. Therefore, another fabrication process needs to be addressed so that the Arsenic atoms can be placed to Te lattice sites, which is defined as Arsenic activation [40]. This process requires high temperatures in order to evaporate Te and fill these vacancies with Arsenic. A typical activation temperature is ~425° C and this process is called high temperature annealing. During this step, a significant amount of Hg vacancies is created. Another annealing process should be performed at temperatures near ~250° C under high Hg vapor pressure in order to eliminate negative effect of these vacancies. This process is called low temperature annealing and significantly improves semiconductor properties. After activation process, a uniform doping level can be achieved more than 10^{18} cm^{-3} density.

2.1.2. Substrate

Infrared detection industry and the research institutes aim to increase array sizes as well as reducing the cost in near future. One of the major limitations of HgCdTe technology is its substrate, where HgCdTe detectors are generally preferred to grow on lattice matched CdZnTe wafers [41]. Low quality substrates with high defect

densities introduce unbounded atomic bonds inside the semiconductor, which create leakage current on corresponding pixel. These pixels (dead pixels) will lose their detection ability due to excessive current level.

The ratio of functional pixels is one of the important performance parameter and it is desired to be higher than ~99% especially for high performance detection applications. Maintaining the same quality over the detector is restricted by the substrate size and defect density. However, high quality substrates with low defect densities are subject to export license issues. On the other hand, commercially available substrates suffer from small area and high cost [42] where the price of 1 cm^2 substrate is more than 100$. Lowering the cost of this technology is possible with the larger substrate size allowing mass production of detectors. However, they are still limited by 6 cm x 6 cm area, which is a modest value compared to the mature semiconductor materials [43].

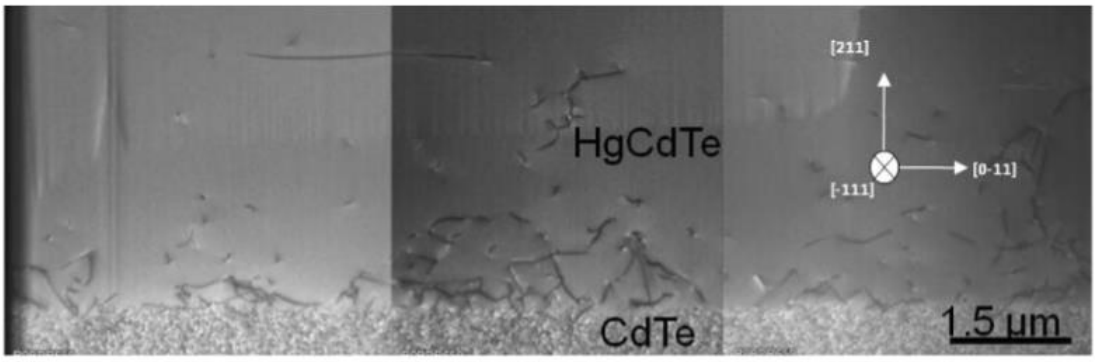

Figure 2.1: SEM image taken for HgCdTe material that is growth on alternative substrates [49].

In the last few decades, research authorities focused on alternative materials to replace CZT substrates to eliminate these disadvantages. Several mature semiconductor materials such as Ge, GaAs and Si, offer high crystal quality, large wafer size and low cost as a substrate [44-48]. However, all of these semiconductors have a notable amount of lattice mismatch with MCT. The high defect density originated by the lattice mismatch can significantly reduce carrier mobility and lifetimes. **Figure 2.1** represents the defects introduced by the lattice mismatch. As can be observed, the defects placed between the buffer layer (CdTe) and the detector layers (HgCdTe) significantly reduces the crystal quality. The lattice constants for different semiconductor materials as well as their bandgap energies are presented in **Figure 2.2**.

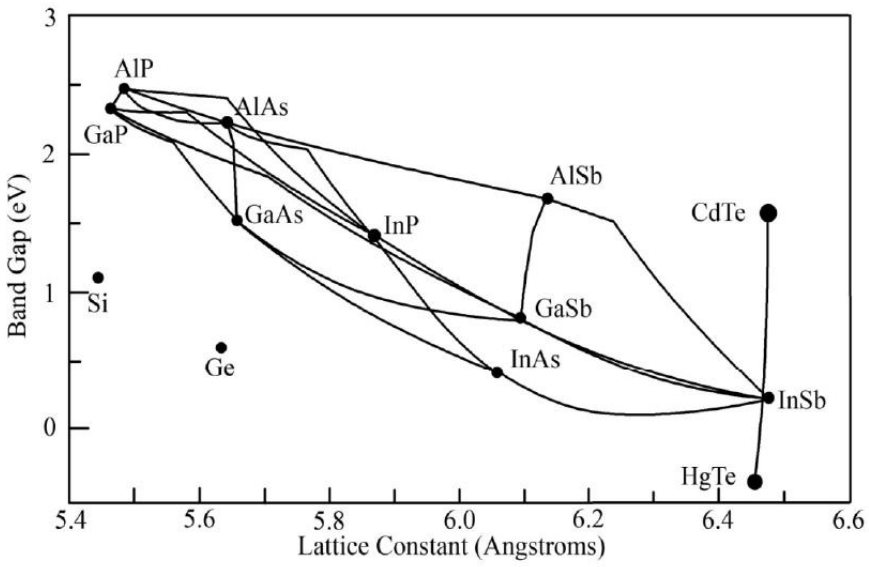

Figure 2.2: Lattice constant versus bandgap graph for commonly used infrared sensor materials [49].

Thermal expansion coefficient (TEC) is another important parameter for the evaluation of alternative substrates. A change in the temperature generates stress on the interface between layers with different thermal expansion coefficient and may lead to physical damage on sensor as well as deterioration in electrical properties. For this reason, substrate, read-out circuit and the device material are desired to have similar TEC. Even though lattice mismatch between Silicon and HgCdTe is higher than the ones for Ge and GaAs, a substantial amount of research focuses on this material. The main reason is that Silicon read-out circuits are generally combined with the infrared sensor by flip-chip process and the coupled sensor array generally operates under cooled temperatures (40 K - 300 K). By this way, the negative effects of the stress on epitaxial layers are aimed to be minimized.

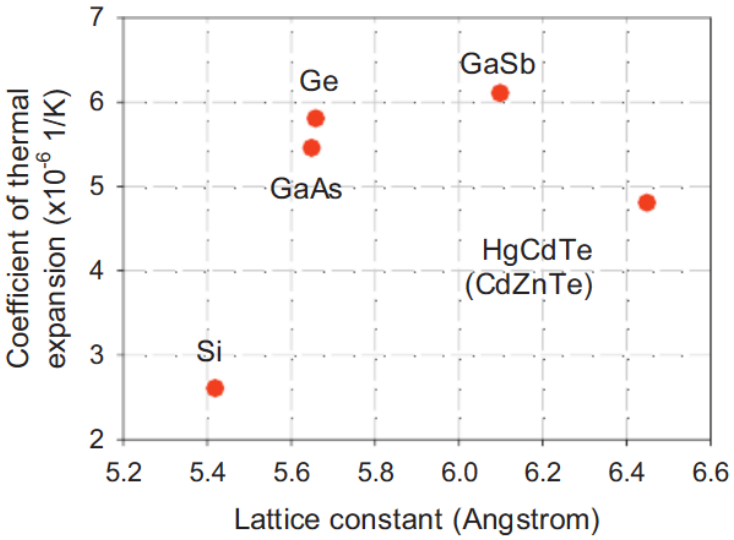

Figure 2.3: Thermal expansion coefficient for most commonly used alternative substrate materials and HgCdTe [47].

Dislocations created by the lattice mismatch disturbs the device operation and generates dead pixels. To overcome this issue, additional buffer layer can be utilized. X-ray diffraction (XRD) method is a well-known technique for the material characterization and process control, which can be used to identify quality of the alternative substrate. The parameters of lattice can be extracted by this measurement. Analysis of frequency spectrum peaks provides information on material type and quality. Moreover, stress/strain parameters can be measured by the Full Width Half-Maximum (FWHM) values of the peak. The disorders and structural deteriorations widens FWHM so the sharp peaks represent high crystal quality.

Another benchmark for the characterization of semiconductor materials is Etch Pit Density (EPD). Etch rate of the semiconductor is higher in the defected regions since surface area of the disordered section are larger which increases its interaction with the etchant. Due to the etch rate difference, pits are created on the surface corresponding to the defected regions. Therefore, the number of pits in a unit area can be useful for the estimation of crystal quality, where low EPD is desired for any semiconductor.

These techniques are the most reliable tools for the crystal quality assessment of alternative substrates. A major focus on the alternative substrate technology is on the reduction of dislocations in order to maintain high carrier lifetimes. For this purpose,

a thick CdTe layer between the detector and the substrate is a common approach to hinder the penetration of dislocations and minimize the stress on the lattice-mismatched interface.

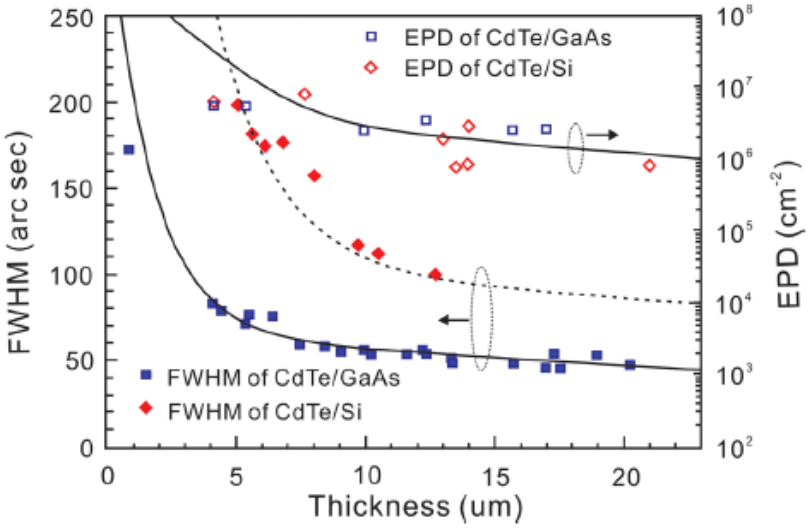

Figure 2.4: Etch pit density and the FWHM values of XRD measurements for HgCdTe detectors, which are growth on GaAs and Si [43].

Figure 2.4 represents XRD FWHM and EPD measurement results with respect to the CdTe buffer layer thickness for both Si and GaAs. As can be observed, increased buffer layer reduces EPD two orders of magnitudes (from $10^8\ cm^{-2}$ to $10^6\ cm^{-2}$). Moreover, a more apparent improvement is observed for the XRD FWHM measurements. For both GaAs and Si, FWHM values decreased almost five times reaching 50 arcsec for GaAs (100 arcsec for Si). Another important point is that the improvements on both parameters saturate for buffer layer thicknesses longer than ~10 μm. Therefore, ideal buffer layer thickness should be around this length.

Thermal cyclic annealing is an additional fabrication process [43], which aims to fix some of the dislocations and improve crystal quality. This process is carried out by short time periods and several cycles at high temperatures (i.e. 5 min at 400°C). It has been noted to be effective in terms of EPD and XRD measurements. However, such high temperature process after-growth might affect other atomic events such as diffusion. Therefore, a precise detector design may suffer from the undesired diffusion of dopants and lose the accuracy between epitaxial layers.

2.2. HgCdTe Detector Structures

2.2.1. Heterojunction Photodiode

The most prominent infrared detector structure is a simple photodiode with an appropriate cut-off wavelength [50-52]. A basic detector structure consists of an absorber and a cap layer. The absorber layer is designed for the optimum optic-electric conversion and determine electrical characteristics of the device together with the cap layer. Moreover, two metalized contact layers should be utilized for the successful collection of current values.

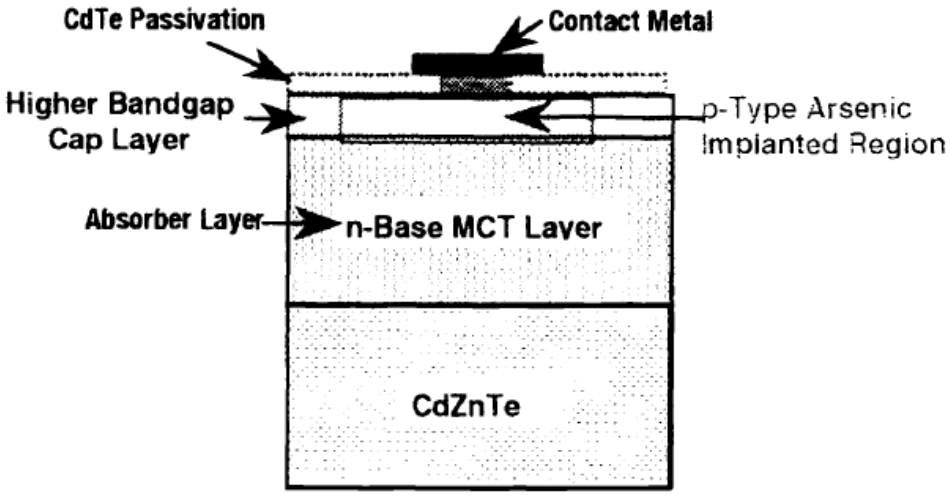

Figure 2.5: A heterojunction photodiode layer structure of the fabricated device including CdTe passivation layer [53].

Photo-generated carriers are transmitted through the device and form the photocurrent. A typical I-V characteristics of a photovoltaic detector is shown in **Figure 2.6**.

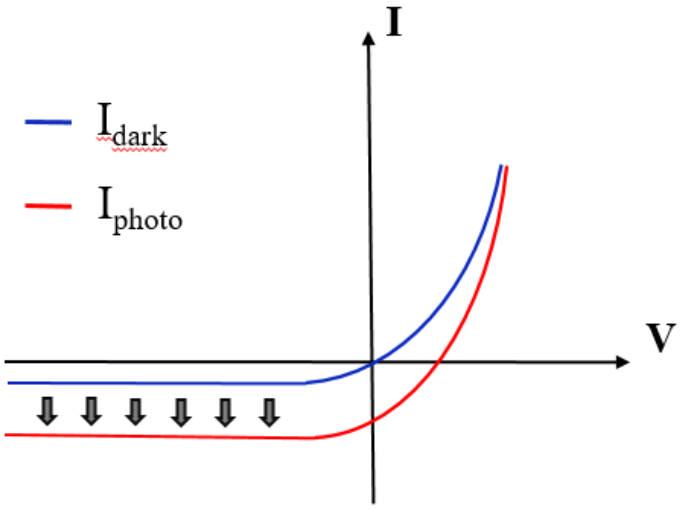

Figure 2.6: Typical I-V curve of a photodiode representing dark and photo currents.

A photo detector should be optimized so that absorption and the collection of photo-generated carriers are not disturbed. HgCdTe has a refractive index between 3.3 and 4.3 depending on the composition, which may result in a decrease in quantum efficiency by 28.6-38.7% due to the reflection on the surface. Hence, an anti-reflection coating should be used for a high performance detection. On the other hand, a device should have appropriate absorber layer length in order to absorb a significant amount of incoming radiation. One should note that absorber length should be designed considering many parameters such as material absorption coefficient, operation wavelength and temperature. For instance, the absorber layer length is typically around 2 μm for SWIR detectors, where this value is ~5 μm for MWIR and ~12 μm for LWIR sensors. Moreover, fabricated infrared detector usually receives radiation from the back surface through substrate so the detector should have a transparent substrate in desired range of wavelength. CdZnTe is the lattice matched substrate for HgCdTe. This substrate has ~1.5 eV bandgap energy, which makes this substrate transparent for wavelengths above ~830 nm. In other words, the incident radiation with a wavelength higher than ~830 nm can successfully reach to the detector layers passing through CdZnTe substrate.

Even though an optical performance degradation due to substrate is not problem for HgCdTe, it is very important for some detector material systems such as InSb. Since these detectors are ideally grown on the same material, InSb substrates should be

removed or grinded to a certain thickness to avoid losses due to the absorption in substrate.

Dark current level of a detector should be optimized by selecting proper doping and Cd compositions for absorber and cap layers. The composition of absorber layer is determined by the cut-off requirement; however, cap layer mole fraction may be considered as a design parameter. A higher Cd composition in cap layer is preferred in order to eliminate diffusion contribution of this layer since intrinsic carrier concentrations are lower for large bandgap HgCdTe layers. One important point is that an abrupt change in the composition may lead a discontinuity in conduction and valence bands depending on the composition variation, and it may disturb electrical characteristics of the sensor.

Furthermore, inconvenient doping levels may trigger recombination mechanisms, which may significantly increase the dark current level of the sensor. A higher doping density brings conduction and valence bands closer in depletion region and increases the tunneling probability. In addition, Auger recombination rate increases to significant levels, which negatively influences detector performance. On the other hand, for low doping densities, depletion region will be longer; hence, the effect of the generation-recombination process might be stronger. Optimum design parameters should be selected considering atmospheric window, operation temperature, performance requirements, cut-off wavelength and crystal quality.

2.2.2. Auger suppression

The most prominent dark current suppression method is Auger suppression [54-57]. A typical structure of Auger suppressed detectors contains two highly doped regions and an intrinsic (or lightly doped) layer in-between them. The layer structure can be represented as $P^+\pi N^+$, where P^+ and N^+ are wide bandgap, highly doped p-type and n-type regions and an intrinsic absorber layer is represented as π.

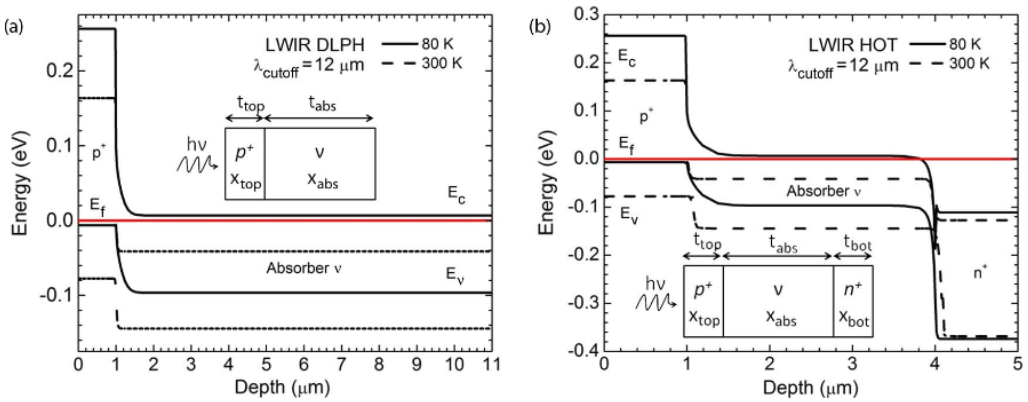

Figure 2.7: Layer structure and band diagram for **a)** a conventional heterojunction structure and **b)** Auger suppression detectors [56].

Auger recombination is an important dark current mechanism for MWIR and LWIR detectors [58-60] especially at elevated temperatures. Therefore, the aim of this structure is to suppress Auger recombination in order to increase operation temperature. Note that the intrinsic carrier density dominates the carrier density at high temperatures (>~100) in π region, even if this layer is lightly doped. Moreover, the intrinsic region in-between two highly doped regions (P^+ and N^+) is subject to the highest electrical field inside the sensor and constant through this layer. Therefore, absorber layer is completely depleted and the carrier densities are significantly decreased.

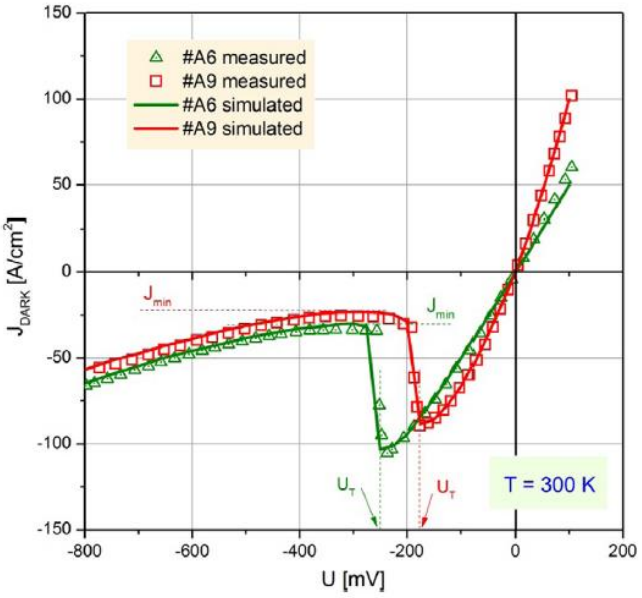

Figure 2.8: I-V characteristics of two Auger suppressed infrared detectors [61].

Furthermore, I-V curves of these devices reveal that this structure performs better at relatively high reverse bias voltages (<-0.2). However, it may stimulate tunneling dark currents especially for crystals with notable defects and dislocations.

2.2.3. Barrier Detectors

Utilization of unipolar barrier is another method for the suppression of dark current and noise mechanisms [62-69]. SRH and surface dark current are aimed to be suppressed so that the performance of the infrared sensor can be improved. Introducing a wide bandgap layer generates discontinuities in both valence and conduction band for HgCdTe material, where two sided barrier obstructs the carrier flow and significantly decreases photocurrent of the detector. However, a unipolar barrier in valence band (conduction band) allows photo-generated electrons (holes) to carry photocurrent. This structure can be optimized by the adjustment of bias voltage and doping profiles. Moreover, this methodology is appropriate for photoconductive structures as well as photovoltaic sensors. A photovoltaic (pBn) and a photoconductive (nBn) photodetector band diagrams are given in **Figure 2.9**.

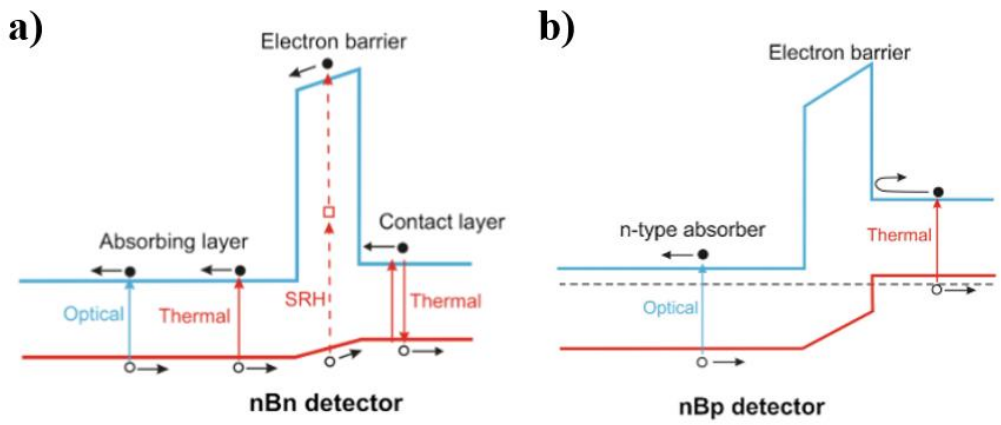

Figure 2.9: Band diagram for a) nBn and b) nBp detectors[70].

Unipolar barrier structures (nBn, pBp, nBp etc.) significantly reduce SRH recombination rate with the help of high bandgap barrier layer. Moreover, the presence of a high bandgap barrier effectively reduces the surface leakage, which might be the dominant dark current mechanism of the infrared detector. In particular, nBn detector structures do not suffer from controllability issues of p-type doping for HgCdTe

materials, which enhances the crystal quality due to lack of Hg vacancies and defects. However, utilization of p-type doped barrier layer in order to remove valence band discontinuity enhances depleted regions between absorber and barrier layers. Due to p-type doping, significant portion of the depletion region relies on intrinsic or lightly doped absorber region and this process results in notable amount of SRH recombination.

2.2.4. Multi Band Detectors

Utilization of multi band infrared detector structures in a single semiconductor offers significant advancements in terms of recognition and detection capabilities [71-73]. Detection configurations in different atmospheric windows have certain characteristics and advantages under different conditions. Multi-band detection allows combining these advantages in order to achieve advanced infrared detection applications. For instance, MWIR detectors benefits higher thermal contrast and the performance degradation due to the water vapor is less significant in MWIR band compared to LWIR band. However, mid-wave detectors more easily saturate due to the presence of hot objects. On the other hand, intensity of the emitted light from near room temperature object is significantly higher at LWIR wavelengths, which make these detectors more advantageous under low background radiation. Furthermore, combination of two detectors with different cutoff wavelengths in the same atmospheric band can be utilized for the advanced thermal detection applications.

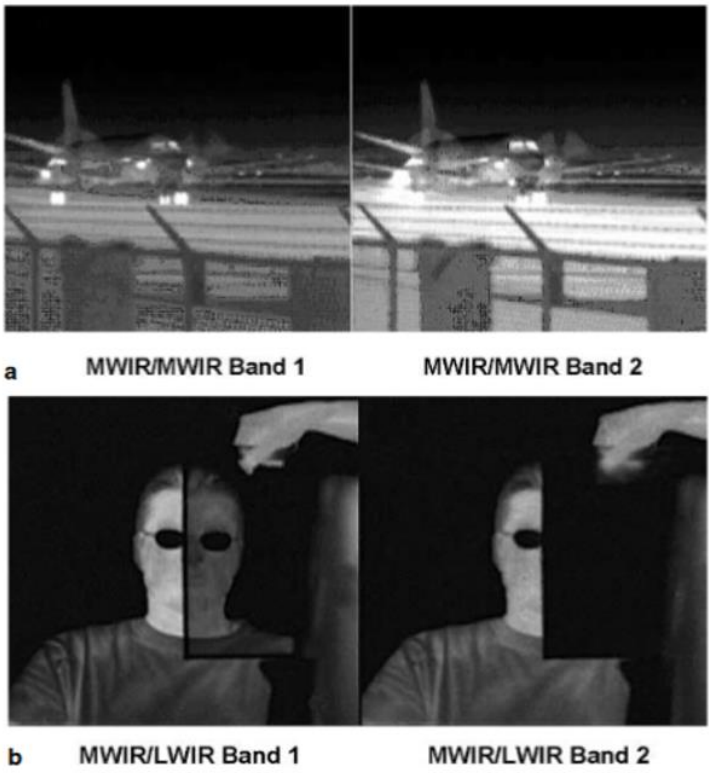

Figure 2.10: Images taken from **a)** MWIR/MWIR and **b)** MWIR/LWIR detectors under different operation wavelengths[73].

Additionally, the exact temperature of the object can be measured by the help of exitance difference in these regions. It is also possible to utilize SWIR-MWIR and SWIR-LWIR detectors. For these structures, abilities of SWIR detection are combined with the thermal detectors.

2.3. State of the Art in HgCdTe Detector Technology

Rule 07 [74] is an empirical model that estimates the dark current density for the state of the art HgCdTe infrared detectors. This model is proposed by a well-known infrared detector company, Teledyne Imaging Sensors (TIS), in 2008. The model is based on the measurement results of state of art ion-implanted pn HgCdTe detectors, which are grown by MBE method. Above 77 K temperature and for the products of cutoff wavelength and temperature $(\lambda_{cutoff}T)$ between $400\ \mu m.K - 1700\ \mu m.K$, this model successfully estimates the dark current density over 13 orders of magnitude range for HgCdTe detectors.

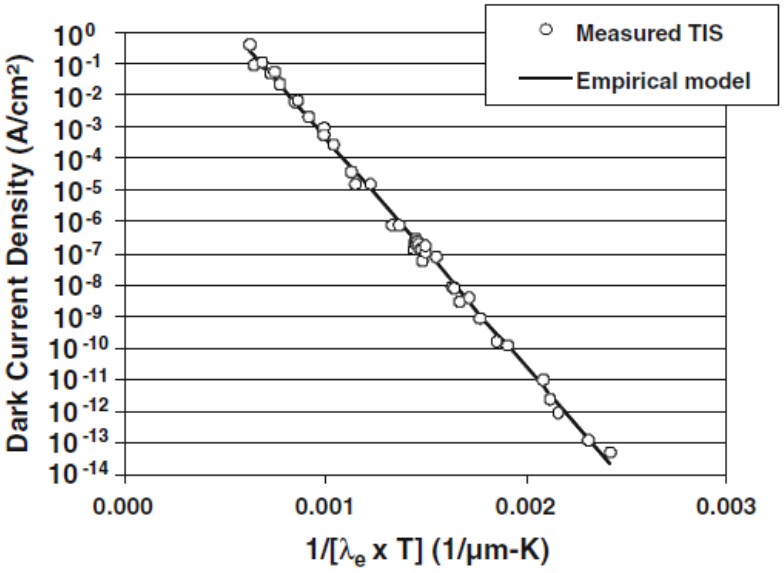

Figure 2.11: Dark current density values for measured detectors and the empirical model [74].

The proposed formulation [74, 75] representing the Rule 07 is illustrated as follows,

$$J = J_0 e^{C(1.24q/k\lambda_e T)} \tag{2.1}$$

$$\lambda_e = \lambda_{cut-off} \text{ for } \lambda_{cut-off} \geq \lambda_{threshold} \tag{2.2}$$

$$\lambda_e = \frac{\lambda_{cut-off}}{\left[1-\left(\frac{\lambda_{scale}}{\lambda_{cut-off}}-\frac{\lambda_{scale}}{\lambda_{threshold}}\right)^{Pwr}\right]} \text{ for } \lambda_{cut-off} \leq \lambda_{threshold} \tag{2.3}$$

The fit parameters presented in the above equations are given as, $J_0 = 8367.000019\ A/cm^2$, $Pwr = 0.544071282$, $C = -1.162972237$, $\lambda_{scale} = 0.200847413\ \mu m$ and $\lambda_{threshold} = 4.635136423\ \mu m$.

It is important to note that from 0.4 to 2.5 times variation in dark current density is given as the possible deviation of empirical fit from the data set. Another important point is that the data samples have variety of layer thicknesses between 4 µm to 10 µm. Moreover, the authors stated that the donor doping densities are typically in the range of $0.5 \times 10^{15} - 2 \times 10^{15}\ cm^{-3}$ and no adjustment has been made for the changes in the doping densities. Therefore, small variations might be acceptable depending on these parameters. However, this model is a reliable approximation for state of the art HgCdTe detector dark current densities over a wide range of cutoff and operation temperature products.

W.E. Tennant, et al. [74] concludes that the dark current densities of the state of the art LWIR HgCdTe detectors are dominated by Auger recombination, where SWIR detectors have defect states, which trigger SRH recombination. Furthermore, both mechanisms are reported to be exist in mid-wave detectors at a lower level.

J.B. Varesi et al. [76] represented 640 x 480 high quality sensor array, which is growth on MBE method. They compared their results with LPE grown detectors and showed that MBE grown HgCdTe detectors have similar or exceeding performance. In this study, 20-30 pA dark current values are reported at -20 mV bias and 140 K temperature for 20 μm x 20 μm pixel area. Furthermore, an increase in the 1/f noise is observed for the HgCdTe detectors with Si substrate compared to LPE material.

M. Zandian et al. [77] reported state-of-art HgCdTe detectors grown by MBE on CdZnTe material. They investigated the dark current performance of MWIR HgCdTe detectors and compared with the dark current values of InSb sensors in literature. HgCdTe detectors are reported to be diffusion limited where the dark current of InSb detectors are dominated by SRH recombination. On the other hand, for temperatures lower than 68 K, tunneling dark current mechanism is observed. The dark current density of $\sim 4.95 \times 10^{-10}\ A/cm^2$ is reached 1024 x 1024 HgCdTe detector at 100 K.

M.A. Kinch et al. [78] investigated the high operating temperature (HOT) detector concepts considering the range of thermoelectric cooler capabilities. Auger, radiative and SRH recombination lifetimes are measured for MWIR and LWIR detectors. For the Auger limited ultimate dark current values, improvement on the SRH recombination lifetime is stated to be essential.

C. Fulk et al. [79] analyzed the dark current data recorded at Raytheon Vision Systems for SWIR and MWIR HgCdTe detectors. The analysis model is stated to be similar to Rule 07 but it includes GR recombination term. The model includes only short and mid-wave region since the shunt and tunneling behavior is observed for narrow bandgap materials at low temperatures.

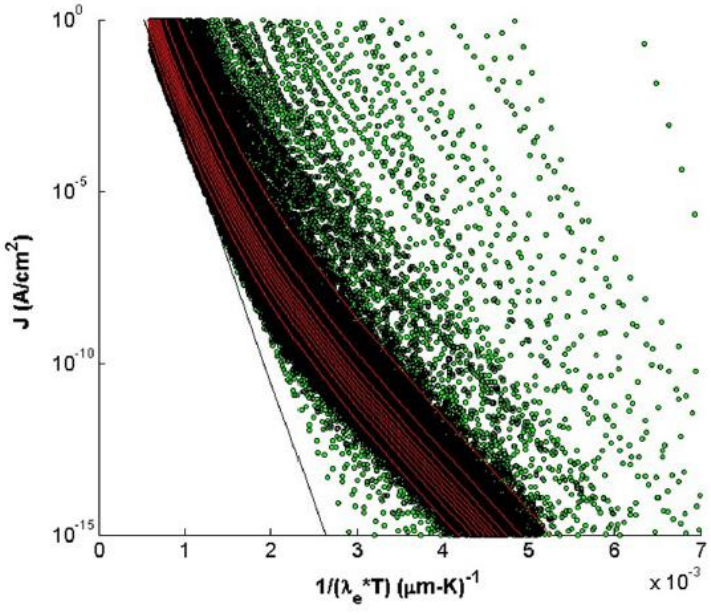

Figure 2.12: Dark current density values for measured detectors at Raytheon Vision Systems where the solid black line is diffusion current and the red lines are fit results for every 10% probability density interval within four orders of magnitude of the mean data [79].

As shown in the **Figure 2.12**, SRH dark current is present at lower temperatures and it dominates the detector performance. Moreover, the probability distribution is analyzed using the current data measured at Raytheon Vision Systems in order to determine manufacturing yield.

A. Kerlain et al. [80] analized NETD and 1/f noise values for MWIR detectors fabricated by Sofradir and CEA-LETI. The dark current density values are stated to be concordant with Rule 07 and 1/f noise contribution is not observed up to 220 K temperature.

2.4. Literature Survey on HgCdTe Detector Modeling

Development of advanced HgCdTe detector structures require deep understanding on electrical and optical properties of this material. For this purpose, a large number of studies are reported for HgCdTe detector modelling.

One common approach is to utilize a commercially available device simulation software such as Sentaurus Device [81-83] and ATLAS [84-87] for the numerical analysis of detector structures. Another method is to develop an electrical model, which solves Poisson, current and continuity equations.

J. Schuster et al. [88, 89] performed a numerical analysis on eSWIR HgCdTe detectors using the commercial software Sentaurus Device software. A dark current suppression method is proposed and performance parameters are represented. The dark current density for 1 μs and 20 μs SRH lifetimes are calculated, where the SRH recombination is dominant below 200 K. The dark current density and the quantum efficiency of the detectors are presented with respect to the junction depth. The results showed that the dark current densities are decreased significanlty by adjusting the position of pn junction for the represented structures without decreasing QE.

P. K. Saxena et al. [87] presented a numerical analysis of MWIR HgCdTe detectors. Electron affinity gradient, junction location and doping concentration have been investageted. Johnson and shot noise are considered for the detectivity calculations. The analysis has been made incorporating with Auger, radiative, SRH and tunneling mechanisms. The simulation model is offered as a design guideline to develop HgCdTe detector structures.

A. Rogalski et al. [90] presented a comparison of p-on-n and n-on-p detector structures. Auger, radiative and SRH recombinations are included to the mathematical model. R_0A products are found to be higher for p+-n junctions. The results show a good agreement with the experimental results and the discrepancies are explained with the surface leakage current.

J. Wenus et al. [91] theoretically analyzed the double layer heterojunction HgCdTe detectors at 77 K. Lateral collection of photocurrent is examined, where the effect of abrupt junction and the Cd composition change is analyzed. The author concluded that the change in the Cd composition between absorber and cap layers has no influence on the quantum efficiency and R_0A product.

J. V. Gumenjuk-Sichevskaja et al. [92] performed a theoretical study on HgCdTe detectors at 77K. SRH recombination and tunneling mechanisms are included to this model. The authors concluded that the only change in the simulation parameters is the trap density for high and low quality diodes.

K. Kosai [93] summarized the developments on numerical simulations HgCdTe detectors. The author concluded that lateral collection, tunneling and impact ionization are sensitive to the deviations in 3D. Moreover, 1D and 2D simulation environments

are not suitable for the calculation of leakage current and the R_0A products of the detector.

W. D. Hu et al. [94] performed a numerical analysis in 2D for dual color HgCdTe photovoltaic detector. Performance of the dual color detector has been studied considering absorber layer thickness and doping profile. The author made a conclusion that a higher doping density on absorber layer negatively effects the photo response of the detector.

C. A. Keasler et al. [95] performed 3D simulations for MWIR and LWIR HgCdTe detectors. Mesa and planar-type structures are compared considering surface damage and fabrication processes considering Auger, radiative and SRH recombination mechanisms.

A. Jozwikowska [96] investigated the effect of abrupt CdTe/HgCdTe passivation interface to the generation-recombination process and dark current performance. SRH, impact ionization, band-to-band and trap-assisted tunneling mechanisms are considered where the trap density is taken as $10^{14} cm^{-3}$. A need for the accurate estimation of dislocation density and trap ionization energy is highlighted.

2.5. Contributions of This Work

HgCdTe is currently one of the leading choices for the advanced applications due to its unique electrical and optical properties. These properties allow implementation of multi band detection and complex specialized layer structures. However, the state of art detector performances can only be achieved with the ideal micro-processing techniques and growth conditions. Due to the non-ideal conditions, defects and dislocations may be introduced during the fabrication, which negatively effects the dark current performance of the detector. Therefore, a significant number of research facilities and companies focus on improving the fabrication processes and optimize the growth conditions. One of the possible reasons that may generate dislocations in the semiconductor is the lattice mismatch of the alternative substrates. Si, Ge or GaAs substrates are studied extensively in order to minimize cost and availability issue of lattice matched CdZnTe substrates. However, poor electrical properties introduced by the significant lattice mismatch degrades the detector performances and generate

dislocations. Growth of thick CdTe buffer layers is one common approach to minimize defect and dislocation densities. However, even with this approach, low carrier lifetimes enhance the trap related dark current mechanisms.

In literature, a large number of alternative substrate studies focus on improving the crystal quality and carrier lifetimes. On the other hand, as an alternative approach, there is a need for specialized structures, which minimize the negative outcomes of lattice mismatched alternative substrates. The main objective of this thesis is to implement the dark current suppression method [88, 89] in order to minimize recombination rates in depletion region for alternative substrate detectors. Note that shunt leakage current may dominate the detector performance of the lattice-mismatched detectors. Moreover, dislocations may result in high shunt noise coefficient that might be greater than G-R noise coefficient. However, there is no well-established mathematical model in order to estimate the density, electrical properties of dislocations and the interactions between dislocations. Therefore, Auger, radiative, TAT and SRH recombinations are considered during the analysis. Low crystal quality of these detectors are represented by short SRH lifetimes during the simulations. For the detailed analysis and the design procedure, an in-house numerical tool, which solves Poisson, current and continuity equations is implemented. In addition, a commercially available software Sentaurus Device is also utilized to obtain current values. In this thesis, two different detector designs are represented for MWIR and SWIR windows. MWIR detector design focus on the elimination of SRH and TAT dark currents in alternative substrate detectors and improve operating temperature (or lower the dark current density at the same temperature). Similarly, the dark current density for SWIR detector structure is aimed to be decreased so that the alternative substrate HgCdTe detectors can be a relatively cheap alternative for SWIR detection. In this thesis, with the utilization of specialized detector structure, the performance of the alternative substrate detectors is aimed to be improved theoretically considering Auger, radiative, TAT and SRH recombinations.

CHAPTER 3

MATHEMATICAL MODEL & SIMULATION

The state-of-art infrared detector technology research focusses on improving detection capabilities with the utilization of novel and complex layer structures. Therefore, mathematical modeling and simulation tools became essential part of the design and development procedure. Specifically, HgCdTe that provides flexibility to utilize a wide range of Cd composition without any lattice mismatch takes tremendous amount of attention from academicians and sensor designers. In this thesis, the electrical characteristics of HgCdTe based detectors are investigated with an in-house numerical tool and the results are verified with a commercial software Sentaurus Device TCAD [97]. In-house simulation tool is capable of solving Poisson's, current and continuity equations as well as generation-recombination mechanisms for HgCdTe devices so that the cutting edge infrared detector performances can be advanced with the high precision in design parameters. Heterojunction detector structures are analyzed by using 1D uniform evaluation points at steady-state conditions.

3.1. Poisson's Equation

In a semiconductor device, it is necessary to solve Poisson's equation in order to determine carrier densities, electric field and thereby electrical potential inside the device in steady state. The well-known Poisson equation is given as in the Equation 3.1.

$$\nabla(\varepsilon\nabla\varphi) = -\rho_{charge} - \rho_{trap} \tag{3.1}$$

$\rho_{charge} = -q(p - n + N_D^+ - N_A^-)$ and ρ_{trap} is trap charge density, φ is electrical potential, q is a space charge, ε is permittivity constant, n and p are electron and hole densities, N_D^+ and N_A^- are the ionized donor and acceptor doping densities.

Assume that ε is constant through the device. For one-dimensional case, Poisson's equation is equal to the Equation 3.2.

$$\varepsilon \frac{d^2\varphi}{dx^2} = -q(p - n + N_D^+ - N_A^-) - \rho_{trap} \tag{3.2}$$

3.1.1. Normalization of Poisson Equation

Electron and hole density values can be defined in terms of electrical potential inside the device.

$$n = n_i e^{\left(\frac{q\varphi}{kT}\right)} \tag{3.3}$$

$$p = n_i e^{\left(-\frac{q\varphi}{kT}\right)} \tag{3.4}$$

According to the Taylor series expansion, any exponential function can be interpreted as in the Equation 3.5.

$$e^{\gamma} = 1 + \gamma + \frac{\gamma^2}{2!} + \frac{\gamma^3}{3!} + \frac{\gamma^4}{4!} + \cdots \tag{3.5}$$

For a very small number γ (in this tool for $\gamma < 0.3$), Equation 3.5 is approximately equal to Equation 3.6.

$$e^{\gamma} \approx 1 + \gamma \tag{3.6}$$

While solving this equation for electrical potential, in every iteration φ value slightly changes so we can substitute the statement above into 1D Poisson's equation. Assuming that trap charge density is negligible, the Poission's equation can be written as in the Equation 3.7.

$$\frac{d^2\varphi}{dx^2} = -\frac{q}{\varepsilon}\left(n_i e^{\left(-\frac{q\varphi}{kT}\right)} - n_i e^{\left(\frac{q\varphi}{kT}\right)} + \frac{qn_i}{kT}\gamma n_i e^{\left(-\frac{q\varphi}{kT}\right)} + \frac{qn_i}{kT}\gamma n_i e^{\left(\frac{q\varphi}{kT}\right)} + N_D^+ - N_A^-\right) \tag{3.7}$$

Define γ as the change in the potential in each step, so we can write $\gamma = \varphi^{new} - \varphi^{old}$ where φ^{old} is the present level of electrical potential and φ^{new} is the potential that will be calculated after one iteration.

After rewriting Equation 3.6 in terms of n, p, $\varphi^{new}$and φ^{old},

$$\frac{d^2\varphi^{new}}{dx^2} = -\frac{q}{\varepsilon}(p\ - n + N_D^+ - N_A^-) + \frac{q^2}{kT}(n+p)(\varphi^{new} - \varphi^{old}) \quad (3.8)$$

Normalization of the physical parameters is essential to solve coupled differential equations. Hence, φ is normalized with V_T, x is normalized with Debye length (L_D), which is defined in Equation 3.9.

$$L_D = \sqrt{\frac{\varepsilon kT}{q^2 n_i}} \quad (3.9)$$

$\bar{\varphi}$ and $\bar{x}$ are defined as normalized electrical potential and the position respectively and these parameters can be calculated as in the Equation 3.10 and Equation 3.11,

$$\bar{\varphi} = \frac{q\varphi}{kT} \quad (3.10)$$

$$\bar{x} = \frac{x}{L_D} \quad (3.11)$$

Then, $\bar{\varphi}$ and $\bar{x}$ is inserted into the Equation 3.8,

$$\frac{d^2\bar{\varphi}^{new}}{d\bar{x}^2} - (\bar{n} + \bar{p})\bar{\varphi}^{new} = -\left(\bar{p}\ - \bar{n} + \frac{N_D^+ - N_A^-}{n_i}\right) - (\bar{n} + \bar{p})\bar{\varphi}^{old} \quad (3.12)$$

3.1.2. Discretization of Poisson Equation

Solution of complex mathematical systems can be achieved by discrete solution methods with higher computation speed and accuracy compared to continuous systems. For this purpose, transfer of continuous parameters, variables and functions to a discrete data system is indeed necessary.

In this thesis, finite difference method is utilized for the accurate approximation of mathematical relations. A discrete equivalent of derivative can be estimated by using the definition of derivative.

$$\frac{df}{dx} = \lim_{h \to 0} \frac{f(x+h)-f(x)}{h} \cong \frac{f(x+h)-f(x)}{h} \tag{3.13}$$

h represents the evaluation frequency and $f(x)$ represents a continuous function of x. The relation shown in the Equation 3.13 is a good approximation only for very small h values. A significant change in the function may increase error rate to the undesired levels. Therefore, smaller h values should be used in order to maintain low mathematical error rate.

Let $x_1, x_2, x_3, \dots, x_n$ be members of an array representing the discrete evaluation points and f is the corresponding function. We can approximate the first derivative of f with different approaches.

$$f_n' = \frac{f(x_{n+1})-f(x_n)}{h} \tag{3.14}$$

$$f_n' = \frac{f(x_n)-f(x_{n-1})}{h} \tag{3.15}$$

$$f_{n+\frac{1}{2}}' = \frac{f(x_{n+1})-f(x_n)}{h} \tag{3.16}$$

The relations in Equations 3.14 - 3.16 are known as forward difference, backward difference and central difference methods. The central difference method can be considered as more accurate than forward and backward difference methods for the same value of h. This method provides the derivative at the middle of two points and it is usually preferred in FEM simulation tools using Voronoi tessellation diagram for box discretization [98].

Higher order derivatives can be estimated by above methods. The central difference method is utilized in order to obtain second order derivative of f.

$$f_n'' = \frac{f\left(x_{n+\frac{1}{2}}\right)-f\left(x_{n-\frac{1}{2}}\right)}{h} \tag{3.17}$$

$$f_n'' = \frac{\frac{f(x_{n+1})-f(x_n)}{h} - \frac{f(x_n)-f(x_{n-1})}{h}}{h} \tag{3.18}$$

$$f_n'' = \frac{f(x_{n+1})-2f(x_n)-f(x_{n-1})}{h^2} \tag{3.19}$$

Then, finite difference equations are inserted into the Equation 3.12,

$$\frac{\bar{\varphi}_{n+1}^{new}}{\bar{x}^2} - \left(\bar{n}_n + \bar{p}_n + \frac{2}{\bar{x}^2}\right)\bar{\varphi}_n^{new} + \frac{\bar{\varphi}_{n-1}^{new}}{\bar{x}^2} = -\left(\bar{p}_n - \bar{n}_n + \frac{N_D^+ - N_A^-}{n_i}\right) - (\bar{n}_n + \bar{p}_n)\bar{\varphi}_n^{old} \tag{3.20}$$

3.1.3. Heterojunction of Poisson Equation

For heterojunction devices, solution of the Poisson's equation needs to be modified due to the changes in material properties. Specifically, the variation in the dielectric constant should be included in 1D Poisson's equation as the following equation.

$$\nabla\varepsilon\nabla\varphi + \varepsilon\nabla^2\varphi = -\rho_{charge} - \rho_{trap} \tag{3.21}$$

For single dimension, the above equation can be written as in the Equation 3.22.

$$\frac{d\varepsilon}{dx}\frac{d\varphi}{dx} + \varepsilon\frac{d^2\varphi}{dx^2} = -q(p - n + N_D^+ - N_A^-) - \rho_{trap} \tag{3.22}$$

Equation 3.22 is rewritten as,

$$\frac{d^2\varphi^{new}}{dx^2} = -q(p\ - n + N_D^+ - N_A^-) + \frac{q^2}{kT}(n + p)(\varphi^{new} - \varphi^{old}) - \frac{d\varepsilon}{dx}\frac{d\varphi^{old}}{dx} \tag{3.23}$$

After normalization, Equation 3.23 can be written as,

$$\frac{d^2\bar{\varphi}^{new}}{d\bar{x}^2} - (\bar{n} + \bar{p})\bar{\varphi}^{new} = -\left(\bar{p}\ - \bar{n} + \frac{N_D^+ - N_A^-}{n_i}\right) - (\bar{n} + \bar{p})\bar{\varphi}^{old} - \frac{1}{\varepsilon}\frac{d\varepsilon}{d\bar{x}}\frac{d\bar{\varphi}^{old}}{d\bar{x}} - \frac{\rho_{trap}}{qn_i} \tag{3.24}$$

In discrete data system, the Poisson's equation can be written as in the Equation 3.25.

$$\frac{\bar{\varphi}_{n+1}^{new}}{\Delta x^2} - \left(\bar{n}_n + \bar{p}_n + \frac{2}{\Delta x^2}\right)\bar{\varphi}_n^{new} + \frac{\bar{\varphi}_{n-1}^{new}}{\Delta x^2} = -\left(\bar{p}_n - \bar{n}_n + \frac{N_D^+ - N_A^-}{n_i}\right) - (\bar{n}_n + \bar{p}_n)\bar{\varphi}_n^{old} - \frac{1}{\varepsilon_n}\frac{\varepsilon_{n+1} - \varepsilon_n}{\Delta x}\frac{\bar{\varphi}^{old}{}_{n+1} - \bar{\varphi}^{old}{}_n}{\Delta x} - \frac{\rho_{trap}}{qn_i} \tag{3.25}$$

3.2. Mathematical Solution Methods

3.2.1. Successive Over Relaxation Method

Normalized and discretized mathematical equations can be solved with several analytical methods. The first model utilized in this thesis is Successive Over Relaxation (SOR) method [99, 100]. This method is an extension of a well-known analytical method known as Gauss-Seidel method [101], which can be utilized to solve a linear system of equations iteratively. Any system of equations can be solved using this method. In each iteration, only one element is evaluated and overwritten as the computation proceeds. In addition, for SOR model, a dumping parameter (ω) is defined so, that speed and accuracy of the solution can be adjusted.

- For an under-damped condition, damping parameter is between zero and one and the precision is maximized. However, the number of iterations until the finalization of computation is increased.
- For a damping parameter $1 < \omega < 2$, system is over-damped where the system reaches the final solution faster.
- When $\omega = 1$, the system is exactly same with the Gauss-Seidel method.
- For $\omega \geq 2$, the equation system cannot reach a solution due to the high oscillation between iterations.

A scheme of this method can be summarized as the following matrixes.

$$[C][\varphi] = [F] \tag{3.26}$$

$[C]$ is named as coefficient matrix, which consist of constants of electrical potential of consecutive iteration points in Equation 3.24. $[F]$ represents the forcing term matrix, which includes the right-hand-side (RHS) of the Equation 3.25 and $[\varphi]$ represents the electrical potential for each evaluation points.

Moreover, boundary conditions should be satisfied and inserted in the numerical model. Dirichlet boundary condition [102] states that the corresponding values of the system of equations are fixed in the boundary, which is electrical potential for the

solution of Poisson's equation. Knowing that, coefficient matrix should be in the form that is shown in Equation 3.27.

$$[C] = \begin{bmatrix} 1 & 0 & 0 & & 0 & 0 & 0 \\ a_1 & b_1 & c_1 & \cdots & 0 & 0 & 0 \\ 0 & a_2 & b_2 & & 0 & 0 & 0 \\ & \vdots & & \ddots & & \vdots & \\ 0 & 0 & 0 & & b_{n-3} & c_{n-3} & 0 \\ 0 & 0 & 0 & \cdots & a_{n-2} & b_{n-2} & c_{n-2} \\ 0 & 0 & 0 & & 0 & 0 & 1 \end{bmatrix} \tag{3.27}$$

The first and the last row of the given matrix are equal to one, which satisfy the Dirichlet boundary condition. It ensures that the applied voltages to the electrical contacts determine the electrical potential values at these points. a, b and c are the coefficients of each iteration term in normalized and discrete Poisson's equation and can be written as in Equation 3.28 and Equation 3.29.

$$a_n = c_n = \frac{1}{\Delta x^2} \tag{3.28}$$

$$b_n = \frac{2}{\Delta x^2} + \bar{n}_n + \bar{p}_n \tag{3.29}$$

The electrical potential values and electron and hole densities are evaluated by considering the doping and intrinsic carrier densities and used as initial condition for the input matrix $[\varphi]$. In each iteration, the potential values in the matrix are renewed as well as the carrier densities. The change in these parameters are taken into account in the following iteration until the system reaches a solution.

For the Gauss-Seidel method, the algorithm of the solution is given as in the following relation.

$$\bar{\varphi}_n^{new} = \frac{F_n - \sum_{m=1}^{n-1} C_{nm} \bar{\psi}_m^{new} - \sum_{m=n+1}^{n} C_{nm} \bar{\psi}_m^{old}}{b_{nn}} \tag{3.30}$$

In this relation, n and m represent the coordinates in the coefficient matrix. The damping parameter is defined so that the regeneration of the solution can be controlled. With the damping parameter, the evaluation result and the values in the previous iteration are mixed. This approach based on the adjustment of the variation between solutions of iterations. In other words, the correction in the corresponding iteration multiplied by the damping parameter and added to the old value. For instance, an over-

damped system with $w = 1.2$ renews the potential values with $1.2 \times \Delta\varphi$ instead of $\Delta\varphi$. Therefore, the final solution can be reached faster for over-damped situations. It should be noted that over-damping might result in a decaying oscillation around the exact solution. On the other hand, under-damped system approaches the result with monotonic and restrained steps leading high accuracy and slower computation. The solution equation with damping parameter is represented with Equation 3.31.

$$\bar{\varphi}_n^{new} = (1-\omega)\bar{\varphi}_n^{old} + \omega \frac{F_m - \sum_{m=1}^{n-1} C_{nm}\bar{\psi}_m^{new} - \sum_{m=n+1}^{n} C_{nm}\bar{\psi}_m^{old}}{b_{nn}} \tag{3.31}$$

The rate of convergence and the error analysis are two important parameters for iterative solvers. In each iteration, error rate should be evaluated so that the convergence rate can be estimated until the desired accuracy in solution. The error rate can be evaluated as in Equation 3.32.

$$error_n = \frac{F_n - \sum_{m=1}^{n-1} C_{nm}\bar{\psi}_m^{new} - \sum_{m=1}^{n} C_{nm}\bar{\psi}_m^{old}}{b_{nn}} - \bar{\varphi}_n^{old} \tag{3.32}$$

The error function is constituted by the electrical potential correction in each iteration. This evaluation reveals the change of electrical potential in a single point between two consecutive iteration, which can be used for the interpretation of convergence.

3.2.2. LU Decomposition Method

In this thesis, LU decomposition method [99, 100] is also utilized as an alternative mathematical approach to the successive over relaxation method. The coefficient matrix in the Equation 3.26 is a tridiagonal matrix and can be written as a combination of two matrices. $[L]$ and $[U]$ are defined as the lower and upper triangular matrices and they satisfy the following relations.

$$[C] = [L][U] \tag{3.33}$$

$$[C][\varphi] = [L][U][\varphi] = [F] \tag{3.34}$$

Above the diagonal, $[L]$ has only zero elements and $[U]$ has zeros below the diagonal. Equation 3.33 can be rewritten as in the following relation.

$$\begin{bmatrix} b_1 & c_1 & 0 & \cdots & 0 & 0 & 0 \\ a_2 & b_2 & c_2 & & 0 & 0 & 0 \\ & \vdots & & \ddots & \vdots & & \\ 0 & 0 & 0 & \cdots & b_{n-1} & c_{n-1} & 0 \\ 0 & 0 & 0 & \cdots & a_n & b_n & c_n \end{bmatrix} = \begin{bmatrix} 1 & 0 & \cdots & 0 & 0 \\ \beta_2 & 1 & & 0 & 0 \\ \vdots & & \ddots & \vdots & \\ 0 & 0 & & 1 & 0 \\ 0 & 0 & \cdots & \beta_n & 1 \end{bmatrix} \begin{bmatrix} \alpha_1 & c_1 & \cdots & 0 & 0 \\ 0 & \alpha_2 & & 0 & 0 \\ \vdots & & \ddots & \alpha_{n-1} & \vdots \\ 0 & 0 & \cdots & 0 & c_{n-1} \\ 0 & 0 & & 0 & \alpha_n \end{bmatrix} \tag{3.35}$$

In the above expression, $[L]$ and $[U]$ matrices contain unknown elements (α, β) and they should be expressed as functions of a, b and c. From the matrix multiplication, the following relations can be found.

$$\alpha_1 = b_1 \tag{3.36}$$

$$a_2 = \alpha_1 \beta_2 \tag{3.37}$$

$$\beta_2 = \frac{a_2}{\alpha_1} \Rightarrow \beta_k = \frac{a_k}{\alpha_{k-1}} \tag{3.38}$$

k represents the mesh point and also the row number of coefficient matrix where it is positive integer smaller than the size of $[C]$. The Equation 3.35 also yields,

$$b_2 = c_1 \beta_2 + \alpha_2 \tag{3.39}$$

$$\alpha_2 = b_2 - c_1 \beta_2 \Rightarrow \alpha_k = b_k - c_{k-1} \beta_k \tag{3.40}$$

The solution can be divided into two parts as in the following relations.

$$[V] = [U][\varphi] \tag{3.41}$$

$$[L][V] = [F] \tag{3.42}$$

As a first step, solution of the Equation 3.41 should be found.

$$\begin{bmatrix} v_1 \\ v_2 \\ \vdots \\ v_{n-1} \\ v_n \end{bmatrix} = \begin{bmatrix} \alpha_1 & c_1 & \cdots & 0 & 0 \\ 0 & \alpha_2 & & 0 & 0 \\ & \vdots & \ddots & & \vdots \\ 0 & 0 & & \alpha_{n-1} & c_{n-1} \\ 0 & 0 & \cdots & 0 & \alpha_n \end{bmatrix} \begin{bmatrix} \varphi_1 \\ \varphi_2 \\ \vdots \\ \varphi_{n-1} \\ \varphi_n \end{bmatrix} \tag{3.43}$$

Then,

$$v_n = \alpha_n \varphi_n \tag{3.44}$$

$$\varphi_n = \frac{v_n}{\alpha_n} \tag{3.45}$$

The potential values in matrix φ_n for any integer n can be evaluated as in the following equations.

$$v_{n-1} = \alpha_{n-1}\varphi_{n-1} + c_{n-1}\varphi_n \tag{3.46}$$

$$\varphi_n = \frac{v_n - c_n\varphi_{n+1}}{\alpha_n} \tag{3.47}$$

Then, the elements in $[V]$ matrix can be found from the following equation.

$$\begin{bmatrix} f_1 \\ f_2 \\ \vdots \\ f_{n-1} \\ f_n \end{bmatrix} = \begin{bmatrix} 1 & 0 & \cdots & 0 & 0 \\ \beta_2 & 1 & & 0 & 0 \\ \vdots & & \ddots & \vdots & \\ 0 & 0 & & 1 & 0 \\ 0 & 0 & \cdots & \beta_n & 1 \end{bmatrix} \begin{bmatrix} v_1 \\ v_2 \\ \vdots \\ v_{n-1} \\ v_n \end{bmatrix} \tag{3.48}$$

This equality yields,

$$f_1 = v_1 \tag{3.49}$$

$$f_2 = \beta_2 v_1 + v_2 \tag{3.50}$$

$$f_k = \beta_k v_{k-1} + v_k \tag{3.51}$$

$$v_k = f_k - \beta_k v_{k-1} \tag{3.52}$$

3.3. Solution of Electron and Hole Continuity Equations

After solving a Poisson equation, electron and hole continuity equations should be satisfied in order to obtain accurate electric characteristic of a semiconductor device. The continuity equations for electrons and holes are given in Equation 3.53 - 3.54.

$$J_n = q\mu_n n\left(-\frac{d\varphi}{dx}\right) + qD_n\left(\frac{dn}{dx}\right) \tag{3.53}$$

$$J_p = q\mu_p p\left(-\frac{d\varphi}{dx}\right) - qD_p\left(\frac{dp}{dx}\right) \tag{3.54}$$

Generation in a semiconductor directly influences the current densities and it can be modelled as in the following relations.

$$\frac{dJ_n}{dx} = qG \tag{3.55}$$

$$\frac{dJ_p}{dx} = -qG \tag{3.56}$$

where G is net generation rate. Let's assume that the carrier densities in the middle of two grid points change linearly,

$$n_{n+\frac{1}{2}} = \frac{n_{n+1}+n_n}{\Delta x} \tag{3.57}$$

Then,

$$J_{n+\frac{1}{2}} = q\mu_n n_{n+\frac{1}{2}}\left(-\frac{\varphi_{n+1}-\varphi_n}{\Delta x}\right) + qD_n\left(\frac{n_{n+1}-n_n}{\Delta x}\right) \tag{3.58}$$

$$J_{n+\frac{1}{2}} = n_{n+1}\left(-q\mu_n\frac{\varphi_{n+1}-\varphi_n}{\Delta x} + q\frac{D_n}{\Delta x}\right) - n_n\left(q\mu_n\frac{\varphi_{n+1}-\varphi_n}{\Delta x} + q\frac{D_n}{\Delta x}\right) \tag{3.59}$$

In most cases, diffusion term in this equation much smaller than the drift term so the term $q\frac{D_n}{\Delta x}$ can be neglected. After this approximation, Equation 3.59 yields that electron density (n_{n+1}) will be equal to the negative of previous density ($-n_n$) for the equilibrium condition ($J_n = 0$) resulting in oscillation in the solution. In other words, this solution is not physically meaningful. Therefore, linear variation of the carrier densities between two grid points is not a suitable approach.

Scharfetter and Gummel [103] provided a solution to this carrier density discretization problem by assuming that the carrier densities between the grid points changes exponentially.

Take electron current equation under steady state,

$$\frac{dJ_n}{dx} = qG \tag{3.60}$$

$$\frac{J_{n+\frac{1}{2}}-J_{n-\frac{1}{2}}}{\Delta x} = qG_n \tag{3.61}$$

Insert $J_{n+\frac{1}{2}}$ (Equation 3.59),

$$\frac{dn}{dx} - n\frac{\mu_{n+\frac{1}{2}}}{D_{n+\frac{1}{2}}}\frac{\psi_{n+1}-\psi_n}{\Delta x} = \frac{J_{n+\frac{1}{2}}}{qD_{n+\frac{1}{2}}} \tag{3.62}$$

Rewrite the Equation 3.61,

$$\frac{dn}{dx} = \frac{dn}{d\varphi}\frac{d\psi}{dx} = \frac{\psi_{n+1}-\psi_n}{\Delta x}\frac{dn}{d\varphi} \tag{3.63}$$

$$\frac{dn}{d\varphi} - \frac{n}{V_t} = \frac{\Delta x}{q(\psi_{n+1}-\psi_n)}\frac{J_{n+\frac{1}{2}}}{D_{n+\frac{1}{2}}} \tag{3.64}$$

Define carrier densities as a function of electrical potential,

$$n(\psi_n) = n_n, n(\psi_{n+1}) = n_{n+1}, \ldots \tag{3.65}$$

After taking Laplace transform, electron concentration can be presented as

$$n(x,\psi) = n_n(1 - g(x,\psi)) + n_{n+1}g(x,\psi) \tag{3.66}$$

where $g(x,\psi)$ is the growth function at a point having electrical potential of ψ and represented as,

$$g(x,\psi) = \frac{1-exp\left(\frac{\psi_{n+1}-\psi_n}{V_t}\frac{x-x_n}{\Delta x}\right)}{1-exp\left(\frac{\psi_{n+1}-\psi_n}{V_t}\right)} \tag{3.67}$$

The limit of central growth function ($g(x+\frac{1}{2})$) is ½ for only the case $\psi_{n+1} - \psi_n = 0$ which satisfies $n_{n+\frac{1}{2}} = \frac{n_{n+1}+n_n}{\Delta x}$.

Inserting growth function to the current density equation of electrons,

$$J_{n+\frac{1}{2}} = \frac{qD_{n+\frac{1}{2}}}{\Delta x}\left(n_{n+1}B\left(\frac{\psi_{n+1}-\psi_n}{V_t}\right) - n_nB\left(\frac{\psi_n-\psi_{n+1}}{V_t}\right)\right) \tag{3.68}$$

$$J_{n-\frac{1}{2}} = \frac{qD_{n-\frac{1}{2}}}{\Delta x}\left(n_nB\left(\frac{\psi_n-\psi_{n-1}}{V_t}\right) - n_{n-1}B\left(\frac{\psi_{n-1}-\psi_n}{V_t}\right)\right) \tag{3.69}$$

For holes,

$$J_{n+\frac{1}{2}} = \frac{qD_{n+\frac{1}{2}}}{\Delta x}\left(p_{n+1}B\left(\frac{\psi_{n+1}-\psi_n}{V_t}\right) - p_nB\left(\frac{\psi_{n+1}-\psi_n}{V_t}\right)\right) \tag{3.70}$$

$$J_{n-\frac{1}{2}} = \frac{qD_{n-\frac{1}{2}}}{\Delta x}\left(p_{n-1}B\left(\frac{\psi_n-\psi_{n-1}}{V_t}\right) - p_nB\left(\frac{\psi_{n-1}-\psi_n}{V_t}\right)\right) \tag{3.71}$$

Equation 3.68 and 3.69 are inserted into the 1D electron current equation,

$$\frac{qD_{n+\frac{1}{2}}}{\Delta x^2} n_{n+1} B\left(\frac{\psi_{n+1}-\psi_n}{V_t}\right) - n_n \left(\frac{qD_{n-\frac{1}{2}}}{\Delta x^2} B\left(\frac{\psi_n-\psi_{n-1}}{V_t}\right) + \frac{qD_{n+\frac{1}{2}}}{\Delta x^2} B\left(\frac{\psi_n-\psi_{n+1}}{V_t}\right)\right) + \frac{qD_{n-\frac{1}{2}}}{\Delta x^2} n_{n-1} B\left(\frac{\psi_{n-1}-\psi_n}{V_t}\right) = G_n \quad (3.72)$$

Equation 3.70 and 3.71 are inserted into the 1D hole current equation,

$$\frac{qD_{n-\frac{1}{2}}}{\Delta x^2} p_{n-1} B\left(\frac{\psi_n-\psi_{n-1}}{V_t}\right) - p_n \left(\frac{qD_{n-\frac{1}{2}}}{\Delta x^2} B\left(\frac{\psi_{n-1}-\psi_n}{V_t}\right) + \frac{qD_{n+\frac{1}{2}}}{\Delta x^2} B\left(\frac{\psi_{n+1}-\psi_n}{V_t}\right)\right) + \frac{qD_{n+\frac{1}{2}}}{\Delta x^2} p_{n-1} B\left(\frac{\psi_n-\psi_{n+1}}{V_t}\right) = G_n \quad (3.73)$$

Diffusion coefficients and carrier mobility values can be assumed linearly varying between the grid points.

$$D^{elect}_{n+\frac{1}{2}} = \frac{D^{elect}_{n+1} - D^{elect}_{n}}{2} \quad (3.74)$$

$$D^{hole}_{n+\frac{1}{2}} = \frac{D^{hole}_{n+1} - D^{hole}_{n}}{2} \quad (3.75)$$

Bernoulli function is represented as B in the above equations and can be evaluated as follows.

$$B(x) = \frac{x}{\exp(x)-1} \quad (3.76)$$

3.4. HgCdTe Material Properties

Modelling and characterization of HgCdTe have been studied extensively and these studies proposed empirical formulations for the electrical and optical material properties. In this section, the mathematical expressions that are utilized as a part of in-house numerical tool are represented.

3.4.1. Bandgap

Bandgap of HgCdTe semiconductor is a function of both temperature and the Cd composition [104-106] and it can be determined by,

$$E_g = -0.302 + 1.93x + 5.35 \times 10^{-4} \times (1 - 2x) \times (-1882 + T^3) \div (255.2 + T^2) - 0.810x^2 + 0.832 \times x^3 \; eV \quad (3.77)$$

where T is temperature and x is Cd mole fraction. The flexibility on the Cd mole fraction is a prominent way to adjust bandgap energy since the lattice mismatch is negligible for any composition of HgCdTe. The change in the bandgap is shown in **Figure 3.1** at 78K.

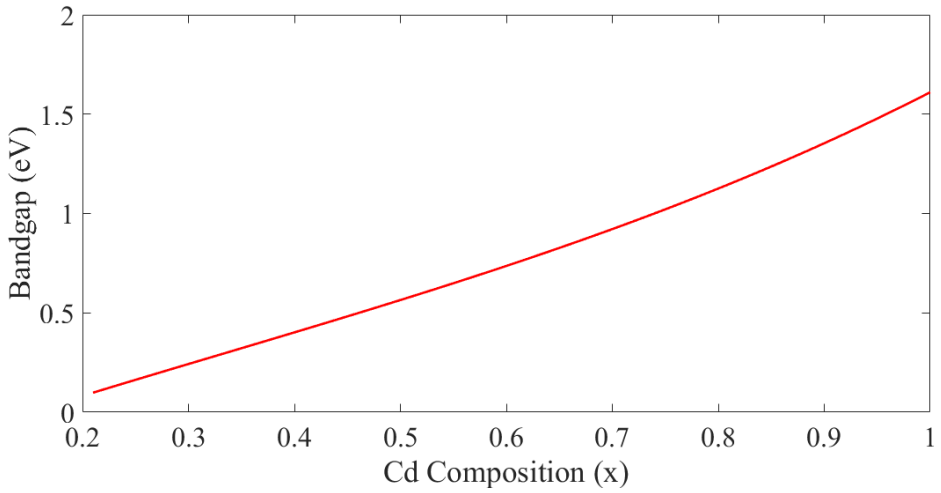

Figure 3.1: Bandgap of HgCdTe with respect to the Cd composition at T=100 K.

It can be observed that the bandgap energy significantly changes with the Cd mole fraction improving the design capabilities of scientists. Furthermore, temperature also has an impact on this parameter. **Figure 3.2** represents the change in the bandgap with respect to the temperature change when $x = 0.3$.

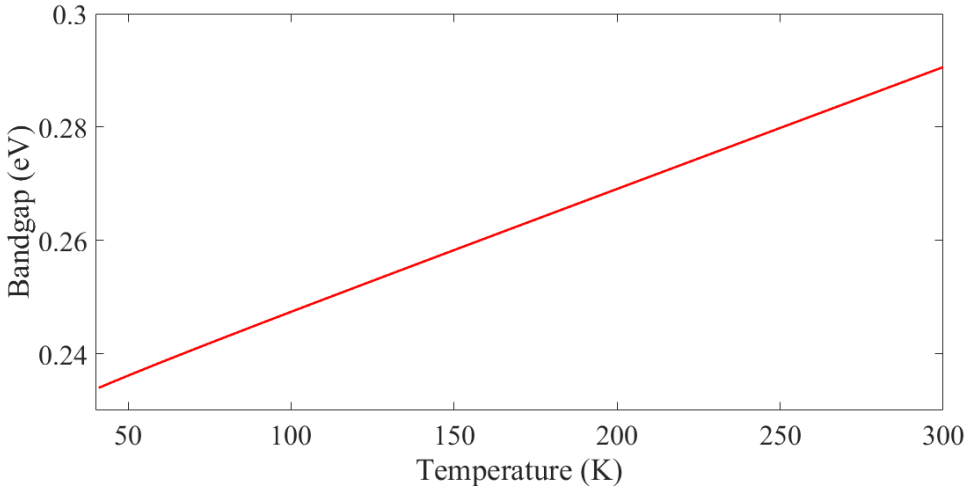

Figure 3.2: Bandgap of HgCdTe with respect to the device temperature for $x = 0.3$.

As represented above, higher temperatures also increase bandgap energy and changes the cutoff value of the infrared detector. Therefore, cutoff wavelength should be defined for the desired operation temperature. Nonetheless, it should be noted that the variation of band energy is less sensitive to temperature when compared to the Cd composition.

3.4.2. Intrinsic Carrier Density

Intrinsic carrier density has a significant role for the determination of electrical properties of a semiconductor. Major dark current components originating from diffusion and recombination mechanisms are functions of intrinsic carrier density so it has a direct impact on the detector performance. At any temperature above 0 K, thermal generation begins, where the electrons in valence band start to reach conduction band. The number of carriers participate in this transition constitute the intrinsic carrier density and can be evaluated as in Equation 3.78 [105, 106].

$$n_i = (5.24256 - 3.5729x - 4.74019T \times 10^{-4} + 1.25942 \times 10^{-2} \times (xT) - 5.77046x^2 - 4.24123 \times 10^{-6} \times T^2) \times 10^{14} \times {E_g}^{0.75} \times T^{1.5} \times e^{-E_g \times e/(2kT)}\ cm^{-3} \quad (3.78)$$

An increasing temperature enhances the thermal energy and increases the intrinsic carrier density as shown in **Figure 3.3**.

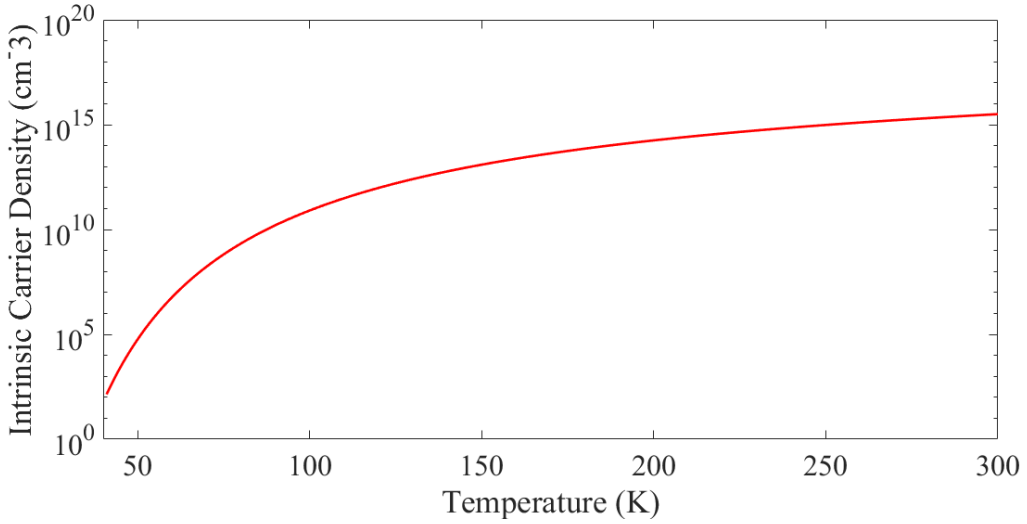

Figure 3.3: Intrinsic carrier density of HgCdTe with respect to the temperature for x = 0.3.

Moreover, a larger bandgap introduces higher energy barrier for thermally generated carriers and hinders the conduction between potential bands. For this reason, intrinsic carrier density significantly decreases with the increasing bandgap energy. In other words, intrinsic carrier density is lower for a greater Cd composition as represented in **Figure 3.4**.

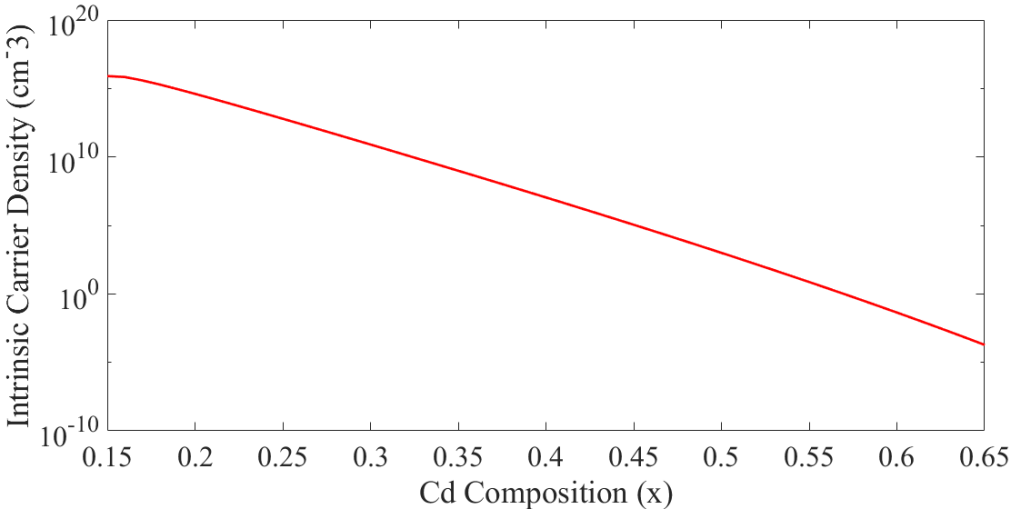

Figure 3.4: Intrinsic carrier density of HgCdTe with respect to the Cd mole fraction at T=100 K.

3.4.3. Permittivity

The dielectric constant of the HgCdTe can be also estimated as a function of mole fraction. It should be noted that solution of the Poisson's equation requires special consideration for the heterojunction structures since the change in the permittivity has a direct impact on solution. The permittivity [107] can be evaluated by Equation 3.79.

$$\varepsilon = (20.5 - 15.6\mathrm{x} + 5.7x^2)\ \varepsilon_0 \tag{3.79}$$

The permittivity in vacuum is given as, $\varepsilon_0 = 8.854 \times 10^{-12}\ {}^{F}/_{m}$.

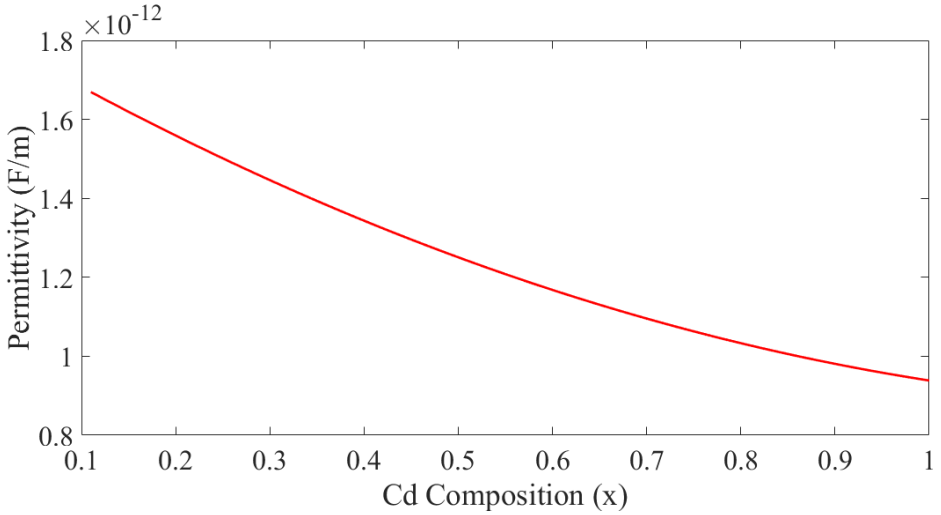

Figure 3.5: Dielectric constant of HgCdTe with respect to the Cd mole fraction at T=100 K.

3.4.4. Mobility

HgCdTe has a very high electron mobility, which is one of the unique properties of this material. The electron mobility [105, 106] is given by,

$$\mu_e = 9 \times 10^8\ \mathrm{b}/(T^{2a})\ cm^2/\mathrm{V.s} \tag{3.80}$$

where $a = (0.2/x)^{0.6}$ and $b = (0.2/x)^{0.75}$.

It can be observed that increasing temperature results in elevated mobility values as in **Figure 3.6**.

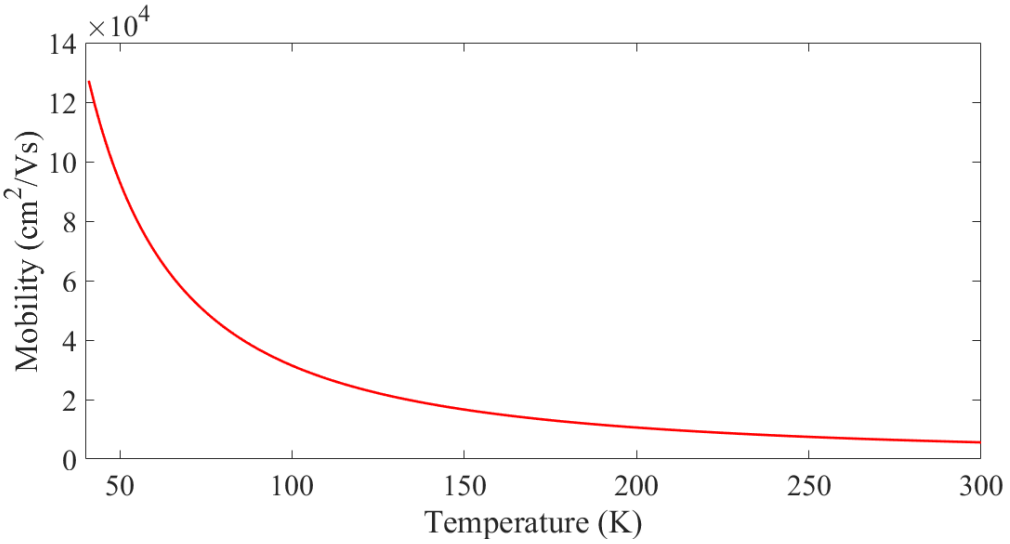

Figure 3.6: Electron mobility of HgCdTe with respect to the temperature for $\boldsymbol{x = 0.3}$.

Furthermore, electron mobility decreases as the Cd composition increases as shown in **Figure 3.7**.

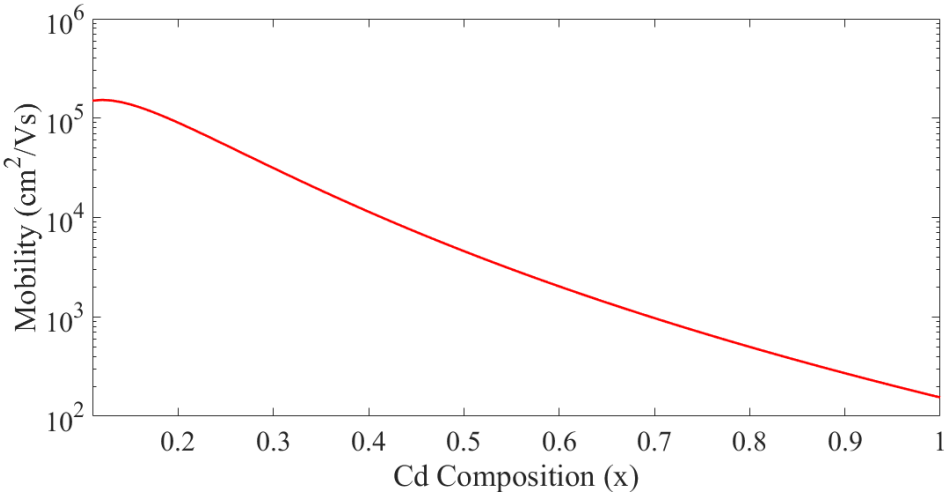

Figure 3.7: Electron mobility of HgCdTe with respect to the Cd composition at T=100 K.

The hole mobility is assumed to be very low compared to electron mobility and modelled as,

$$\mu_h = \frac{\mu_e}{100} \tag{3.81}$$

3.4.5. Electron Affinity & Band Potentials

Electrical characteristics of an infrared detector can be estimated by the help of band diagram, where events such as band bending, discontinuity and alignment are

indicators of the performance parameters. Therefore, band diagram is a useful tool for the infrared detector designers. For heterojunction devices, change in the bandgap energy results in discontinuities or variations in energy bands. However, valence and conduction bands are not influenced from this variation in the same extent. For accurate estimation, a term electron affinity is defined as the energy difference between bottom of conduction band and the vacuum energy level. The electron affinity [107] is given by,

$$\varphi_{affinity} = 4.23 - 0.813 \times (E_g - 0.083) \tag{3.82}$$

Then, the band potentials can be evaluated as,

$$E_c = -\varphi_{affinity} - \varphi \tag{3.83}$$

$$E_v = -\varphi_{affinity} - \varphi - E_g \tag{3.84}$$

where E_c and E_v are the conduction and valence band energy levels. The electrical potential evaluated as a solution of Poisson's equation introduces the bending effect originating from the doping levels. The amount of bending and its length provides information about the junction parameters and internal electrical field. On the other hand, band discontinuities are formed by the affinity level.

3.5. Recombination Models

3.5.1. Shockley-Read-Hall Process

Dislocations, defects and GR centers inside the depletion region introduce traps in energy bandgap, which trigger generation-recombination events. SRH recombination rate [29] is given as in Equation 3.85.

$$R_{SRH} = \frac{pn - n_i^2}{\tau_p\left(n + n_i e^{\frac{-E_{trap}}{kT}}\right) + \tau_n\left(p + n_i e^{\frac{E_{trap}}{kT}}\right)} \tag{3.85}$$

E_{trap} is the trap energy level with respect to the intrinsic fermi level.

3.5.2. Auger Recombination

Auger recombination [108] is modelled as in the Equation 3.86 considering both Auger 1 and Auger 7 processes.

$$R_{Aug} = (G_{Ae} \cdot n + G_{Ah} \cdot p) \times (np - n_i^2) \tag{3.86}$$

The electron and hole Auger constants G_{Ae} and G_{Ah} are given by,

$$G_{Ae} = \frac{\left(\frac{m_0}{m_e}\right)|F_1F_2|^2}{2n_i^2 3.8\times10^{-18}\varepsilon_{r\_hf}^2 + \left(1+\frac{m_e}{m_{hh}}\right)^{0.5}\left(1+\frac{2m_e}{m_{hh}}\right)}\left(\frac{E_g}{kT}\right)^{-1.5} \times e^{-\left[\frac{1+2\frac{m_e}{m_{hh}}E_g}{1+\frac{m_e}{m_{hh}}kT}\right]} \tag{3.87}$$

$$G_{Ah} = G_{Ae}\left[\frac{1-\frac{3E_g}{kT}}{6\left(1-\frac{1.25E_g}{kT}\right)}\right] \tag{3.88}$$

where ε_{r_hf} is high frequency permittivity, $|F_1F_2|$ is overlap integral, m_0, m_e and m_{hh} are electron rest mass, electron effective mass and heavy hole mass. These parameters are utilized as in the Table 3.1.

Table 3.1: Properties of HgCdTe [106-109].

ε_{r_hf}	$(15.2 - 15.6 \times x + 8.2 \times x^2)$
$\|F_1F_2\|$	0.15
m_0	$9.10938215 \times 10^{-31} kg$
m_e	$0.006937 \times m_0$
m_{hh}	$0.55 \times m_0$

3.5.3. Radiative Recombination

For complete and reliable analysis of state-of-art infrared detector performances, the radiative recombination is also implemented in this study. The following relation describes the amount of net radiative recombination [108].

$$R_{rad} = G_R \times (np - n_i^2) \tag{3.89}$$

where G_R is radiative generation rate which is given in Equation 3.90.

$$G_R = 5.8 \times 10^{-13} \varepsilon_{r\_hf}^{0.5} \left(\frac{m_0}{m_e+m_{hh}}\right)^{1.5} \times \left(1+\frac{m_0}{m_e}+\frac{m_0}{m_{hh}}\right) \times \left(\frac{300}{T}\right) \times \left[E_g^2 + 3kTE_g + 3.75k^2T^2\right] \quad (3.90)$$

3.5.4. Trap-Assisted-Tunneling (TAT)

In order to quantify effect of trap assisted tunneling, Hurkx tunneling model is utilized [110]. This model assumes that the carrier lifetimes are shortened due to the trap assisted tunneling factor. With this modification, SRH recombination model is updated as in Equation 3.91.

$$R_{SRH} = \frac{pn-n_i^2}{\frac{\tau_p}{1+\Gamma_p}\left(n+n_i e^{\frac{-E_{trap}}{kT}}\right)+\frac{\tau_n}{1+\Gamma_n}\left(p+n_i e^{\frac{E_{trap}}{kT}}\right)} \quad (3.91)$$

Γ_n and Γ_p are trap-assisted-tunneling factor for electrons and holes respectively. When the internal electric field is weak, these constants are less than one and this recombination rate can be approximated as the conventional SRH term. When electric field is very high, the bending in depletion region increases significantly, which may increase the tunneling probability and the trap-assisted-tunneling factor. Therefore, the effective carrier lifetimes are decreased that represents the tunneling effect.

CHAPTER 4

ALTERNATIVE SUBSTRATE MWIR HgCdTe INFRARED DETECTOR DESIGN

Increasing the operating temperature of HgCdTe detectors is one of the major challenges for the infrared detector technology. In general, the dark current level limits the maximum operation temperature for specified performance parameters. As mentioned in the previous sections, mechanisms constituting the dark current level are functions of intrinsic material properties and the junction parameters. However, adjustment of them may not be possible in conventional double layered heterojunction structures. Within the scope of this study [111, 112], a modified version of the generation-recombination dark current suppression method [88, 89] is utilized so that the operation temperature is increased significantly for the same detection requirements.

A substantial amount of research have focused on improving the crystal quality and their fabrication for alternative substrate HgCdTe detectors [113-115]. Even though the modest improvements have been achieved in this regard, these detectors are not comparable with the detectors with lattice-matched substrate (CdZnTe). Due to the degraded crystal quality, SRH recombination rate dominates the dark current for short SRH carrier lifetimes. In this study, SRH recombination is suppressed by introducing a wide bandgap material into the depletion region and the dark current density is significantly reduced for alternative substrate HgCdTe detectors. This suppression method [88, 89] is effectively used for the elimination of disadvantages introduced by the poor electrical properties of alternative substrates.

In this chapter, design procedure and the suppression method are represented in detail including performance and sensitivity analysis towards variations in properties of detector layers.

4.1. Device Parameters

A conventional double-layer p-n heterojunction (DLH) structure and a depletion engineered heterojunction (DEH) structure are designed and compared in terms of detection performance. As a first step of detector design, absorption of the incoming light is needed to be optimized. The cutoff wavelength of the detector is desired to be 5 μm which covers the mid-wave infrared atmospheric transmission window. Bandgap energy of the absorber layer should be selected carefully to satisfy this requirement and it can be found as,

$$E_g(eV) = \frac{1.24}{\lambda_{cutoff}(\mu m)} = \frac{1.24}{5\ \mu m} = 0.248\ eV \tag{4.1}$$

For this purpose, the appropriate Cd mole fraction is found as $x = 0.3$ using the Equation 3.76, where the corresponding bandgap energy is $E_g = 0.2476\ eV$ at 100 K.

The designed detector structures aim to sense near room temperature objects. Therefore, the target is assumed to be 300 K, which perfectly represents a human body temperature. Depending on the weather conditions and the geographic regions, atmospheric molecules may lower the transmission of emitted light to the detector. Considering the realistic circumstances, 20% of the emitted radiation is assumed to be lost due to scattering and absorption events [21]. In addition, the reflection at the surface may be another reason for degradation in the signal level. However, in this study, detectors are assumed to have an anti-reflection coating, which minimizes the reflection. Also, during the simulations, f/2 [116] optics is assumed to be used as a part of imaging system. For the given conditions, $3 \times 10^{-5}\ W/cm^2$ radiation is evaluated to reach detector considering the illumination between 3-5 μm [22]. During the simulations, detectors are exposed to the evaluated radiation in 4 μm wavelength, which corresponds to $3.773 \times 10^9\ photons/s$.

Another design parameter is the length of absorber layer. This length should guarantee that a significant ratio of the incoming photons can be absorbed contributing to the

generation of electron-hole pairs. Absorption process has an exponential behavior so the absorbed photon density gets lower as the distance from the surface increases. **Figure 4.1** represents the absorbed photon density (per 1 cm^3 volume) inside the device, where the photon density at the surface is $\sim 6 \times 10^{14}$ $photons/cm^2.s$ for the conditions specified above.

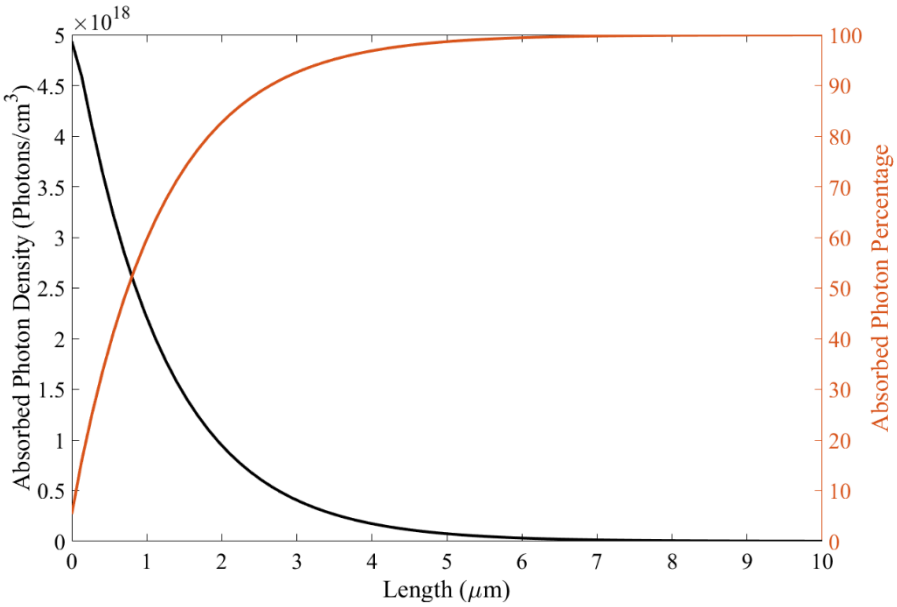

Figure 4.1: Absorbed photon density (per volume) and the absorption rate inside the HgCdTe detector with 5 µm cutoff at T=100 K obtained from Sentaurus Device.

As seen in this figure, most of the absorption process occurs in the first several micrometers. It is a fact that a longer layer guarantees higher absorption ratio of photons. Collection of incoming light can be increased up to ~100% by this way. However, the longer device (within the diffusion length) may generate excessive dark current due to the increased diffusion volume. Therefore, the absorber length should be selected carefully satisfying both high absorption and optimum dark current. **Figure 4.1** shows that for an HgCdTe detector with 5 µm cut-off wavelength, 3 µm long absorber layer is sufficient to absorb ~93% of incident light at 100 K and this value increases to ~98% for an absorber length of 5 µm. In the designed device structures, absorber layer is chosen to be 3 µm long since it allows significant rate of absorption.

Length and Cd mole fraction of the cap layer are other design parameters. This layer creates the pn junction and forms the electrical characteristics together with the

absorber layer. Typically, length of this layer is shorter than the absorber layer in order to avoid recombination of photo-generated carriers. Therefore, 1 µm layer is utilized as the cap layers of both DLH and DEH structures. On the other hand, Cd composition of this layer is another parameter, which determines the electrical characteristics of the detector structure. Conventional DLH structures contain slightly higher Cd composition in cap layer with respect to the absorber layer so that the elevated bandgap minimizes the thermal generation in this layer. In other words, diffusion and generation-recombination dark currents are expected to be originated mostly in the absorber layer. In addition to this, the energy band potentials should be examined between consecutive epitaxial layers where discontinuities in energy bands may result in substantial performance degradation. For conventional DLH structures, utilization of abrupt composition change inevitably generates offset in both valence and conduction bands. However, this effect can be tolerated with the band bending formed by the internal electric field. Even though doping densities are influential in this process, J. Wenus et al. [91] stated that higher composition of cap layer does not significantly affect the quantum efficiency and dark current performance of the detectors. As a result, $x = 0.5$ mole fraction is selected for the cap layer of DLH structure as shown in **Figure 4.2**.

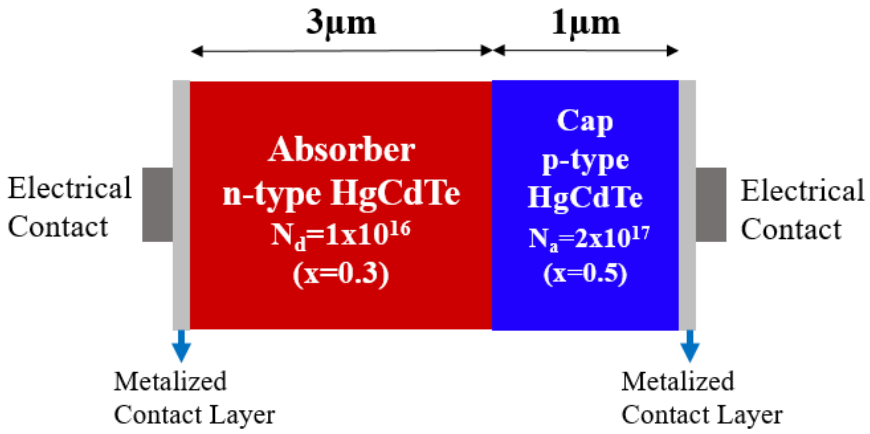

Figure 4.2: DLH detector layer structure for MWIR window.

Furthermore, the doping densities form junction behavior and influence fundamental electrical events such as band bending, depletion region length, tunneling probabilities and recombination processes. Dark current level of diode seems to be inversely proportional with donor and acceptor levels as stated in Equation 1.8. However, the

recombination lifetime also changes with the doping density. Therefore, increasing the doping density may not be a solution to the dark current performance of the detector. Specifically, if the detector performance is limited by the short SRH recombination lifetime. When the doping densities forming the junction is excessively high, the internal electrical field significantly increases within the relatively small depletion region. Therefore, the amount of bending in energy bands increases and occurs in a shorter distance. As a result, the valence band of p-type layer approaches to the conduction band of n-type region and increases the tunneling probability. This process limits the doping densities in order not to trigger tunneling dark currents, which may dominate dark current even for low reverse bias voltages.

Another constraint is related with the collection of photocurrent. Highly doped detector may be easily affected by Auger recombination with even more significant rates for the optical illumination case. Hence, the signal level is more sensitive to the Auger recombination.

A conventional n-type doping density is in the interval of $0.2 \times 10^{15}\ cm^{-3} - 1 \times 10^{16}\ cm^{-3}$ [58, 74, 75], where the ideal doping level changes with the carrier lifetimes and the operation conditions. For the designed devices, the donor doping level is selected to be $N_D = 1 \times 10^{16}\ cm^{-3}$. For an absorber layer doping, the cap layer doping can be selected to design depletion region properties. As mentioned earlier, depending on the imperfect annealing processes, Hg vacancies may be present at p-type HgCdTe layers. These vacancies may create sensitivity to the recombination mechanisms since the trap energy levels stimulate these mechanisms in depletion region. Therefore, the major part of the depletion region is desired to be located in n-type region. As a result, the cap layer doping is selected as $N_A = 2 \times 10^{17}\ cm^{-3}$ which is 20 times higher than the absorber layer doping and similar to the typical doping density values in literature [58, 74, 75].

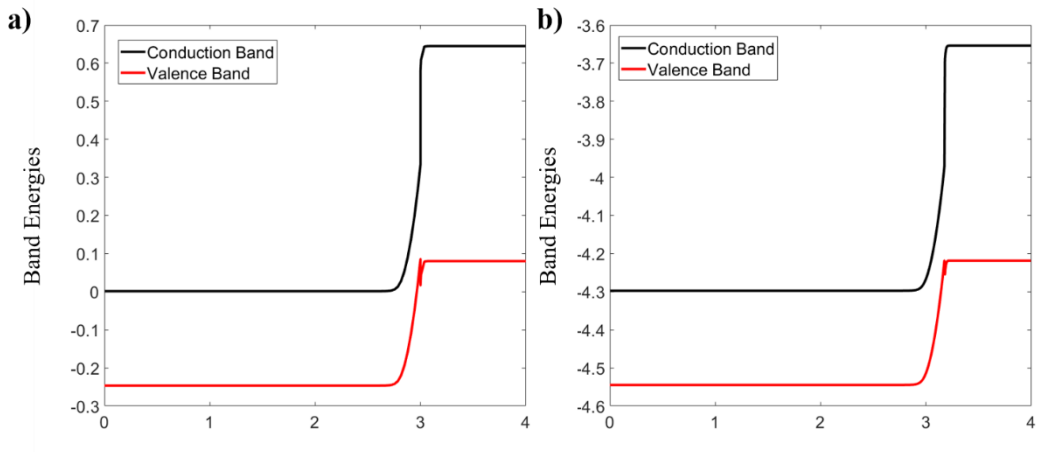

Figure 4.3: Band diagrams for DLH structure obtained from **a)** Sentaurus Device and **b)** the in-house numerical tool for V_{bias}=-0.1V.

The band diagram of the DLH device is represented in **Figure 4.3** with both using the commercial software Sentaurus Device and the in-house simulation tool. There is almost a perfect agreement in the results except for small differences, which are originated from mesh size difference. As shown in the band diagram, the composition change introduced an offset in valence band. However, this offset does not create a discontinuity in the valence band since it is placed at the pn junction interface.

4.2. Dark Current Suppression Technique

The aim of the designed structure is to enhance performance of alternative substrate mid-wave HgCdTe detectors. For this purpose, the suppression method is utilized targeting the recombination mechanisms originating in depletion region such as TAT, SRH, Auger and radiative recombinationss. All of these mechanisms are directly influenced by the intrinsic carrier density and the carrier lifetime as previously mentioned. Moreover, these processes are more significant for alternative substrates due to the inadequate crystal quality of sensor layers. For this reason, a considerable amount of research focuses on improving the crystal quality of these devices but reported carrier lifetimes are still very short (50 ns – 3 µs) for alternative substrates [118, 119]. On the other hand, variations in the temperature and Cd mole fraction considerably changes the intrinsic carrier concentration and accordingly the recombination rates. 50 K decrease (from 100 K to 150 K) in the operation temperature

yields 153 times drop in the intrinsic carrier density ($n_i = 8.01 \times 10^{10}\ cm^{-3} \rightarrow n_i = 1.23 \times 10^{13}\ cm^{-3}$) for $x = 0.3$. However, elevation in operating temperature is desired in order to lower the cooling cost and to produce area efficient camera systems.

Another point is that similar effect can be achieved by the placement of a higher Cd composition material in the corresponding region. For instance, n_i decreases rapidly ($n_i = 8.06 \times 10^{10}\ cm^{-3} \rightarrow n_i = 1.23 \times 10^{8}\ cm^{-3}$) even for 0.07 ($x = 0.3 \rightarrow x = 0.37$) change in the Cd mole fraction at 100 K. Considering the depletion region approximation and the quadratic relation of TAT, SRH, Auger and radiative recombinations with intrinsic carrier density, the suppression of these dark current mechanisms are more dramatic. Therefore, the depletion engineered heterojunction (DEH) MWIR detector structure designed in this thesis based on this approach. However, generation of valence band discontinuity should be avoided at the interface of absorber and suppressive wide bandgap layer. In the following section, the determination of length and Cd composition of the wide bandgap layer (depletion layer-DL) is presented.

4.3. Valence Band Discontinuity Cancelation

As mentioned in previous sections, QE is a key performance parameter for infrared detectors, where the successful collection of photo-generated carriers from the electrical contacts has a significant effect on this parameter besides the absorption of incoming radiation. Hence, the DEH structure should be designed so that the photo-generated carriers are not disturbed by band discontinuities. In this study, a method is proposed in order to remove carrier-blocking discontinuity in valence band.

Electron affinity, band energy differences between sensor layers and the junction parameters determine the final state of the band diagram. Therefore, determination of mole fraction in suppressive depletion layer and its length should be mathematically modelled as a function of these parameters. As modelled in Chapter 3, valence band energy is a combination of intrinsic parameters and the electrical potential inside the device. Considering only intrinsic parameters, electron affinity decreases due to the mole fraction increase in the depletion layer with respect to the absorber layer. On the other hand, increase in the bandgap energy is more significant resulting in a higher

valence band discontinuity. Material properties given in previous sections are utilized to estimate valence band offset that is illustrated in the **Figure 4.4**.

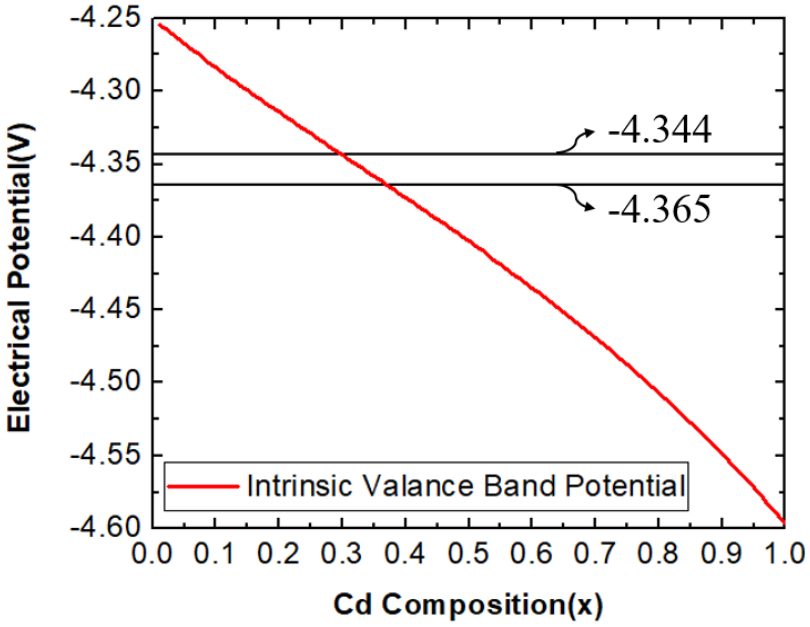

Figure 4.4: Change in the intrinsic valence band potential with respect to the Cd composition, where the insets correspond to $x = 0.3$ and $x = 0.37$ Cd compositions, which is obtained from the in-house numerical tool.

The potential energy given in this figure is a combination of electron affinity and the bandgap energy difference in valence band. In other words, the potentials belonging to the Cd mole fractions of the two consecutive layers demonstrate the band offset without the junction effect. From this graph, the discontinuity value introduced to the system can be evaluated precisely for a selected Cd composition in depletion layer. It is obvious that for a higher Cd composition, the suppression rate increases. However, a higher valence band offset is introduced to the detector structure. For a desired suppression rate Cd composition should be selected as a first design parameter. After selecting the depletion layer mole fraction regarding the suppression level, the amount of discontinuity for the selected layer should be noted so that it can be eliminated by band bending.

The band discontinuity is assumed to be eliminated, when the sharp edge at DL and AL interface equals to the energy level of the absorber layer in the valence band. Due

to the band bending, the potential barrier gets thinner, which increases the tunneling probability of carriers and minimizes the barrier effect.

As a second step, the length of the depletion layer should be determined without generating a valence band discontinuity. Ideally, suppressive depletion layer length should be as wide as possible for the complete coverage of depletion region leading to a fully suppressed SRH recombination. The valence band offset introduced between the depletion layer and absorber layer should be located inside the depletion region so that the proposed valence band discontinuity cancelation method can be utilized. In order to determine the maximum utilizable depletion layer length, the energy band potential should be solely investigated. **Figure 4.5** represents the electrical potential inside the DLH detector structure.

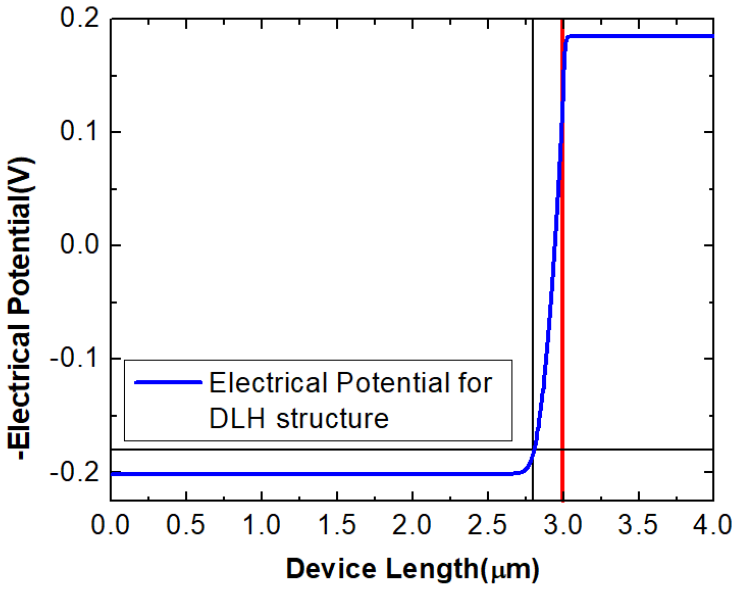

Figure 4.5: Electrical potential change inside the DLH device due to pn junction, which is obtained from the in-house numerical tool. The red line represents pn junction interface and the solid black lines correspond to the point that provides introduced band offset for the Cd composition of depletion layer.

The proposed design approach requires that the electrical potential variation with respect to the absorber layer should be at least the amount of valence band offset corresponding to the selected Cd composition level of the suppressive layer, which is determined by using **Figure 4.4**. For instance, the composition change introduces ~0.02 eV band offset for $x = 0.37$ depletion layer composition. For the maximum

coverage of depletion region, the suppressive layer should start at the point having a potential that is sum of the band offset (~0.02 eV in this case) and the negative of valence band potential of absorber layer (-0.02 eV). Note that this layer is n-type doped and it is confined in between the estimated point and the pn junction interface. As explained before, a larger bandgap material in the depletion region increases the suppression rate. However, it requires shorter DL length, which may suffer from the unsuppressed recombination in the edges of depletion region. Hence, there is a trade-off between coverage of the depletion region and the suppression rate so there are optimum depletion layer parameters (Cd composition & length) for each detector structure. For the optimum performance, Cd composition of depletion layer can be renewed and this procedure should be repeated in order to find ideal layer parameters.

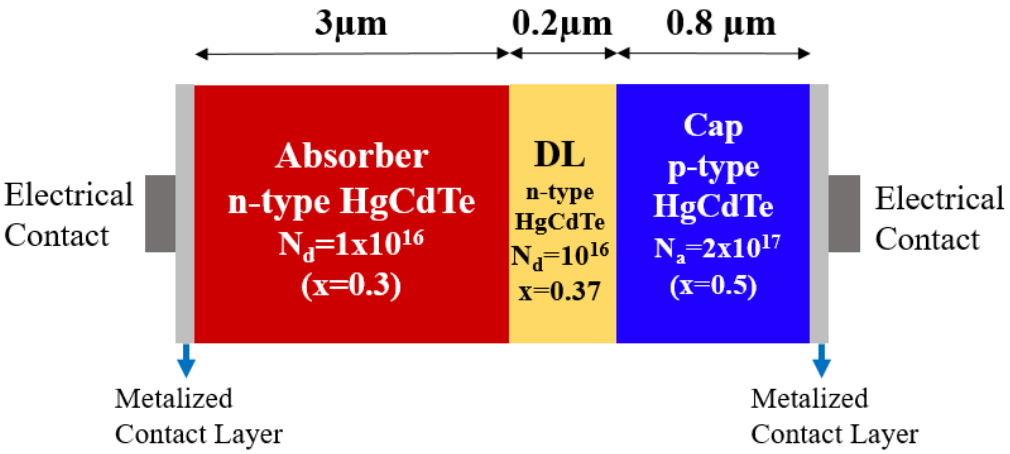

Figure 4.6: The layer structure for the DEH MWIR detector, where the depletion layer (DL) is represented in yellow region.

For the DEH structure, Cd mole fraction is determined as $x = 0.37$ and the maximum utilizable depletion layer length is found as 0.2 µm using the valence band discontinuity cancelation method. The resultant layer structure of this detector is illustrated in **Figure 4.6**.

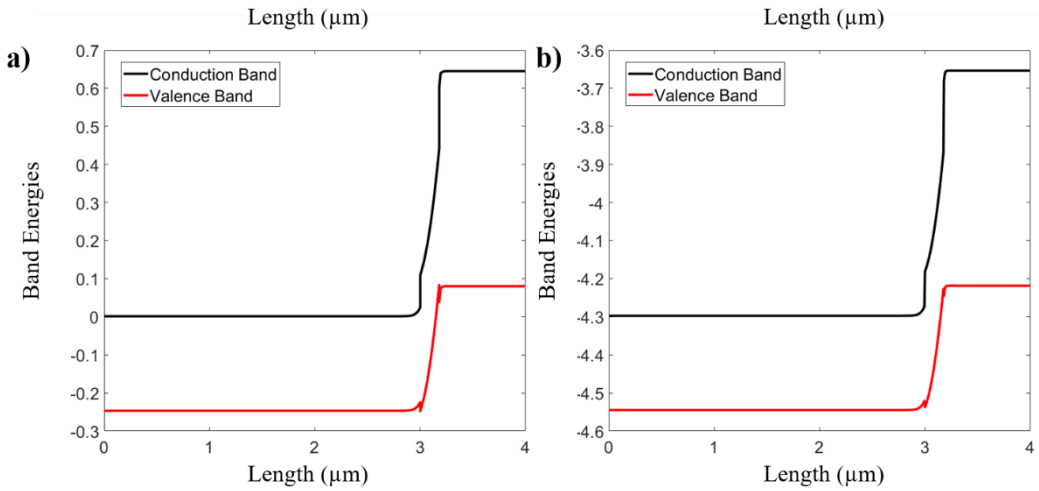

Figure 4.7: Band diagrams for DEH structure obtained from **a)** Sentaurus Device and **b)** the in-house numerical tool for V_{bias}=-0.1V.

Figure 4.7 represents the band diagram for DEH structure taken from both Sentaurus Device and the in-house numerical tool. As shown in the band diagrams, both results are in a good agreement, where small differences can be explained with the number of evaluation points used in the simulations. In the band diagram of DEH device, there is no valence band discontinuity, which might affect the detector performance. Detailed analysis of this structure is represented in the following section in terms of both dark current and quantum efficiency, where the effect of valence band discontinuity is also illustrated in sensitivity analysis section for variations in the design parameters.

4.4. Performance Analysis

TAT, SRH, Auger and radiative recombinations are included to the simulations for both DEH and DLH detectors and these detectors are compared with each other in terms of dark current and quantum efficiency values. The analysis is carried out for the temperatures between 75 K and 250 K under illumination and dark environment. As stated in the device parameters section, atmospheric transmission is assumed as 80% between 3-5 µm and f-number is two. Exitance of a room temperature object having 1 m^2 surface area is evaluated as $3 \times 10^{-5}\ W/cm^2$, after passing through the optic system, where both sensors are exposed to this radiation in 4 µm wavelength in the simulations.

In order to observe improvements and to reveal dominant dark current mechanisms for these structures, various cases have been simulated considering Auger, SRH, TAT and radiative recombinations as well as the diffusion only case. This procedure also enabled us to compare these values with the maximum achievable device performance, which is the diffusion-limited case. Furthermore, SRH lifetimes are reduced to 200 ns and 1 μs in order to represent poor electrical properties of alternative substrates.

For the DEH device, carefully placed wide bandgap material ($x = 0.37$ in this case) into the depletion region is expected to reduce the contribution of TAT, SRH, radiative and Auger recombinations to the dark current. It should be noted that the stated values of intrinsic carriers ($n_i = 8.06 \times 10^{10}\ cm^{-3} \rightarrow n_i = 1.23 \times 10^{8}\ cm^{-3}\ for\ x = 0.3 \rightarrow x = 0.37$ at 100 K) are local parameters and only valid in the suppressive layer. In other words, the overall suppression may not be in the same degree due to the recombination take place in the other layers. Nevertheless, these processes are several orders of magnitudes lower outside the depletion region, which yields that almost complete suppression can be accomplished by this technique.

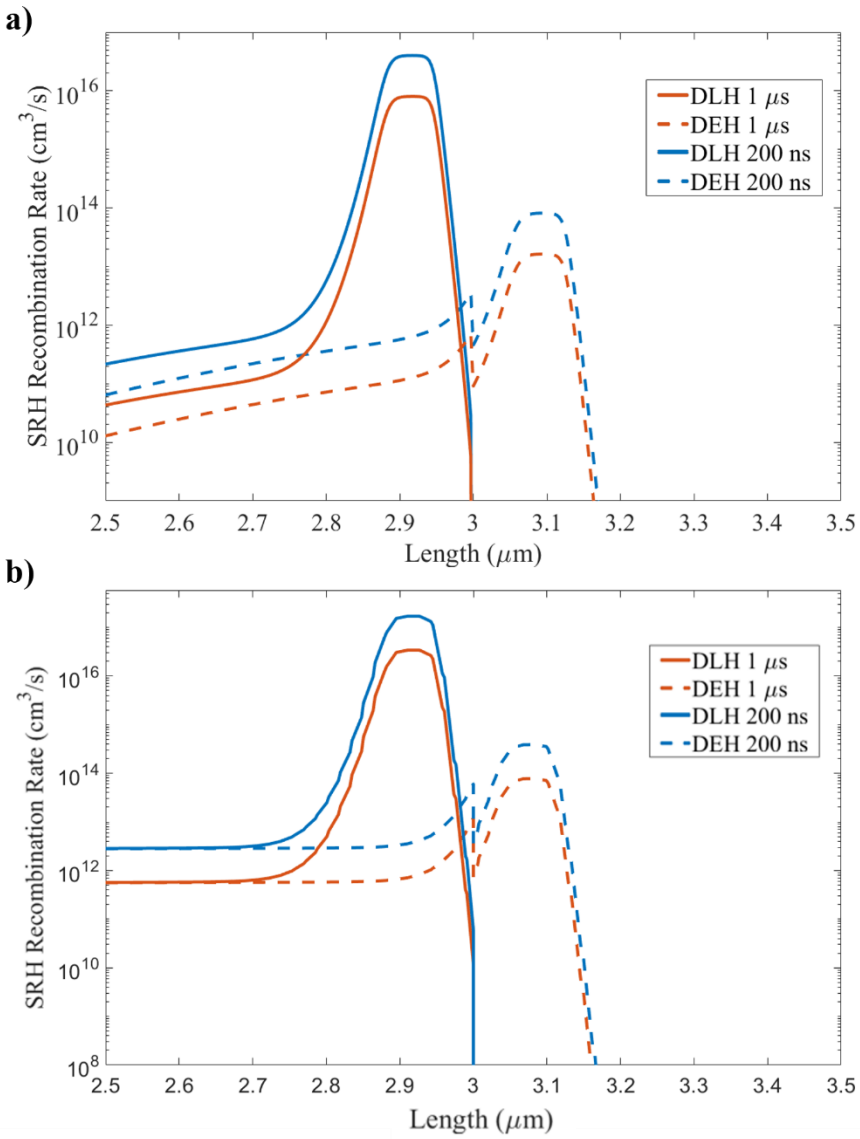

Figure 4.8: SRH recombination rate for $\boldsymbol{\tau = 1\ \mu s}$ and $\boldsymbol{\tau = 200\ ns}$ cases for both DLH and DEH structures obtained from **a)** the in-house numerical tool and **b)** Sentaurus Device.

Figure 4.8 represents the SRH recombination rates for the mid-wave DLH and DEH detectors, where the SRH recombination rates obtained from both simulation tools are in good agreement. This figure illustrates the suppression of SRH recombination mechanism. As expected, the degradation in this parameter gets more significant as the mole fraction increases ($x = 0.3 \rightarrow 0.37$, $R_{SRH} = 4.1 \times 10^{16}\ \frac{cm^3}{s} \rightarrow 8.2 \times 10^{13}\ \frac{cm^3}{s}$). However, the overall effect of the suppression to the dark current performance stays constant at the same level after a certain Cd composition. Moreover, valence band discontinuity at the interface of depletion layer and the absorber layer

becomes more and more apparent as the bandgap of suppressive layer increases. The outcomes of this event to the detector performance is investigated thoroughly in the sensitivity analysis section.

Figure 4.9 illustrates the Arrhenius plot of the dark and photo current levels for diffusion only case as well as current densities of DEH and DLH devices when the SRH recombination lifetime is 200 ns. The enhancements in the operation temperature is evaluated for 99.9% BLIP condition for both structures in order to maintain high signal to noise ratio as the target application of the DEH detector structure is high performance detection. In this sense, ~40 K (from ~83.5 K to ~123.5 K) of increase in the operation temperature is observed for the optimized DEH structure.

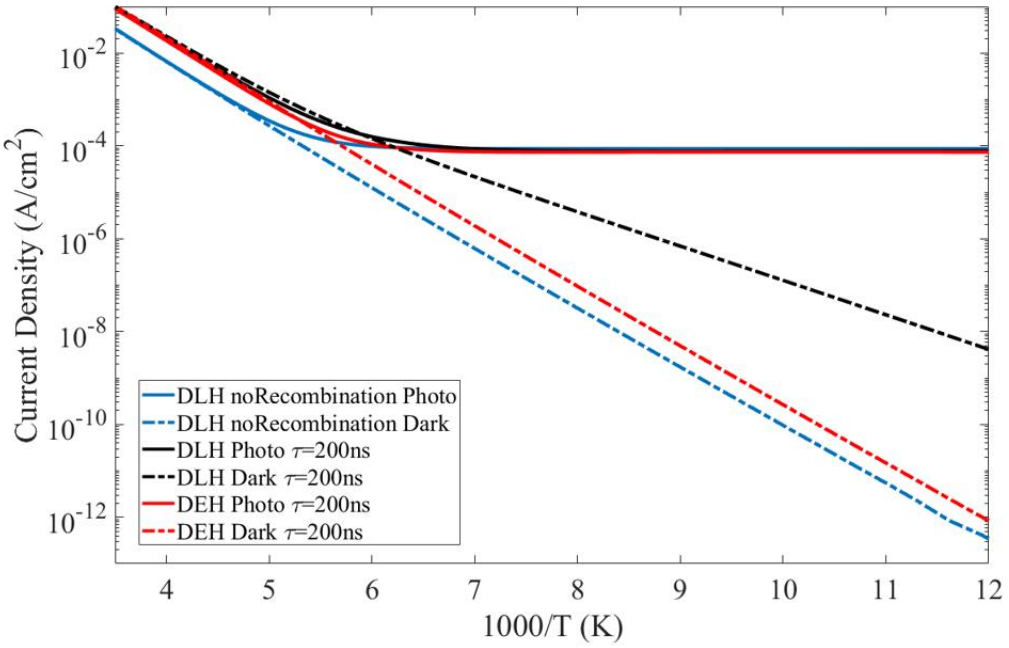

Figure 4.9: Arrhenius plot of current density obtained from Sentaurus Device software for V_{bias}=-0.1 V and τ=200 ns.

Alternatively, at the same operation temperature (T=100 K), the dark current density is reduced approximately ~2000 times for DEH detector structure compared to DLH detector shown in **Figure 4.6** (from $J_{dark} = 1.25x10^{-7}A/cm^{-2}$ to $J_{dark} = 2.57x10^{-10}A/cm^{-2}$). With this enhancement, performance of alternative substrate sensors may substantially increase benefiting from low dark current or advanced operating temperatures.

The same simulation is repeated for 1 μs of carrier lifetime and the results are represented in **Figure 4.10**. In this case, the improvement in the operation temperature is ~35 K (from ~92.5 K to ~127.5 K) without any degradation in the performance. Moreover, the dark current density value has become $J_{dark} = 2.13x10^{-7} A/cm^{-2}$ at 100 K, which corresponds to ~850 times decrease. The results showed that the advancement in the device performance is more apparent for $\tau = 200\, ns$ case even when the dark current is lower for $\tau = 1\, \mu s$ case. The very short carrier lifetime magnifies the recombination rates -specifically the SRH recombination- generating immoderate dark current. For this reason, the enhancement achieved with the suppression becomes more significant for lower crystal quality.

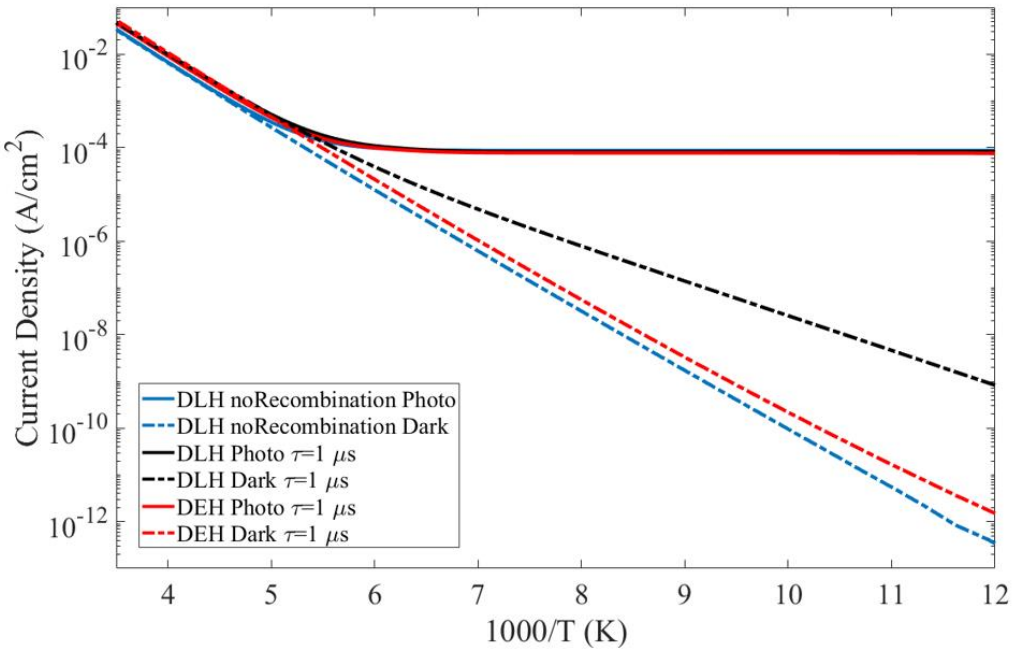

Figure 4.10: Arrhenius plot of current density obtained from Sentaurus Device software for V_{bias}=-0.1 V and τ=1 μs.

Another point is that the quantum efficiency values are kept high during this process. For the both cases, QE values are around 80% (77% for 200 ns, 82% for 1 μs) which is nearly equal to the diffusion only case (QE = ~87%). The data proves that the valence band discontinuity is removed and collection of photo-generated carriers is not disturbed.

One important point is that the mobility values may be negatively affected depending on the substrate type. In order to investigate variations in mobility values, the values

found in literature are compared with the implemented numerical tool. For instance, the electron mobility for GaAs substrates is provided as $4.8x10^4 cm^2V^{-1}s^{-1}$ for 0.3 Cd composition at 77K [120] and the value that we use is $4.74x10^4 cm^2V^{-1}s^{-1}$ in our model at the same conditions. Moreover, in a recent publication [121], hole mobility values are measured between $434\ cm^2V^{-1}s^{-1}$ and $588\ cm^2V^{-1}s^{-1}$, which are again similar to the values used in the simulations. M. Carmody et al. [122] provided mobility measurements which verify that GaAs substrates may generate the similar mobility values compared to the CZT substrates. On the other hand, the results show that Si substrates with higher lattice match may experience more severe negative effect on mobility. Considering the majority of the samples [122], decrease on the mobility for Si substrates is estimated as 15%. Therefore, in order to represent the effect of variation in the mobility for alternative substrate devices to the overall detector performance, both electron and hole mobilities are decreased to the 85% of their ideal values and the simulations are repeated with the renewed parameters. The resultant simulations showed that the decrease in QE is nearly 1.5% (from ~82% to ~80.5%) and 5% (from ~80% to ~75%) for 1 μs and 200 ns, respectively. On the other hand, dark current values are also decreased by ~8% for 1 μs (~15% for 200 ns) resulting in even higher signal to noise ratio. This result can be explained by the mobility component of the current equations.

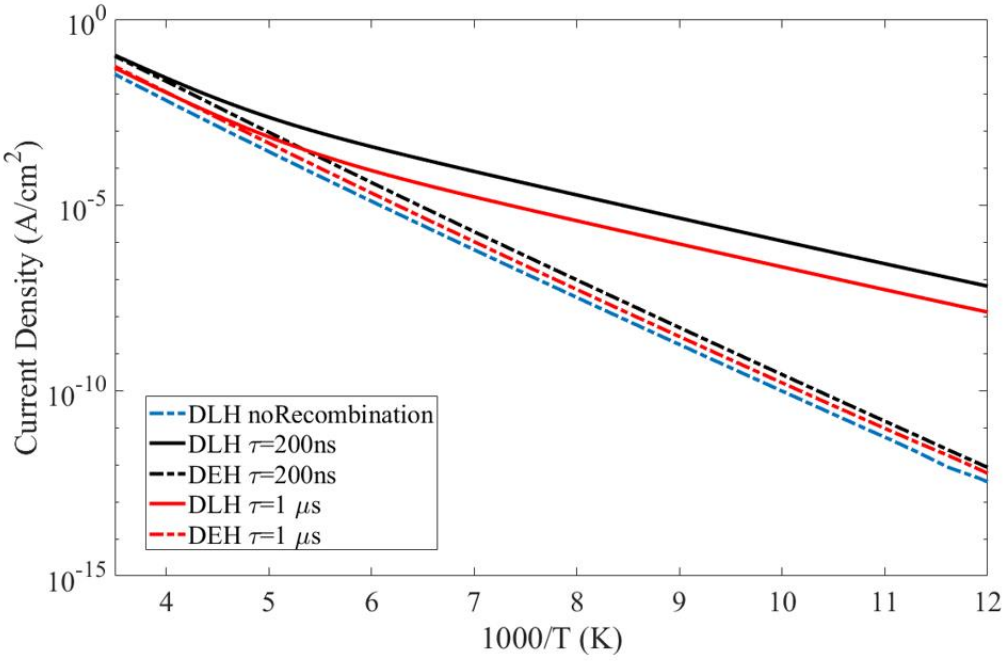

Figure 4.11: Arrhenius plot of dark current densities obtained from Sentaurus Device software for both devices and lifetimes at V_{bias}=-0.1 V.

In **Figure 4.11**, the dark current of the given structures (DLH and DEH) for both lifetime values are compared with the diffusion-only case. For the complete suppression case, the recombination rates are negligible and the dark current is composed of only diffusion current. Therefore, it can be considered to be the minimum achievable dark current. As seen in the **Figure 4.11**, the dark current of DEH structure is only ~2-3 times higher than the diffusion current even for low carrier lifetimes. The dark current level for 1 μs lifetime is almost equal to the diffusion-limited case, where it is slightly higher for $\tau = 200\ ns$. The difference comes from the recombination rate, which occurs outside of the depletion region. After the suppression of recombination mechanisms in depletion region, the recombination rate in the remaining part is typically very small compared to diffusion current. However, as the carrier lifetime becomes shorter, the recombination rate in this region increases and starts to dominate dark current. Hence, the dark current for $\tau = 200\ ns$ is ~2.7 times higher than the diffusion current.

4.5. Sensitivity Analysis of DEH Detector Structure

Simulations and analytical calculations help designers to optimize detector structures and find ideal values for design parameters. However, in practice, variations usually take place in these parameters, which may generate undesired consequences in the detection performance. Therefore, it is essential to investigate sensitivity of the DEH structure to the design parameters in case of the fabrication related aberrations.

Firstly, the depletion layer mole fraction is subjected to variations and DEH detector structure is simulated many times for different Cd composition cases. The resultant band diagrams are illustrated in **Figure 4.12**, where the suppressive depletion layer mole fraction is utilized between $x = 0.32$ and $x = 0.55$.

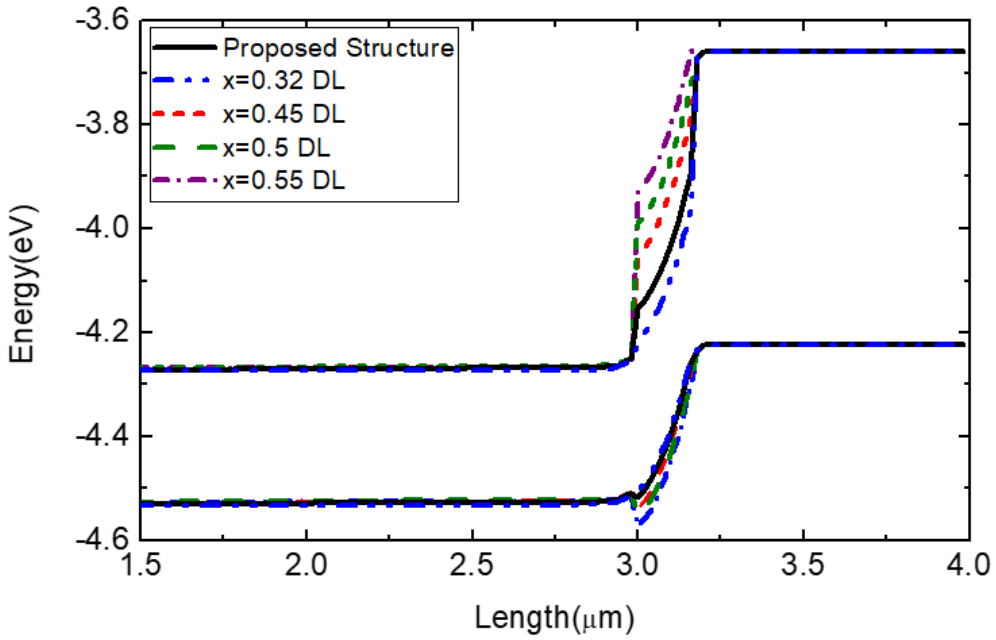

Figure 4.12: Band diagram for various devices with different Cd composition in depletion layer obtained from the in-house numerical tool.

Results show that conduction band energy changes more significantly than the valence band where the discontinuity reaches considerable levels for Cd compositions higher than $x = 0.5$. To be more accurate, dark current and the quantum efficiency are noted for more realistic cases. DLH, optimized DEH structures and the detectors with DL composition of $x = 0.34$ and $x = 0.4$ are compared in the following table.

Table 4.1: Performance comparison for conventional DLH, optimized DEH and DEH structures having Cd composition variations in DL.

Doping Density	Cd Composition	Depletion Layer Length	Dark Current Density	QE
Double Layer Heterojunction Structure (Figure 4.2)			$2.08x10^{-7}A/cm^{-2}$	88.1%
$N_d = 1x10^{16}cm^{-3}$	x=0.37	0.18 μm	$1.56x10^{-10}A/cm^{-2}$	82%
$N_d = 1x10^{16}cm^{-3}$	x=0.34	0.18 μm	$1.5x10^{-9}A/cm^{-2}$	82.8%
$N_d = 1x10^{16}cm^{-3}$	x=0.40	0.18 μm	$1.07x10^{-10}A/cm^{-2}$	77%

As expected, the wide bandgap material decreased QE but this change is limited only by ~5%, which does not critically influence the detection performance. On the other hand, dark current is increased nearly 10 times (from $I_{dark} = 1.56x10^{-10}A/cm^{-2}$ to $I_{dark} = 1.5x10^{-9}A/cm^{-2}$) for $x = 0.34$ case since the suppression rate is inadequate due to the lower Cd composition .

Secondly, fluctuations in the depletion layer length have been investigated for $l = 0.1\ \mu m, 0.24\ \mu m, 0.3\ \mu m$ and $l = 0.4\ \mu m$. Band diagrams for these cases are represented in **Figure 4.13,** where longer DL cases suffer from valence band discontinuity.

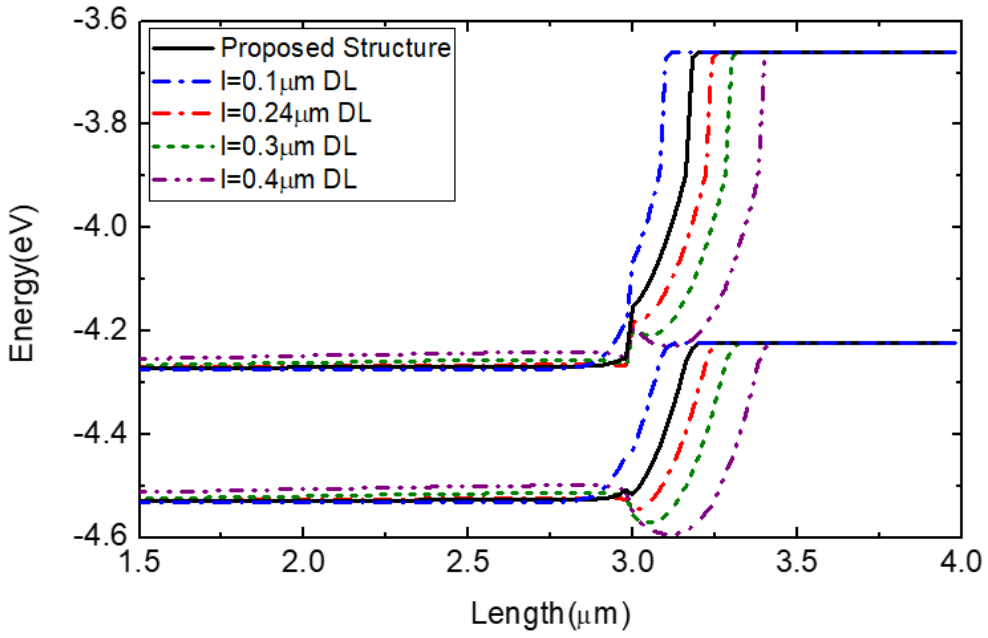

Figure 4.13: Band diagram with respect to the change in the depletion layer length obtained from the in-house numerical tool.

At the DL and AL interface, an additional band bending occurs for excessively long depletion layer cases. For these cases, the interface is positioned outside of the depletion region, which generates a junction between two n-type layers. Note that these two layers are identically doped. However, the intrinsic fermi potential is different in these layers since the change in the bandgap potential is not shared in the same amount between conduction and valence bands. Moreover, the donor doping energy levels are also different for these layers due to their intrinsic carrier densities. For these reasons, a negative electric field is generated at the AL/DL interface when it is not depleted. The resultant negative electric field disturbs the current flow inside the detector and introduces a hole blocking energy barrier, which is similar to band discontinuity. As in the previous analysis, the performance is estimated for more realistic variations in the depletion layer length. In the following table, dark current and QE values are represented for $\pm 0.06\ \mu m$ change in DL length.

Table 4.2: Performance comparison for conventional DLH, optimized DEH and DEH structures having variations in DL length.

Doping Density	Cd Composition	Depletion Layer Length	Dark Current Density	QE
Double Layer Heterojunction Structure (Figure 4.2)			$2.08x10^{-7}A/cm^{-2}$	88.1%
$N_d = 1x10^{16}cm^{-3}$	x=0.37	0.18 μm	$1.56x10^{-10}A/cm^{-2}$	82%
$N_d = 1x10^{16}cm^{-3}$	x=0.37	0.24 μm	$1.54x10^{-9}A/cm^{-2}$	76.9%
$N_d = 1x10^{16}cm^{-3}$	x=0.37	0.12 μm	$1.19x10^{-9}A/cm^{-2}$	83.6%

As shown in **Table 4.2**, when DL length is smaller than the optimized value ($l = 0.12\ \mu m$), the dark current suppression level is ~8 times lower than the ideal case. This behavior comes from the lack of coverage of depletion region. On the other hand, QE is decreased by ~5.1% (from 82% to 76.9%) for $l = 0.24\ \mu m$ case due to the hole barrier in valence band. Furthermore, the newly generated negative electric field results in SRH recombination in the absorber layer side, hence, the dark current is increases to $I_{dark} = 1.54x10^{-9}A/cm^{-2}$ (from $I_{dark} = 1.56x10^{-10}A/cm^{-2}$). Nevertheless, even with these changes, the detector structure is still functional and provides better signal to noise ratio than conventional DLH structure.

Furthermore, the variations in the doping densities are also investigated in order to reveal the sensitivity of detector performance to this parameter. The suppression technique focusses on the recombinations in depletion region and the doping densities determine the properties of this layer. Therefore, fluctuations in the doping density are expected to affect the performance by the change in depletion region length. In the **Figure 4.14**, doping densities of the absorber and the depletion layer is arranged to observe effect of ± 2 and ± 10 times variations in this parameter.

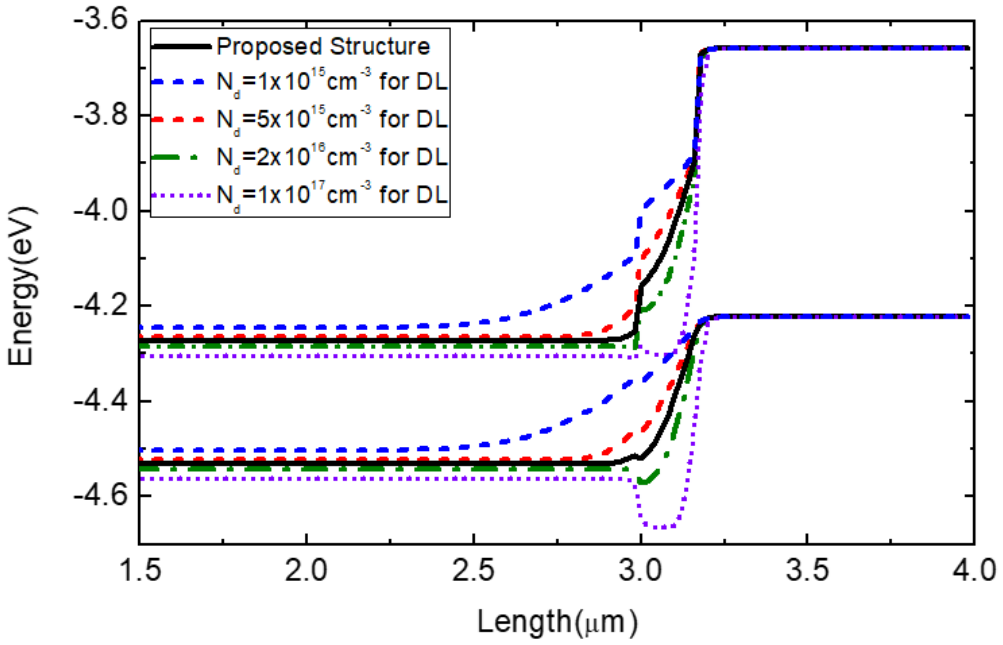

Figure 4.14: Band diagram with respect to fluctuations in doping density of depletion layer obtained from the in-house numerical tool.

Similar to the excessively long DL case, when the doping is increased by 10 times, the depletion region in n-type region gets smaller and results in n-N junction. As explained above, the negative E-field creates band bending, which increases valence band discontinuity even more and disturbs the detector performance. On the other hand, when the doping level is reduced, the depletion region extends toward the absorber layer and DL covers only a portion of this region. However, although the suppression becomes less significant, this device is still functional as an infrared sensor.

Table 4.3: Performance comparison for conventional DLH, DEH with designed parameters and DEH structures having variations in DL doping density.

Doping Density	Cd Composition	Depletion Layer Length	Dark Current Density	QE
Double Layer Heterojunction Structure (Figure 4.2)			$2.08x10^{-7}A/cm^{-2}$	88.1%
$N_d = 1x10^{16}cm^{-3}$	x=0.37	0.18 μm	$1.56x10^{-10}A/cm^{-2}$	82%
$N_d = 5x10^{15}cm^{-3}$	x=0.37	0.18 μm	$2.11x10^{-9}A/cm^{-2}$	87%
$N_d = 2x10^{16}cm^{-3}$	x=0.37	0.18 μm	$9.44x10^{-10}A/cm^{-2}$	59.9%

For the two times variation in the doping density, data shown in the **Table 4.3** is obtained. When the doping level is $N_d = 5\text{x}10^{15} cm^{-3}$, the dark current is elevated by more than ten times as expected. In addition, QE is increased to 87%, which is slightly more than the designed DEH device. The only significant performance degradation has come from the high doping case, where the QE is limited by 59.9%. In conclusion, the utilized suppression method is able to withstand the changes in the design parameters without having a critical deterioration in photocurrent collection. Results showed that the maximum decrease in QE is limited by ~5% except the high doping case. Moreover, even with the fluctuations originating from the fabrication, the dark current values are still ~2-3 orders of magnitude lower than the conventional DLH device.

4.6. Conclusion

A significant improvement has been reported in this thesis on the dark current performance of alternative substrate HgCdTe detectors. By effectively minimizing the SRH dark current for alternative substrate mid-wave detectors, an increase in the operation temperature is achieved. Alternatively, the signal to noise ratio is significantly improved at the same operation temperature. One important point is that lattice-mismatch may result in degradations in the detector performance due to the dislocations [123]. Similar to the lattice mismatched InGaAs and superlattice detectors, alternative substrate HgCdTe devices may suffer from shunt current generated by the dislocations. Furthermore, an activation energy of Eg/2 has been reported in literature [124, 125] for shunt leakage due to the dislocations, which may lead to a significant increase in the dark current. The density of dislocations depends on micro processing steps and the growth conditions, where density, electrical properties and the interactions between dislocations determine the shunt leakage current. Moreover, previously reported studies [123, 126-128] reported a relation between 1/f noise and the dislocations, where shunt leakage noise coefficient might be larger than the G-R noise coefficient resulting in an important limitation for these detectors [129, 130]. However, due to the lack of a well-established theory on dislocation modeling, shunt leakage is not included in this thesis.

Considering TAT, SRH, radiative and Auger recombinations, the improvement in the dark current density has been achieved by generation-recombination suppression method. While additional TAT dark current is observed in DLH device at relatively low temperatures, a wide bandgap depletion layer significantly eliminated this contribution and lowered the dark current density. The quantum efficiencies are maintained high for DEH device structure with significantly lower dark current values. This improvement is observed to be more significant for shorter carrier lifetimes and lower operating temperatures. It should be noted that the shunt leakage mechanism might be more apparent for these conditions. Nevertheless, the performance of the DEH detector structure is significantly higher than the DLH detector structure. With our assumptions, the dark current density is very close to diffusion-limited case for a wide range of operation temperature. Therefore, the dark current density of this structure is less affected by the crystal quality than the DLH detector structure with the specified assumptions.

Sensitivity of DEH device to the fabrication errors is also investigated in order to represent practical concerns. For reasonable variations on the depletion layer parameters, the dark current and quantum efficiency performances of the DEH structure do not critically affected. Only for a high doping case, QE is decreased by ~20%, where the dark current is still very low compared to DLH detector. For all other cases, variations in the performance parameters are very small for the illustrated DEH structure, which demonstrates the effectiveness of the suppression technique.

CHAPTER 5

SWIR DETECTOR DESIGN FOR NIGHTGLOW DETECTION

SWIR detection has been in great interest for both civilian and military applications. Unlike MWIR and LWIR windows, detection in short wavelength region improves the capabilities of human eye and even provides remarkable features. Detection in very dark environments is one of these applications. Specifically, ability to detect objects in moonless night has been the ultimate target for high performance detector designers.

5.1. Nightglow Radiation

The major light source in short-wave infrared region is sun, where the reflected sunlight is aimed to be detected in majority of the SWIR applications. Alternatively, an active light source can be utilized to improve the detection capabilities in this region especially in indoor applications. However, utilization of an active source may not be desired for the military applications like night vision since these sources can be easily detected from the outside. Nevertheless, the infrared imaging technology can still provide functionality in SWIR band by the help of nightglow radiation. This energy pattern is defined as the emitted light from the atmospheric gasses during the night. The molecules exposed to the daylight releases their energy and forms an invisible light source. Since the intensity of this radiation is very low compared to other sources, design of novel sensor structures and advancements in semiconductor technology have been essential part of nightglow detection.

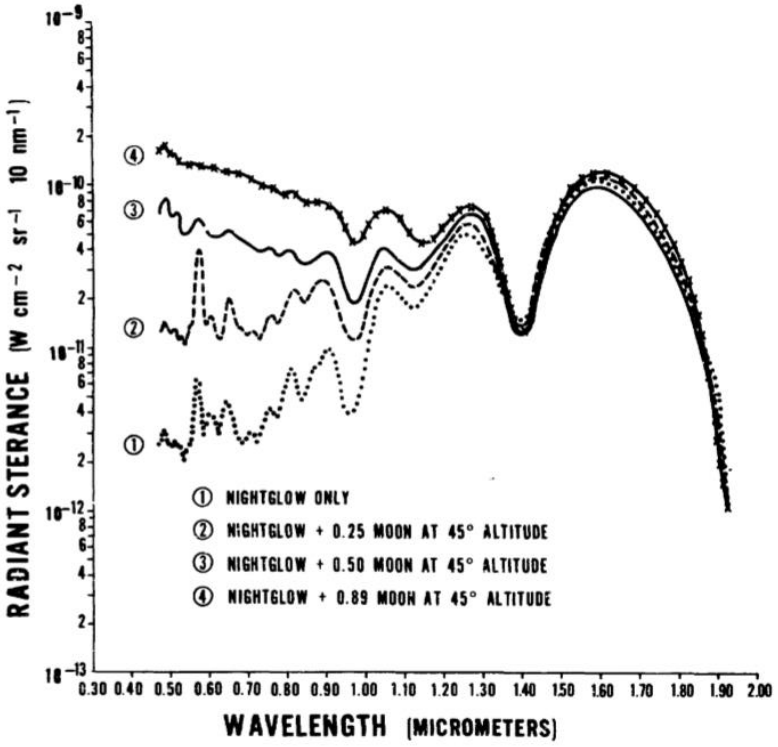

Figure 5.1: Radiant sterance spectrum for nightglow under four different conditions [131].

Another important point is that the nightglow radiation is present below 1.9 μm wavelength in the infrared spectrum as shown in **Figure 5.1**. The total amount of energy emitted from this source [131] is evaluated as low as $L_{nightglow} = \sim 3.42\, nW/cm^2.sr$. Moreover, the flux calculations are repeated for another measurement [132] in the literature. The irradiance graph of the nightglow radiation is presented in **Figure 5.2**.

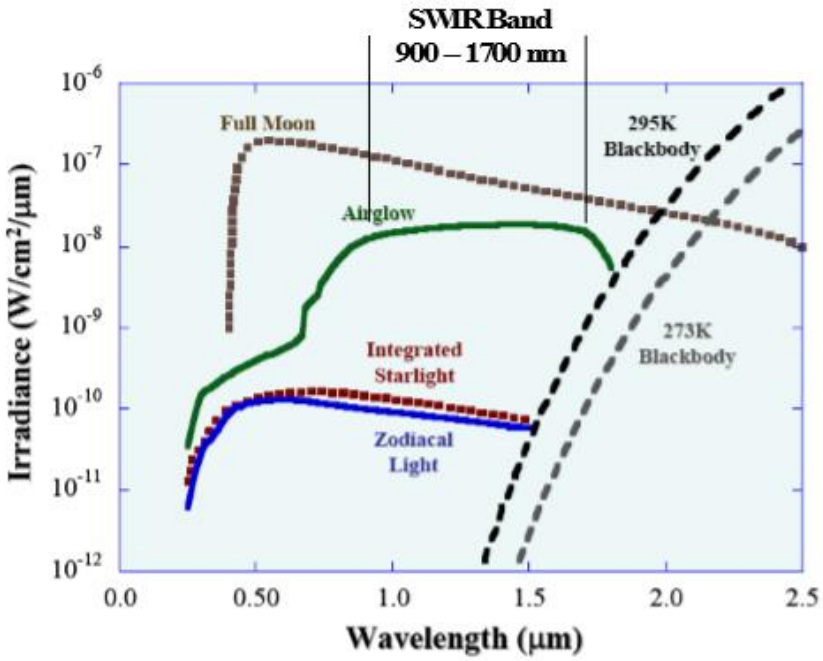

Figure 5.2: Irradiance spectrum of nightglow radiation [132].

The emitted radiance under 1.7 μm wavelength is found to be $L_{nightglow} = \sim 4.57\, nW/cm^2.sr$ using the **Figure 5.2**. The optical power that reaches to the detector is evaluated for f/1.4 aperture [133] considering the above radiance values. The calculations lead to $1.368\, nW/cm^2$ [131] and $1.828\, nW/cm^2$ [132] optical powers for the given measurements. In our simulations, $1.5\, nW/cm^2$ optical power is utilized in 1.5 μm wavelength for a reliable approximation of the nigthglow radiation.

5.2. InGaAs Detectors

SWIR photodetector technology is currently dominated by InGaAs material due its high performance at room temperature and low cost. As a III-V alloy, $In_{0.53}Ga_{0.47}As$ is a lattice matched material with InP substrate, where 4 inches epi-ready substrates are available for relatively low prices in the market. Furthermore, allowing fabrication of numerous detectors at the same time makes this semiconductor favorable choice for infrared detection industry. Apart from these, due to its optical properties, this alloy is perfectly suitable for the detection in SWIR window.

The cutoff wavelength of the lattice matched $In_{0.53}Ga_{0.47}As$ detector is 1.7 μm, which is sufficient for the significant number of SWIR applications. Moreover, it is possible to increase the cutoff wavelength to 2.5 μm by utilization of higher In compositions. However, in this case, the lattice mismatch may result in excessive number of defects and orders of magnitude increase in the dark current.

Even though InGaAs is one of the mature infrared detector material, the current limitation for this technology is surface leakage current. With the utilization of advanced passivation techniques and specialized layer structures, the dark current density has been reduced down to $0.19\,nA/cm^2$ at 273 K [133] ($J_{dark} = 0.26\,nA/\,cm^2$ at 273 K [134], $J_{dark} = 0.5\,nA/cm^2$ at 280 K [135], $J_{dark} = 2\,nA/cm^2$ at 285.3 K [136] & $J_{dark} = 0.64\,nA/cm^2$ at 283 K [137]). Note that the dark current density level is required as low as $1\,nA/cm^2$ in order to sense nightglow radiation [138].

5.3. SWIR HgCdTe Detectors

High quality ideal substrate HgCdTe detectors have diffusion-limited performance in SWIR band [117, 139, 140] for a wide range of temperatures. However, due to the price and availability issues of CdZnTe, HgCdTe is not a cost efficient material for the applications, where 1.7 μm cutoff wavelength is sufficient. Therefore, a large number of HgCdTe SWIR detectors are designed so that the cutoff wavelength is ~2.5 μm. At this wavelength, the lattice mismatched InGaAs detectors suffer from increased dark current values. Therefore, HgCdTe is the leading material for these cutoff wavelengths. Dark current of MCT SWIR detectors with cutoff wavelengths between 1.95-2.45 μm, which are fabricated by CEA and Sofradir [117], are reported to be limited by diffusion current above ~160 K temperature. It is also noted that surface passivation and the material quality is the limiting factors for the dark current performance at low temperatures, which may result in generation-recombination mechanism. In other studies [140, 141], SRH dark current is observed under ~ 140 K temperature for SWIR HgCdTe detector with 2.3 μm cutoff wavelength. However, the dark current density is measured higher than the Rule 07. Furthermore, Auger suppression can be utilized in order to decrease dark current of these detectors. With

this approach, very similar and even slightly lower dark current densities can be achieved than the ones for Rule 07 [139], which corresponds to diffusion-limited performance.

Although the ideal substrate HgCdTe detectors are successful to achieve diffusion-limited performance, low SRH carrier lifetimes significantly increase the dark current density [88, 142, 143]. For such condition, SRH recombination may dominate the detector dark current at elevated temperatures.

5.4. Alternative Substrate HgCdTe SWIR Design

Due to the availability and the cost of CZT substrates, InGaAs material is the leading choice for the state-of-art detection in SWIR window (for 1.7 cutoff wavelength). As previously mentioned, the alternative substrate technology has become a promising research area aiming to achieve similar performance with reduced cost of other semiconductor substrates. In this sense, the dark current suppression technique is utilized for alternative substrate HgCdTe SWIR detectors in order to improve detector performance.

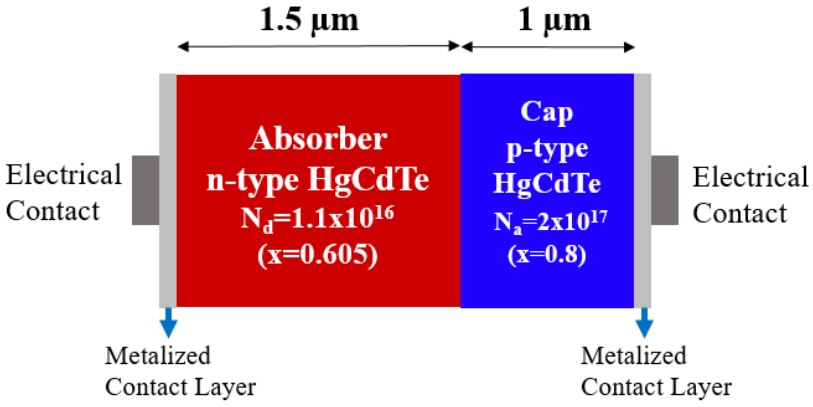

Figure 5.3: Double layer heterojunction (DLH) HgCdTe SWIR detector structure.

The Cd composition for the absorber layer is determined as $x = 0.605$ using the empirical formulation [104-106] given in Equation 3.76, which guarantees 1.7 µm cutoff wavelength at 300 K. The Cd composition for the cap layer is selected as $x = 0.8$ in order to minimize dark current contribution of this layer. The doping densities are utilized as $N_D = 1.1 \times 10^{16}\ cm^{-3}$ and $N_A = 2 \times 10^{17}\ cm^{-3}$ so that the

most of the depletion region is embedded in absorber layer (similar to DEH MWIR design). This situation allows us to implement the dark current suppression method by inserting an n-doped wide bandgap material. The layer structure for DL device is illustrated in the **Figure 5.3**.

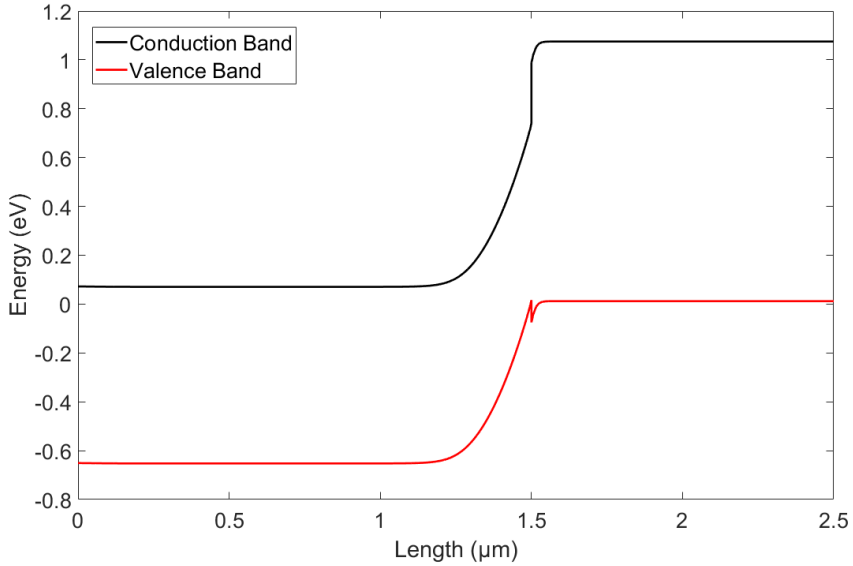

Figure 5.4: Band diagram for double layer heterojunction (DLH) HgCdTe SWIR detector structure obtained from Sentaurus Device.

As stated in the previous chapter, there is a trade of between suppression rate and the coverage of the depletion region. For a higher suppression rate, the length of depletion layer should be smaller in order to avoid valence band discontinuity. For the alternative substrate DEH detector structure, the SRH recombination rate can reach $\sim 10^{17}\ cm^{-3}/s$ inside the depletion region for a SRH lifetime as low as ~1 µm. For this reason, Cd composition of the depletion layer is selected to be $x = 0.8$, which maximizes the suppression rate. Even for this high Cd composition ($x = 0.8$), the detector current still contains a small portion of SRH dark current. However, for Cd compositions higher than 0.8, either the SRH dark current increases due to the partially coverage of depletion region or QE decreases significantly. Considering these constraints, the valence band discontinuity cancelation method is utilized to determine length of the suppressive layer for $x = 0.8$. The valence band offset introduced between absorber and depletion layers is evaluated as $70\ meV$ and the depletion layer length is determined to be $l = 0.21\ \mu m$. The DEH SWIR detector is illustrated in **Figure 5.5**.

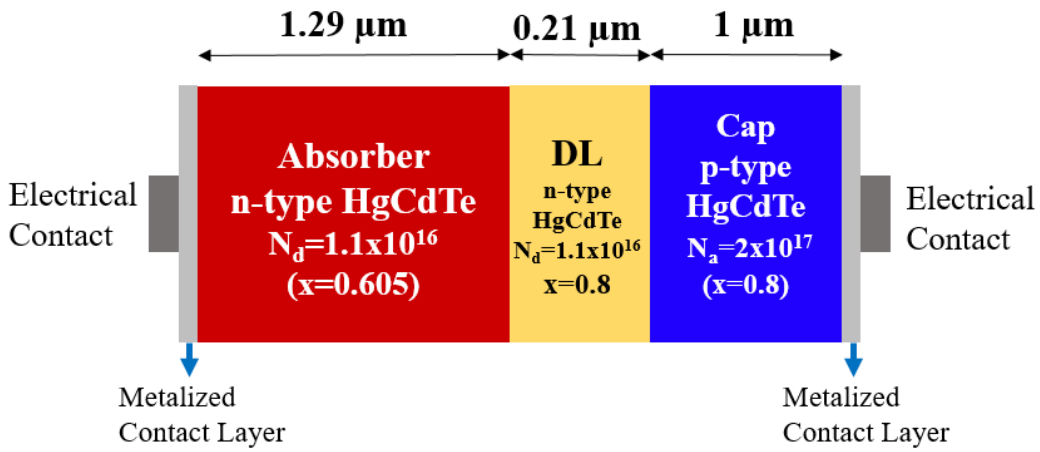

Figure 5.5: Layer structure for the DEL HgCdTe SWIR detector.

The designed SWIR detector consist of an n-type 1.29 µm long absorber layer which ensures significant absorption of incoming photons. The donor doping density is determined as $N_D = 1.1 \times 10^{16}\ cm^{-3}$ considering depletion region requirements and also the values in literature [88, 89]. The cutoff wavelength is selected to be 1.7 µm. Cd composition of the depletion layer is $x = 0.8$ and donor doping is the same with absorber layer. The length of this region is determined with the valence band reduction method and utilized as 0.21 µm. The layer structure for the DEH SWIR design is illustrated in **Figure 5.5**.

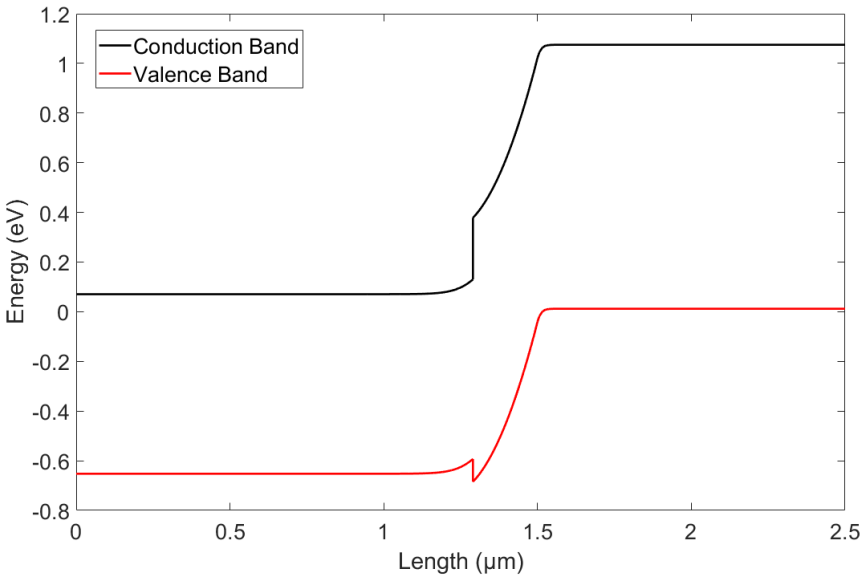

Figure 5.6: Band diagram for depletion engineered heterojunction (DEH) HgCdTe SWIR detector structure obtained from Sentaurus Device.

As shown in **Figure 5.6**, the valence band edge is nearly in the same level with the absorber and depletion layer interface. The performance analysis in the next section shows that there is no significant degradation in quantum efficiency due to the valence band discontinuity.

5.5. Performance Analysis for DEH SWIR Detector Design

The performance assessment has been made considering TAT, SRH, Auger and radiative recombinations. For $V_{bias} = -0.1\,V$, the operation temperature has been swept and dark current densities are compared together with QE values. During the simulations, flux rate corresponding to the nightglow radiance are utilized. Moreover, the system is assumed to have anti-reflection coating and f/1.4 aperture.

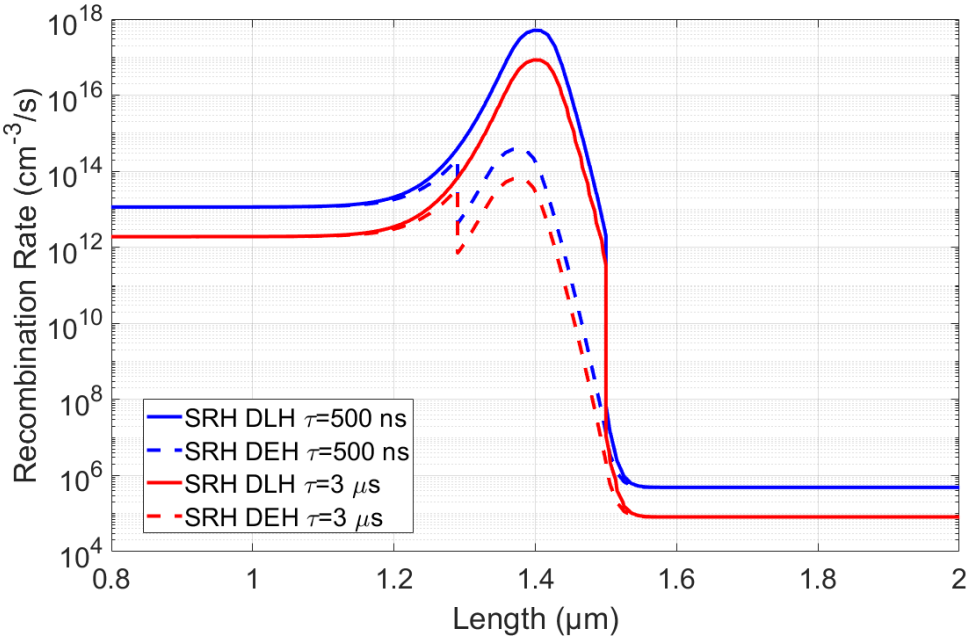

Figure 5.7: SRH recombination rate of SWIR DEH device for τ=500 ns and τ=3 μs carrier lifetimes obtained from Sentaurus Device software.

In order to represent low crystal quality of alternative substrate detectors, τ=500 ns and τ=3 μs carrier lifetimes are utilized in the simulations. As expected the SRH recombination rate is significantly lower for DEH SWIR device compared to DLH SWIR detector as shown in **Figure 5.7**. For both cases, the suppression rate yields ~13000 times decrease ($R_{SRH} = 5.0 \times 10^{17}\ cm^{-3}/s \rightarrow R_{SRH} = 3.91 \times 10^{14}\ cm^{-3}/s$) in the point where maximum recombination rate occurs.

The current densities evaluated under these conditions are represented in **Figure 5.8**. It is important to note that SWIR imaging is aimed to be done in room temperature. Alternatively, with a thermos electric cooler and vacuum package, sensors can operate just below the room temperature consuming very little energy. Therefore, the performance comparison is made for 273 K and 300 K.

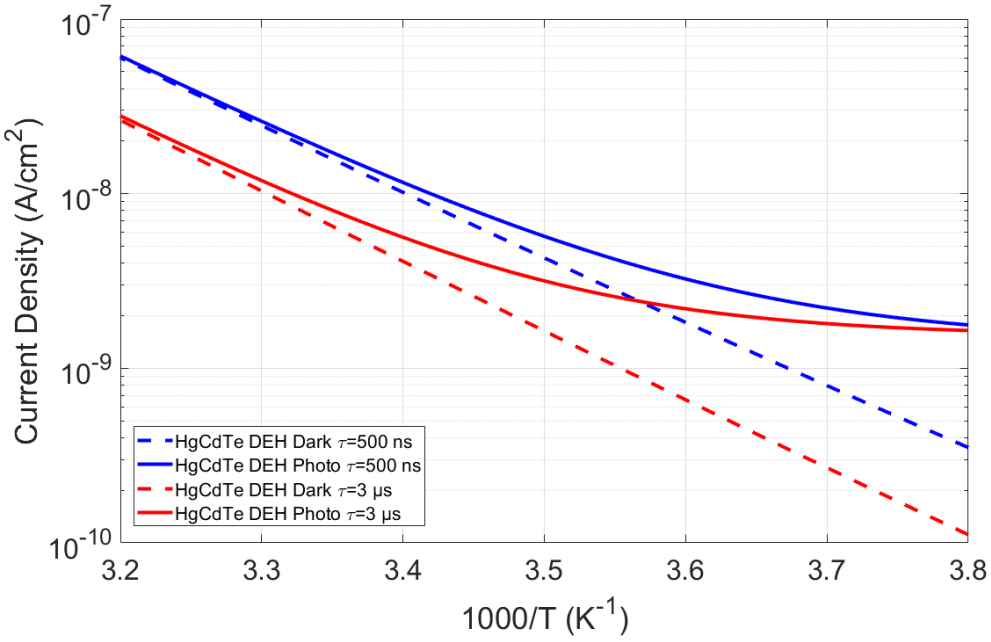

Figure 5.8: Dark and photo current densities of SWIR DEH device for τ=500 ns and τ=3 µs SRH lifetimes assuming that the shunt leakage is not present. The dark current values are obtained from Sentaurus Device.

The dark current value of the DEH SWIR design is decreased to $J_{dark} = 0.26\ nA/cm^2$ at 273 K and τ=3 µs, which is very similar to the state of art InGaAs detectors. This number is increased up to $J_{dark} = 0.76\ nA/cm^2$ for very short carrier lifetime (τ=500 ns). With this enhancement, the dark current densities of alternative substrate HgCdTe detectors reached to comparable values with the detectors sensing nightglow radiation. Note that the shunt leakage current generated by the dislocations may lead to an increase in the dark current, which may be the limiting factor for lattice-mismatched detectors.

For each simulation case, the photo current value is found as nearly $J_{photo} = 1.5\ nA/\ cm^2$. This means that the ratio of photo current to a dark current is more than one for the worst case scenario. For a more reasonable case, this ratio increases to ~4. Note that the current ultimate performance detectors provide the similar values without significantly decreasing the operation temperatures. In terms of quantum efficiency, HgCdTe detectors are able to reach ~78% and ~84% for τ=500 ns and τ=3 µs respectively, where the previous studies [132-134] state QE values between 80% and 85%.

CHAPTER 6

CONCLUSION AND FUTURE WORK

In this thesis work, numerical analysis has been made for high performance infrared detectors. An in-house numerical tool, which solves Poisson, current and continuity equations is utilized in order to contribute performance assessment of heterojunction infrared detectors at steady state. This tool is also capable of evaluating electrical properties of HgCdTe material for any Cd composition. Successive Over Relaxation and LU Decomposition numerical methods are implemented so that the aforementioned equations can be solved iteratively in one dimensional space. These methods are explained in detail and compared with each other in terms of convergence time and accuracy. During the analysis, a well-known commercial software Sentaurus Device and the in-house numerical tool have been utilized to design specialized detector structures, where the detectors are examined in various operation temperatures and carrier lifetimes.

Moreover, an alternative substrate MWIR HgCdTe detector is designed for the detection of near room temperature objects. It is fact that poor crystal quality originating from the defects and dislocations introduced by the alternative substrates trigger the recombination mechanisms and result in excessive dark current. The proposed layer structure is successfully eliminate this disadvantage by effective suppression of generation-recombination mechanisms in depletion region. A carefully designed wide bandgap layer is placed between p and n-type doped regions. With this technique, lowered intrinsic carrier density significantly reduced the recombination rates originating in depletion region.

Abrupt change in the composition between two consecutive layers introduces band discontinuities in both valence and conduction band. Even though they decreases the dark current density, the collection of photo-generated carriers are significantly disturbed by this process. Therefore, as an essential part of the dark current suppression, a method for valence band discontinuity reduction is proposed in order to find maximum utilizable length for the suppressive depletion layer without creating a hole blocking energy barrier. Considering the internal electrical potential inside the device and the band offset generation due to the change in the Cd mole fraction, maximum coverage of depletion region is achieved for the desired rate of suppression.

An optimized MWIR detector structure provides nearly ~40 K increase (from ~83.5 K to ~123.5 K) in the operation temperature at 99.9% BLIP operation. For the same operation temperature, the dark current density is decreased orders of magnitudes even for detectors with very low crystal quality. It is known that the shunt current generated by the dislocations may disturb the detector performance for lattice-mismatched semiconductors. However, currently, interaction between dislocations, density and the activation energy of dislocations cannot be analytically modelled. Hence, only SRH, TAT, Auger and radiative recombinations are included in the simulations. Considering these mechanisms, our results show that nearly diffusion limited dark current values can be achieved with the proposed sensor structure even for alternative substrates. Furthermore, the suppression rate is more significant for low quality substrates, which proves the reliability of the proposed design.

In order to model fabrication errors, sensitivity analysis has been made considering the fluctuations in doping density, depletion layer length and the composition. Except for the high doping case, QE is maintained high with only ~5% decrease. Even for the worst case, the sensor is still functional with ~20% decrease on QE.

SWIR imaging is another major research topic for research institutions. Currently, lattice matched InGaAs detectors dominated SWIR imaging industry with its low cost and high performance. In this thesis, a similar dark current suppression approach is utilized for the alternative substrate SWIR HgCdTe detectors in order to suppress SRH, radiative and TAT dark currents. The designed structure aimed to reach state of art detection capabilities of InGaAs detectors with reduced cost of alternative substrate HgCdTe material. For this purpose, the layer structure is designed with the valence

band reduction method and a significant amount of suppression of SRH recombination is achieved. The detector provide dark current density as low as $J_{dark} = 0.26\ nA/cm^2$ for recombination lifetime of 3 μs at 273 K.

The dark current performance is improved for the HgCdTe SWIR detector, which enables high performance detection with alternative substrate detectors. Furthermore, the detector is able to sense nightglow radiation considering the low dark current values ($< 1\ nA/cm^2$). This feature enhances the capabilities of SWIR imaging in a source free environment with volume and energy efficient camera system.

As a future work, the leakage currents and 1/f noise performance can be investigated for various fabricated detectors. The dominancy of the shunt current with respect to the bias voltage and noise coefficients of different noise mechanisms (GR & 1/f noise) might be investigated. Additionally, utilization of graded doping and Cd composition can be investigated in order to optimize layer transitions. This approach has a potential to reach 100% depletion coverage and complete suppression of corresponding recombination mechanisms.

REFERENCES

[1]A. Rogalski, "HgCdTe infrared detector material: history, status and outlook", 2018. .

[2]A. Rogalski, J. Antoszewski and L. Faraone, "Third-generation infrared photodetector arrays", Journal of Applied Physics, vol. 105, no. 9, p. 091101, 2009.

[3]W. Tennant, D. Lee, M. Zandian, E. Piquette and M. Carmody, "MBE HgCdTe Technology: A Very General Solution to IR Detection, Described by “Rule 07”, a Very Convenient Heuristic", Journal of Electronic Materials, vol. 37, no. 9, pp. 1406-1410, 2008.

[4]A. Rogalski, "Infrared detectors: an overview", Infrared Physics & Technology, vol. 43, no. 3-5, pp. 187-210, 2002.

[5]K. Tsai, K. Chang, C. Lee, K. Huang, J. Tsang and H. Chen, "Two-color infrared photodetector using GaAs/AlGaAs and strained InGaAs/AlGaAs multiquantum wells", Applied Physics Letters, vol. 62, no. 26, pp. 3504-3506, 1993.

[6]A. Perera, S. Matsik, H. Liu, M. Gao, M. Buchanan, W. Schaff and W. Yeo, "GaAs/InGaAs quantum well infrared photodetector with a cutoff wavelength at 35 μm", Applied Physics Letters, vol. 77, no. 5, pp. 741-743, 2000.

[7]S. Chakrabarti, X. Su, P. Bhattacharya, G. Ariyawansa and A. Perera, "Characteristics of a multicolor InGaAs-GaAs quantum-dot infrared photodetector", IEEE Photonics Technology Letters, vol. 17, no. 1, pp. 178-180, 2005.

[8]E. Lewis, P. Treado, R. Reeder, G. Story, A. Dowrey, C. Marcott and I. Levin, "Fourier Transform Spectroscopic Imaging Using an Infrared Focal-Plane Array Detector", Analytical Chemistry, vol. 67, no. 19, pp. 3377-3381, 1995.

[9]Ching-Yeu Wei, K. Wang, E. Taft, J. Swab, M. Gibbons, W. Davern and D. Brown, "Technology development for InSb infrared imagers", IEEE Transactions on Electron Devices, vol. 27, no. 1, pp. 170-175, 1980.

[10]E. Michel, J. Xu, J. Kim, I. Ferguson and M. Razeghi, "InSb infrared photodetectors on Si substrates grown by molecular beam epitaxy", IEEE Photonics Technology Letters, vol. 8, no. 5, pp. 673-675, 1996.

[11]S. Tong, J. Lee, H. Kim, F. Liu and K. Wang, "Ge dot mid-infrared photodetectors", Optical Materials, vol. 27, no. 5, pp. 1097-1100, 2005.

[12]L. Colace, G. Masini, G. Assanto, H. Luan, K. Wada and L. Kimerling, "Efficient high-speed near-infrared Ge photodetectors integrated on Si substrates", Applied Physics Letters, vol. 76, no. 10, pp. 1231-1233, 2000.

[13]S. Eker, Y. Arslan, M. Kaldirim and C. Besikci, "QWIP focal plane arrays on InP substrates for single and dual band thermal imagers", Infrared Physics & Technology, vol. 52, no. 6, pp. 385-390, 2009.

[14]S. Eker, Y. Arslan and C. Besikci, "High speed QWIP FPAs on InP substrates", Infrared Physics & Technology, vol. 54, no. 3, pp. 209-214, 2011.

[15]M. Tidrow, "Device physics and state-of-the-art of quantum well infrared photodetectors and arrays", Materials Science and Engineering: B, vol. 74, no. 1-3, pp. 45-51, 2000.

[16]A. Rogalski, P. Martyniuk and M. Kopytko, "InAs/GaSb type-II superlattice infrared detectors: Future prospect", Applied Physics Reviews, vol. 4, no. 3, p. 031304, 2017.

[17]Z. Xu, J. Chen, F. Wang, Y. Zhou and L. He, "High performance InAs/GaAsSb superlattice long wavelength infrared photo-detectors grown on InAs substrates", Semiconductor Science and Technology, vol. 32, no. 5, p. 055011, 2017.

[18]A. Daniels, “Field Guide to Infrared Systems, Detectors, and FPAs,” Second ed. Bellingham, Wash: SPIE Press, 2010.

[19]A. Joseph, "The Kirchhoff-Planck Radiation Law." Science 156, no. 3771 (1967): 30-37. http://www.jstor.org/stable/1720913.

[20] M. Planck, “On the law of distribution of energy in the normal spectrum”. Annalen der physik, 1901, 4.553: 1.

[21]G. Tattersall, "Infrared thermography: A non-invasive window into thermal physiology", 2018. .

[22]W. Blevin and W. Brown, "A Precise Measurement of the Stefan-Boltzmann Constant", Metrologia, vol. 7, no. 1, pp. 15-29, 1971.

[23]W. Wien, Proceedings of the Imperial Academy of Science, Berlin, February 9, 1893, p. 55.

[24]A. Rogalski and K. Chrzanowski, Infrared Devices and Techniques, vol. 10. Opto-electronics Review, 2002.

[25] H. M. Nussenzveig, W. J. Wiscombe, “Efficiency factors in Mie scattering”. Physical Review Letters, 45(18), 1490, 1980.

[26] R. J. Strutt, "The Light Scattered by Gases: Its Polarisation and Intensity." Proceedings of the Royal Society of London. Series A, Containing Papers of a Mathematical and Physical Character 95, no. 667: 155-76, 1918. http://www.jstor.org/stable/93666.

[27] G. Gaussorgues, Infared Thermography, Chapman and Hall, p91, 1994.

[28] B. G. Streetman and S. K. Banerjee, Solid State Electronic Devices, 6th Edition, Prentice Hall, 2006.

[29]C. Sah, R. Noyce and W. Shockley, "Carrier Generation and Recombination in P-N Junctions and P-N Junction Characteristics", Proceedings of the IRE, vol. 45, no. 9, pp. 1228-1243, 1957.

[30]Y. Nemirovsky, D. Rosenfeld, R. Adar and A. Kornfeld, "Tunneling and dark currents in HgCdTe photodiodes", Journal of Vacuum Science & Technology A: Vacuum, Surfaces, and Films, vol. 7, no. 2, pp. 528-535, 1989.

[31]P. Petersen, "Auger Recombination in Hg1−xCdxTe", Journal of Applied Physics, vol. 41, no. 8, pp. 3465-3467, 1970.

[32]W. van Roosbroeck and W. Shockley, "Photon-Radiative Recombination of Electrons and Holes in Germanium", Physical Review, vol. 94, no. 6, pp. 1558-1560, 1954.

[33]K. Van Vliet, "Noise in Semiconductors and Photoconductors", Proceedings of the IRE, vol. 46, no. 6, pp. 1004-1018, 1958.

[34]W. Guggenbuehl and M. O. Strutt, "Theory and Experiments on Shot Noise in Semiconductor Junction Diodes and Transistors", Proceedings of the IRE, vol. 45, no. 6, pp. 839-854, 1957.

[35]V. Radeka, "1/|f| Noise in Physical Measurements", IEEE Transactions on Nuclear Science, vol. 16, no. 5, pp. 17-35, 1969.

[36]"Understanding and Eliminating 1/f Noise | Analog Devices", Analog.com, 2018. [Online]. Available: http://www.analog.com/en/analog-dialogue/articles/understanding-and-eliminating-1-f-noise.html. [Accessed: 12- May- 2018].

[37]A. Rogalski, Infrared detectors. Amsterdam: Gordon & Breach, 2000.

[38]D. Lee, M. Carmody, E. Piquette, P. Dreiske, A. Chen, A. Yulius, D. Edwall, S. Bhargava, M. Zandian and W. Tennant, "High-Operating Temperature HgCdTe: A Vision for the Near Future", Journal of Electronic Materials, vol. 45, no. 9, pp. 4587-4595, 2016.

[39]J. Arias, M. Zandian, J. Pasko, S. Shin, L. Bubulac, R. DeWames and W. Tennant, "Molecular-beam epitaxy growth and in situ arsenic doping of p-on-n HgCdTe heterojunctions", Journal of Applied Physics, vol. 69, no. 4, pp. 2143-2148, 1991.

[40]L. He, J. Yang, S. Wang, S. Guo, M. Yu, X. Chen, W. Fang, Y. Qiao, Q. Zhang, R. Ding and T. Xin, "A study of MBE growth and thermal annealing of p-type long wavelength HgCdTe", Journal of Crystal Growth, vol. 175-176, pp. 677-681, 1997.

[41]J. Benson, L. Bubulac, M. Jaime-Vasquez, J. Arias, P. Smith, R. Jacobs, J. Markunas, L. Almeida, A. Stoltz, P. Wijewarnasuriya, J. Peterson, M. Reddy, K. Jones, S. Johnson and D. Lofgreen, "Impact of CdZnTe Substrates on MBE HgCdTe Deposition", Journal of Electronic Materials, vol. 46, no. 9, pp. 5418-5423, 2017.

[42]M. Reddy, J. Peterson, D. Lofgreen, J. Franklin, T. Vang, E. Smith, J. Wehner, I. Kasai, J. Bangs and S. Johnson, "MBE Growth of HgCdTe on Large-Area Si and CdZnTe Wafers for SWIR, MWIR and LWIR Detection", Journal of Electronic Materials, vol. 37, no. 9, pp. 1274-1282, 2008.

[43]W. Lei, J. Antoszewski and L. Faraone, "Progress, challenges, and opportunities for HgCdTe infrared materials and detectors", Applied Physics Reviews, vol. 2, no. 4, p. 041303, 2015.

[44]X. Hu, A. Huang, Q. Liao, L. Chen, X. Chen, H. Fan, H. Chen, R. Ding, L. He, D. Sun and Y. Liu, "Large format high SNR SWIR HgCdTe/Si FPA with multiple-choice gain for hyperspectral detection", Hyperspectral Imaging Sensors: Innovative Applications and Sensor Standards 2017, 2017.

[45]V. Bazovkin, S. Dvoretsky, A. Guzev, A. Kovchavtsev, D. Marin, V. Polovinkin, I. Sabinina, G. Sidorov, A. Tsarenko, V. Vasil'ev, V. Varavin and M. Yakushev, "High operating temperature SWIR p + –n FPA based on MBE-grown HgCdTe/Si(0 1 3)", Infrared Physics & Technology, vol. 76, pp. 72-74, 2016.

[46]J. Wenisch, W. Schirmacher, R. Wollrab, D. Eich, S. Hanna, R. Breiter, H. Lutz and H. Figgemeier, "Evaluation of HgCdTe on GaAs Grown by Molecular Beam Epitaxy for High-Operating-Temperature Infrared Detector Applications", Journal of Electronic Materials, vol. 44, no. 9, pp. 3002-3006, 2015.

[47]R. Gu, J. Antoszewski, W. Lei, I. Madni, G. Umana-Membrenao and L. Faraone, "MBE growth of HgCdTe on GaSb substrates for application in next generation infrared detectors", Journal of Crystal Growth, vol. 468, pp. 216-219, 2017.

[48]J. Zanatta, G. Badano, P. Ballet, C. Largeron, J. Baylet, O. Gravrand, J. Rothman, P. Castelein, J. Chamonal, A. Million, G. Destefanis, S. Mibord, E. Brochier and P. Costa, "Molecular beam epitaxy growth of HgCdTe on Ge for third-

generation infrared detectors", Journal of Electronic Materials, vol. 35, no. 6, pp. 1231-1236, 2006.

[49]C. Downs and T. Vandervelde, "Progress in Infrared Photodetectors Since 2000", Sensors, vol. 13, no. 4, pp. 5054-5098, 2013.

[50]K. Jóźwikowski, M. Kopytko and A. Rogalski, "Numerical Estimations of Carrier Generation–Recombination Processes and the Photon Recycling Effect in HgCdTe Heterostructure Photodiodes", Journal of Electronic Materials, vol. 41, no. 10, pp. 2766-2774, 2012.

[51]J. Wenus, J. Rutkowski and A. Rogalski, "Two-dimensional analysis of double-layer heterojunction HgCdTe photodiodes", IEEE Transactions on Electron Devices, vol. 48, no. 7, pp. 1326-1332, 2001.

[52]J. Arias, J. Pasko, M. Zandian, S. Shin, G. Williams, L. Bubulac, R. DeWames and W. Tennant, "Planarp-on-nHgCdTe heterostructure photovoltaic detectors", 2018.

[53]J. Bajaj, "State-of-the-art HgCdTe infrared devices", Photodetectors: Materials and Devices V, 2000.

[54]P. Martyniuk, M. Kopytko, A. Keblowski, K. Grodecki, W. Gawron and E. Gomulka, "Interface Influence on the Long-Wave Auger Suppressed Multilayer N+πP+p+n+ HgCdTe HOT Detector Performance", IEEE Sensors Journal, vol. 17, no. 3, pp. 674-678, 2017.

[55]S. Velicu, C. Grein, P. Emelie, A. Itsuno, J. Philips and P. Wijewarnasuriya, "MWIR and LWIR HgCdTe Infrared Detectors Operated with Reduced Cooling Requirements", Journal of Electronic Materials, vol. 39, no. 7, pp. 873-881, 2010.

[56]A. Itsuno, J. Phillips and S. Velicu, "Predicted Performance Improvement of Auger-Suppressed HgCdTe Photodiodes and p-n Heterojunction Detectors", IEEE Transactions on Electron Devices, vol. 58, no. 2, pp. 501-507, 2011.

[57]P. Emelie, S. Velicu, C. Grein, J. Phillips, P. Wijewarnasuriya and N. Dhar, "Modeling of LWIR HgCdTe Auger-Suppressed Infrared Photodiodes under

Nonequilibrium Operation", Journal of Electronic Materials, vol. 37, no. 9, pp. 1362-1368, 2008.

[58]M. Kinch, F. Aqariden, D. Chandra, P. Liao, H. Schaake and H. Shih, "Minority carrier lifetime in p-HgCdTe", Journal of Electronic Materials, vol. 34, no. 6, pp. 880-884, 2005.

[59]A. Itsuno, J. Phillips and S. Velicu, "Predicted Performance Improvement of Auger-Suppressed HgCdTe Photodiodes and $p\hbox{-}n$ Heterojunction Detectors", IEEE Transactions on Electron Devices, vol. 58, no. 2, pp. 501-507, 2011.

[60]P. Emelie, S. Velicu, C. Grein, J. Phillips, P. Wijewarnasuriya and N. Dhar, "Modeling of LWIR HgCdTe Auger-Suppressed Infrared Photodiodes under Nonequilibrium Operation", Journal of Electronic Materials, vol. 37, no. 9, pp. 1362-1368, 2008.

[61]P. Madejczyk, W. Gawron, P. Martyniuk, A. Keblowski, W. Pusz, J. Pawluczyk, M. Kopytko, J. Rutkowski, A. Rogalski and J. Piotrowski, "Engineering steps for optimizing high temperature LWIR HgCdTe photodiodes", 2018.

[62]P. Martyniuk and A. Rogalski, "Modelling of MWIR HgCdTe complementary barrier HOT detector", Solid-State Electronics, vol. 80, pp. 96-104, 2013.

[63]J. Antoszewski, N. Akhavan, G. Umana-Membreno, R. Gu, W. Lei and L. Faraone, "Recent Developments in Mercury Cadmium Telluride IR Detector Technology", ECS Transactions, vol. 69, no. 14, pp. 61-75, 2015.

[64]A. Itsuno, J. Phillips and S. Velicu, "Design and Modeling of HgCdTe nBn Detectors", Journal of Electronic Materials, vol. 40, no. 8, pp. 1624-1629, 2011.

[65]W. Qiu, T. Jiang and X. Cheng, "A bandgap-engineered HgCdTe PBπn long-wavelength infrared detector", Journal of Applied Physics, vol. 118, no. 12, p. 124504, 2015.

[66]N. Akhavan, G. Jolley, G. Umana-Membreno, J. Antoszewski and L. Faraone, "Performance Modeling of Bandgap Engineered HgCdTe-Based nBn Infrared

Detectors", IEEE Transactions on Electron Devices, vol. 61, no. 11, pp. 3691-3698, 2014.

[67]Wei-Cheng Qiu, Wei-Da Hu, Lu Chen, Chun Lin, Xiang-Ai Cheng, Xiao-Shuang Chen and Wei Lu, "Dark Current Transport and Avalanche Mechanism in HgCdTe Electron-Avalanche Photodiodes", IEEE Transactions on Electron Devices, vol. 62, no. 6, pp. 1926-1931, 2015.

[68]V. Gopal and W. Hu, "Characterization of leakage current mechanisms in long wavelength infrared HgCdTe photodiodes from a study of current–voltage characteristics under low illumination", Journal of Applied Physics, vol. 118, no. 22, p. 224503, 2015.

[69]V. Gopal, Q. Li, J. He, K. He, C. Lin and W. Hu, "Current transport mechanisms in mercury cadmium telluride diode", Journal of Applied Physics, vol. 120, no. 8, p. 084508, 2016.

[70]A. Rogalski and P. Martyniuk, "Mid-Wavelength Infrared nBn for HOT Detectors", Journal of Electronic Materials, vol. 43, no. 8, pp. 2963-2969, 2014.

[71]G. Destefanis, J. Baylet, P. Ballet, P. Castelein, F. Rothan, O. Gravrand, J. Rothman, J. Chamonal and A. Million, "Status of HgCdTe Bicolor and Dual-Band Infrared Focal Arrays at LETI", Journal of Electronic Materials, vol. 36, no. 8, pp. 1031-1044, 2007.

[72]E. Bellotti and D. D'Orsogna, "Numerical Analysis of HgCdTe Simultaneous Two-Color Photovoltaic Infrared Detectors", IEEE Journal of Quantum Electronics, vol. 42, no. 4, pp. 418-426, 2006.

[73]E. Smith, L. Pham, G. Venzor, E. Norton, M. Newton, P. Goetz, V. Randall, A. Gallagher, G. Pierce, E. Patten, R. Coussa, K. Kosai, W. Radford, L. Giegerich, J. Edwards, S. Johnson, S. Baur, J. Roth, B. Nosho, T. De Lyon, J. Jensen and R. Longshore, "HgCdTe focal plane arrays for dual-color mid- and long-wavelength infrared detection", Journal of Electronic Materials, vol. 33, no. 6, pp. 509-516, 2004.

[74]W. Tennant, D. Lee, M. Zandian, E. Piquette and M. Carmody, "MBE HgCdTe Technology: A Very General Solution to IR Detection, Described by “Rule 07”, a

Very Convenient Heuristic", Journal of Electronic Materials, vol. 37, no. 9, pp. 1406-1410, 2008.

[75]W. Tennant, "“Rule 07” Revisited: Still a Good Heuristic Predictor of p/n HgCdTe Photodiode Performance?", Journal of Electronic Materials, vol. 39, no. 7, pp. 1030-1035, 2010.

[76]J. Varesi, R. Bornfreund, A. Childs, W. Radford, K. Maranowski, J. Peterson, S. Johnson, L. Giegerich, T. de Lyon and J. Jensen, "Fabrication of high-performance large-format MWIR focal plane arrays from MBE-grown HgCdTe on 4″ silicon substrates", Journal of Electronic Materials, vol. 30, no. 6, pp. 566-573, 2001.

[77]M. Zandian, J. Garnett, R. Dewames, M. Carmody, J. Pasko, M. Farris, C. Cabelli, D. Cooper, G. Hildebrandt, J. Chow, J. Arias, K. Vural and D. Hall, "Mid-wavelength infrared p-on-n Hg1−xCdxTe heterostructure detectors: 30–120 kelvin state-of-the-Art performance", Journal of Electronic Materials, vol. 32, no. 7, pp. 803-809, 2003.

[78]M. Kinch, F. Aqariden, D. Chandra, P. Liao, H. Schaake and H. Shih, "Minority carrier lifetime in p-HgCdTe", Journal of Electronic Materials, vol. 34, no. 6, pp. 880-884, 2005.

[79]C. Fulk, W. Radford, D. Buell, J. Bangs and K. Rybnicek, "State-of-the-Art HgCdTe at Raytheon Vision Systems", Journal of Electronic Materials, vol. 44, no. 9, pp. 2977-2980, 2015.

[80]A. Kerlain, A. Brunner, D. Sam-Giao, N. Pére-Laperne, L. Rubaldo, V. Destefanis, F. Rochette and C. Cervera, "Mid-Wave HgCdTe FPA Based on P on N Technology: HOT Recent Developments. NETD: Dark Current and 1/f Noise Considerations", Journal of Electronic Materials, vol. 45, no. 9, pp. 4557-4562, 2016.

[81]W. Hu, J. He, W. Qiu, Z. Ye, L. Chen, C. Lin, L. He, X. Chen and W. Lu, "Recent progress on dark current characterization of very long-wavelength HgCdTe infrared photodetectors and HgCdTe APDs in SITP", Infrared Technology and Applications XLII, 2016.

[82]Q. Li, J. He, W. Hu, L. Chen, X. Chen and W. Lu, "Influencing Sources for Dark Current Transport and Avalanche Mechanisms in Planar and Mesa HgCdTe p-i-n

Electron-Avalanche Photodiodes", IEEE Transactions on Electron Devices, vol. 65, no. 2, pp. 572-576, 2018.

[83]N. Akhavan, G. Jolley, G. Umana-Membreno, J. Antoszewski and L. Faraone, "Design of Band Engineered HgCdTe nBn Detectors for MWIR and LWIR Applications", IEEE Transactions on Electron Devices, vol. 62, no. 3, pp. 722-728, 2015.

[84]S. Bansal, K. Sharma, N. Gupta and A. Singh, "Simulation and optimization of Hg1-xCdxTe based mid-wavelength IR photodetector", 2016 IEEE Uttar Pradesh Section International Conference on Electrical, Computer and Electronics Engineering (UPCON), 2016.

[85]S. Bansal, K. Sharma, K. Soni, N. Gupta, K. Ghosh and A. Singh, "Hg1-xCdxTe based p-i-n IR photodetector for free space optical communication", 2017 Progress In Electromagnetics Research Symposium - Spring (PIERS), 2017.

[86]O. Gravrand, F. Boulard, A. Ferron, P. Ballet and W. Hassis, "A New nBn IR Detection Concept Using HgCdTe Material", Journal of Electronic Materials, vol. 44, no. 9, pp. 3069-3075, 2015.

[87]P. Saxena and P. Chakrabarti, "Computer modeling of MWIR single heterojunction photodetector based on mercury cadmium telluride", Infrared Physics & Technology, vol. 52, no. 5, pp. 196-203, 2009.

[88] J. Schuster, R. DeWames, E. DeCuir, E. Bellotti and P. Wijewarnasuriya, "Junction optimization in HgCdTe: Shockley-Read-Hall generation-recombination suppression", Applied Physics Letters, vol. 107, no. 2, p. 023502, 2015.

[89] J. Schuster, R. DeWames, E. DeCuir, E. Bellotti, N. Dhar and P. Wijewarnasuriya, "Heterojunction depth in P+-on-n eSWIR HgCdTe infrared detectors: generation-recombination suppression", Infrared Sensors, Devices, and Applications V, 2015.

[90]A. Rogalski, A. Jozwikowska, K. Jozwikowski, and J. Rutkowski, "Performance of p+-n HgCdTe photodiodes," Semiconductor Science and Technology, vol. 8, pp. 289-292, 1993.

[91]J. Wenus, J. Rutkowski, and A. Rogalski, "Two-dimensional analysis of double-layer heterojunction HgCdTe photodiodes," IEEE Transactions on Electron Devices, vol. 48, pp. 250-260, 2001.

[92]J. V. Gumenjuk-Sichevskaja, F. F. Sizov, V. N. Ovsyuk, V. V. Vasil'ev, and D. G. Esaev, "Charge transport in HgCdTe-based n+-p photodiodes," Semiconductors, vol. 35, pp. 800-806, 2001.

[93]K. Kosai, "Status and application of HgCdTe device modeling," Journal of Electronic Materials, vol. 24, pp. 635-640, 1995.

[94]W. D. Hu et al., "Numerical analysis of two-color HgCdTe infrared photovoltaic heterostructure detector," Optical and Quantum Electronics, vol. 41, pp. 699-704, 2010.

[95]C. A. Keasler, M. Moresco, D. D'orsogna, P. Lamarre, and E. Bellotti, "3D numerical analysis of As-diffused HgCdTe planar pixel arrays," Proceeding of SPIE, vol. 7780, pp. 77800J-1-77800J-6, 2010.

[96]A. Jozwikowska, K. Jozwikowski, J. Antonsewski, and Z. Orman, "Generation-recombination effects on the dark currents in CdTe-passivated midwave infrared HgCdTe photodiodes," Journal of Applied Physics, vol. 98, pp. 014504-1-014504-11, 2005.

[97]Sentaurus Device User Guide, Version K-2015.06, June 2015.

[98]M. Tanemura, T. Ogawa and N. Ogita, "A new algorithm for three-dimensional voronoi tessellation", Journal of Computational Physics, vol. 51, no. 2, pp. 191-207, 1983.

[99]P. Muralidharan, "One-Dimensional Modeling of Mercury Cadmium Telluride Photodetectors Operated at Low Temperatures", Master of Science, Arizona State University, 2018.

[100]D. Vasileska, S. Goodnick and G. Klimeck, Computational electronics. Boca Raton: CRC Press, 2010.

[101]M. Usui, H. Niki and T. Kohno, "Adaptive gauss-seidel method for linear systems", International Journal of Computer Mathematics, vol. 51, no. 1-2, pp. 119-125, 1994.

[102]N. Wiener, "The Dirichlet Problem", Journal of Mathematics and Physics, vol. 3, no. 3, pp. 127-146, 1924.

[103]D. Scharfetter and H. Gummel, "Large-signal analysis of a silicon Read diode oscillator", IEEE Transactions on Electron Devices, vol. 16, no. 1, pp. 64-77, 1969.

[104]J. Gumenjuk-Sichevskaja, F. Sizov, V. Ovsyuk, V. Vasil'ev and D. Esaev, "Charge transport in HgCdTe-based n +-p photodiodes", Semiconductors, vol. 35, no. 7, pp. 800-806, 2001.

[105]D. D'orsogna, Ph.D. thesis, Boston University, 2010.

[106]P. Y. Emelie, Ph.D. thesis, The University of Michigan, 2009.

[107] D. H. Mao, Ph.D. thesis, Stanford University, 1998.

[108]H. Kocer, Y. Arslan and C. Besikci, "Numerical analysis of long wavelength infrared HgCdTe photodiodes", Infrared Physics & Technology, vol. 55, no. 1, pp. 49-55, 2012.

[109]J. Rosbeck, R. Starr, S. Price and K. Riley, "Background and temperature dependent current-voltage characteristics of HgCdTe photodiodes", Journal of Applied Physics, vol. 53, no. 9, pp. 6430-6440, 1982.

[110]W. Van Roosbroeck, "Theory of the Flow of Electrons and Holes in Germanium and Other Semiconductors", Bell System Technical Journal, vol. 29, no. 4, pp. 560-607, 1950.

[111]Y. Ozer and S. Kocaman, "Generation recombination suppression via depletion engineered heterojunction for alternative substrate MWIR HgCdTe infrared photodetectors", Journal of Applied Physics, vol. 122, no. 14, p. 143103, 2017.

[112]Y. Ozer and S. Kocaman, "A comparative design study for MWIR HgCdTe detectors", Infrared Technology and Applications XLIII, 2017.

[113]J. Benson, L. Bubulac, P. Smith, R. Jacobs, J. Markunas, M. Jaime-Vasquez, L. Almeida, A. Stoltz, J. Arias, G. Brill, Y. Chen, P. Wijewarnasuriya, S. Farrell and U. Lee, "Growth and Analysis of HgCdTe on Alternate Substrates", Journal of Electronic Materials, vol. 41, no. 10, pp. 2971-2974, 2012.

[114]L. He, X. Fu, Q. Wei, W. Wang, L. Chen, Y. Wu, X. Hu, J. Yang, Q. Zhang, R. Ding, X. Chen and W. Lu, "MBE HgCdTe on Alternative Substrates for FPA Applications", Journal of Electronic Materials, vol. 37, no. 9, pp. 1189-1199, 2008.

[115]A. Stoltz, J. Benson, M. Carmody, S. Farrell, P. Wijewarnasuriya, G. Brill, R. Jacobs and Y. Chen, "Reduction of Dislocation Density in HgCdTe on Si by Producing Highly Reticulated Structures", Journal of Electronic Materials, vol. 40, no. 8, pp. 1785-1789, 2011.

[116]R. Bommena, S. Ketharanathan, P. Wijewarnasuriya, N. Dhar, R. Kodama, J. Zhao, C. Buurma, J. Bergeson, F. Aqariden and S. Velicu, "High-Performance MWIR HgCdTe on Si Substrate Focal Plane Array Development", Journal of Electronic Materials, vol. 44, no. 9, pp. 3151-3156, 2015.

[117]O. Gravrand, L. Mollard, O. Boulade, V. Moreau, E. Sanson and G. Destéfanis, "Ultra low dark current CdHgTe FPAs in the SWIR range at CEA and Sofradir", Sensors, Systems, and Next-Generation Satellites XV, 2011.

[118] H. Cui, N. Tang, and Z. Tang, NUSOD, 2012.

[119] A. A. Guzev, A. P. Kovchavtcev, A. V. Tsarenko, M. V. Yakushev, V. S. Varavin, V. V. Vasilyev, S. A. Dvoretsky, D. V. Marin, I. V. Sabinina, D. A. Shefer, G. Y. Sidorov, and Y. G. Sidorov, MoP-IPRM-036 Compound Semiconductor Week, 2016.

[120] J. Song, J. Kim, M. Park, J. Kimb, K. Jung, S. Suh, “Iodine And Arsenic Doping Of (100)HgCdTe/GaAs Grown by Metalorganic Vapor Phase Epitaxy Using Isopropyl Iodide And Tris-Dimethylaminoarsenic”, Journal of Crystal Growth 1841185 (1998) 1232-1236

[121] L. He, J. Yang, S. Wang, M. Yu, Y. Wu , Y. Qiao, X. Chen, W. Fang, Q. Zhang, Y. Gui, J. Chu, “MBE Growth of HgCdTe for Infrared Focal Plane Arrays”, SPIE Vol. 3553 • 0277-786X/98 (2017)

[122] M. Carmody, A. Yulius, D. Edwall, D. Lee, E. Piquette, R. Jacobs, D. Benson, A. Stoltz, J. Markunas, A. Almeida, J. Arias, “Recent Progress in MBE Growth of CdTe and HgCdTe on (211)B GaAs Substrates”, Journal Of Electronic Materials, Vol. 41, No. 10, (2012)

[123]C. Besikci, "Extended short wavelength infrared FPA technology: status and trends", Quantum Sensing and Nano Electronics and Photonics XV, 2018.

[124]Ozer S and Besikci C., “Assessment of InSb photodetectors on Si substrates,” J. Phys. D: Appl. Phys. 36, 1-5 (2003).

[125]Johnson S.M., Rhiger D. R., Rosbeck J. P., Peterson J. M., Taylor S. M., and Boyd M. E., “Effect of dislocations on the electrical and optical properties of long-wavelength infrared HgCdTe photovoltaic detectors,” J. Vac. Sci. Technol. B 10, 1499-1506 (1992).

[126]Gopal V. and Gupta S., “Contributions of dislocations to 1/f noise in mercury cadmium telluride infrared photovoltaic detectors,” Infrared Phys. Technol. 48,59-66 (2006).

[127]Radford W. A. and Jones C. E., “1/f noise in ion-implanted and double-layer epitaxial HgCdTe photodiodes,” J. Vac. Sci. Technol. A 3, 183-188 (1985).

[128] Nemirovsky A. and Unikovsky A., “Tunneling and 1/f noise currents in HgCdTe photodiodes,” J. Vac. Sc. Technol. B 10, 1602-1610 (1992).

[129]Ciura L., Kolek A., Jurenczyk J., Czuba K., Jasik A., Sankowska I., Papis-Polakowska E., and Kaniewski J., “Noise-Current Correlations in InAs/GaSb Type-II Superlattice Midwavelength Infrared Detectors,” IEEE Tran.Electron Devices 63, 4907-4912 (2016).

[130] Bae S. H., Lee S. J., Kim H. Y., Lee H. C., and Kim C. K, “Analysis of 1/f Noise in LWIR HgCdTe Photodiodes,” J. Electronic Materials 29, 877-882 (2000).

[131]M. L. Vatsia, U. K. Stich and D. Dunlap, “Night-Sky Radiant Sterance from 450 to 2000 Nanometers.” ARMY NIGHT VISION LAB FORT BELVOIR VA, 1972.

[132]D. Dayton, R. Nolasco, J. Allen, M. Myers, J. Gonglewski, G. Fertig, D. Burns, and I. Mons, “SWIR sky glow imaging for detection of turbulence in the upper atmosphere,” Advanced Wavefront Control: Methods, Devices, and Applications VIII, 2010.

[133]H. Yuan, M. Meixell, J. Zhang, P. Bey, J. Kimchi and L. Kilmer, "Low dark current small pixel large format InGaAs 2D photodetector array development at Teledyne Judson Technologies", Infrared Technology and Applications XXXVIII, 2012.

[134]Michael MacDougal, Jon Geske, Chad Wang, David Follman, "Low-LightLevel InGaAs focal plane arrays with and without illumination," Proc. SPIE 7660, Infrared Technology and Applications XXXVI, 76600K (4 May 2010); doi: 10.1117/12.852605

[135]Infrared Technology and Applications XL, edited by Bjørn F. Andresen, Gabor F. Fulop, Charles M. Hanson, Paul R. Norton, Proc. of SPIE Vol. 9070, 907007 · © 2014 SPIE CCC code: 0277-786X/14/$18 · doi: 10.1117/12.2053999

[136]B. Onat, W. Huang, N. Masaun, M. Lange, M. Ettenberg and C. Dries, "Ultra-low dark current InGaAs technology for focal plane arrays for low-light level visible-shortwave infrared imaging", Infrared Technology and Applications XXXIII, 2007.

[137]M. MacDougal, J. Geske, C. Wang, S. Liao, J. Getty and A. Holmes, "Low dark current InGaAs detector arrays for night vision and astronomy", Infrared Technology and Applications XXXV, 2009.

[138]H. Figgemeier, M. Benecke, K. Hofmann, R. Oelmaier, A. Sieck, J. Wendler and J. Ziegler, "SWIR detectors for night vision at AIM", Infrared Technology and Applications XL, 2014.

[139]A. Wichman, B. Pinkie and E. Bellotti, "Dense Array Effects in SWIR HgCdTe Photodetecting Arrays", Journal of Electronic Materials, vol. 44, no. 9, pp. 3134-3143, 2015.

[140]L. Mollard, G. Bourgeois, C. Lobre, S. Gout, S. Viollet-Bosson, N. Baier, G. Destefanis, O. Gravrand, J. Barnes, F. Milesi, A. Kerlain, L. Rubaldo and A. Manissadjian, "p-on-n HgCdTe Infrared Focal-Plane Arrays: From Short-Wave to Very-Long-Wave Infrared", Journal of Electronic Materials, vol. 43, no. 3, pp. 802-807, 2013.

[141]V. Bazovkin, S. Dvoretsky, A. Guzev, A. Kovchavtsev, D. Marin, V. Polovinkin, I. Sabinina, G. Sidorov, A. Tsarenko, V. Vasil'ev, V. Varavin and M. Yakushev, "High operating temperature SWIR p + –n FPA based on MBE-grown HgCdTe/Si(0 1 3)", Infrared Physics & Technology, vol. 76, pp. 72-74, 2016.

[142]S. Simingalam, B. VanMil, Y. Chen, E. DeCuir, G. Meissner, P. Wijewarnasuriya, N. Dhar and M. Rao, "Development and fabrication of extended short wavelength infrared HgCdTe sensors grown on CdTe/Si substrates by molecular beam epitaxy", Solid-State Electronics, vol. 101, pp. 90-94, 2014.

[143]J. Schuster, R. DeWames, E. DeCuir, E. Bellotti, N. Dhar and P. Wijewarnasuriya, "Numerical Device Modeling, Analysis, and Optimization of Extended-SWIR HgCdTe Infrared Detectors", Journal of Electronic Materials, vol. 45, no. 9, pp. 4654-4662, 2016.